

## Galactic Winds across the Gas-Rich Merger Sequence. I. Highly Ionized N V and O VI Outflows in the QUEST Quasars\*

SYLVAIN VEILLEUX,<sup>1,2</sup> DAVID S. N. RUPKE,<sup>3</sup> WEIZHE LIU,<sup>1</sup> ANTHONY TO,<sup>3,4</sup> MARGARET TRIPPE,<sup>1,5,6</sup>  
TODD M. TRIPP,<sup>7</sup> FRED HAMANN,<sup>8</sup> REINHARD GENZEL,<sup>9</sup> DIETER LUTZ,<sup>9</sup> ROBERTO MAIOLINO,<sup>10,11</sup> HAGAI NETZER,<sup>12</sup>  
KENNETH R. SEMBACH,<sup>13</sup> ECKHARD STURM,<sup>9</sup> LINDA TACCONI,<sup>9</sup> AND STACY H. TENG<sup>1,14</sup>

<sup>1</sup>Department of Astronomy, University of Maryland, College Park, MD 20742, USA

<sup>2</sup>Joint Space-Science Institute, University of Maryland, College Park, MD 20742, USA

<sup>3</sup>Department of Physics, Rhodes College, Memphis, TN 38112, USA

<sup>4</sup>Department of Physics, University of Hawaii, Honolulu, HI 96822, USA

<sup>5</sup>Johns Hopkins University Applied Physics Laboratory, Laurel, MD 20723 USA

<sup>6</sup>Lincoln Laboratory, Massachusetts Institute of Technology, Lexington, MA 02421-6426 USA

<sup>7</sup>Department of Astronomy, University of Massachusetts, Amherst, MA 01003, USA

<sup>8</sup>Department of Physics and Astronomy, University of California, Riverside, CA 92507, USA

<sup>9</sup>Max-Planck-Institut für Extraterrestrische Physik, Giessenbachstrasse 1, 85748 Garching, Germany

<sup>10</sup>Cavendish Laboratory, University of Cambridge, 19 J.J. Thomson Avenue, Cambridge CB3 0HE, United Kingdom

<sup>11</sup>Kavli Institute for Cosmology, University of Cambridge, Madingley Road, Cambridge CB3 0HA, United Kingdom

<sup>12</sup>School of Physics and Astronomy, Tel-Aviv University, Tel Aviv 69978, Israel

<sup>13</sup>Space Telescope Science Institute, Baltimore, MD 21218, USA

<sup>14</sup>Institute for Defense Analyses, Alexandria, MD 22311, USA

### ABSTRACT

This program is part of QUEST (Quasar/ULIRG Evolutionary Study) and seeks to examine the gaseous environments of  $z \lesssim 0.3$  quasars and ULIRGs as a function of host galaxy properties and age across the merger sequence from ULIRGs to quasars. This first paper in the series focuses on 33 quasars from the QUEST sample and on the kinematics of the highly ionized gas phase traced by the N V  $\lambda\lambda 1238, 1243$  and O VI  $\lambda\lambda 1032, 1038$  absorption lines in high-quality *Hubble Space Telescope* (HST) Cosmic Origins Spectrograph (COS) data. N V and O VI outflows are present in about 60% of the QUEST quasars and span a broad range of properties, both in terms of equivalent widths (from 20 mÅ to 25 Å) and kinematics (outflow velocities from a few  $\times 100$  km s<sup>-1</sup> up to  $\sim 10,000$  km s<sup>-1</sup>). The rate of incidence and equivalent widths of the highly ionized outflows are higher among X-ray weak or absorbed sources. The weighted outflow velocity dispersions are highest among the X-ray weakest sources. No significant trends are found between the weighted outflow velocities and the properties of the quasars and host galaxies although this may be due to the limited dynamic range of properties of the current sample. These results will be re-examined in an upcoming paper where the sample is expanded to include the QUEST ULIRGs. Finally, a lower limit of  $\sim 0.1\%$  on the ratio of time-averaged kinetic power to bolometric luminosity is estimated in the 2–4 objects with blueshifted P V  $\lambda\lambda 1117, 1128$  absorption features.

*Keywords:* galaxies: evolution – ISM: jets and outflows – quasars: absorption lines – quasars: general

Corresponding author: Sylvain Veilleux  
veilleux@astro.umd.edu

\* Based on observations made with the NASA/ESA *Hubble Space Telescope*, obtained from the data archive at the Space Telescope Science Institute. STScI is operated by the Association of Universities for Research in Astronomy, Inc. under NASA contract NAS 5-26555.

### 1. INTRODUCTION

Large multiwavelength surveys of the local and distant universe have shown that major mergers of gas-

rich galaxies<sup>1</sup> may trigger spectacular bursts of star formation, accompanied with quasar-like episodes of rapid growth of the supermassive black holes (SMBHs), and result in merger remnants that follow tight SMBH-host scaling relations and resemble today’s quiescent early-type galaxies (e.g. Sanders et al. 1988; Hickox & Alexander 2018). Modern simulations of galaxy formation and evolution (e.g. Nelson et al. 2019; Oppenheimer et al. 2020; Nelson et al. 2021) largely reproduce these observations. However, the root cause of the fast “quenching” of the star formation activity in the merger remnants depends on the detailed, sub-grid scale, implementation of how the mass, momentum, and energy from stellar winds, supernova explosions, and SMBH-related processes are injected into, and interact with, the interstellar medium (ISM) and circumgalactic medium (CGM) of the host galaxies. Over the past several years, nearby gas-rich galaxy mergers have emerged as excellent laboratories to study in detail these stellar and quasar feedback processes (see Veilleux et al. 2020, for a recent review). These objects are the focus of the present study.

Locally, major gas-rich galaxy mergers often coincide with obscured ultraluminous infrared galaxies (ULIRGs). As these systems evolve, the obscuring gas and dust, funneled to the center by the dissipative collapse and tidal forces during the merger, are either transformed into stars or expelled out of the nucleus by powerful winds driven by the central quasar and starburst, giving rise to dusty quasars and finally to completely exposed quasars. Galactic-scale winds are ubiquitous in local ULIRGs and dusty quasars (e.g. Sturm et al. 2011; Veilleux et al. 2013a; Cicone et al. 2014; Rupke et al. 2017; Veilleux et al. 2017; Fluetsch et al. 2019, 2020; Lutz et al. 2020; Veilleux et al. 2020, and references therein). The outflows detected in ULIRGs extend over a large range of distances from the central energy source, seamlessly blending with the circumgalactic medium at  $>10$  kpc (Veilleux et al. 2020, and references therein).

In these objects, the outflow masses and energetics are often dominated by the outer ( $\gtrsim$ kpc) cool dusty molecular or neutral atomic gas phase, but the driving mechanism is best probed by examining the inner ( $\lesssim$  sub-kpc) ionized phase. ULIRG F11119+3257 is the first and still the best case among local ULIRGs where a fast ( $>0.1$  c), highly ionized (Fe XXV/XXVI at  $\sim 7$  keV), accretion-disk scale ( $<1$  pc) quasar wind appears to be driving a massive ( $> 100 M_{\odot} \text{ yr}^{-1}$ ), large-scale (1–10+ kpc) molecular and neutral-gas outflow (Tombesi et al.

2015, 2017; Veilleux et al. 2017). Unfortunately, the search for hot winds in a statistically significant sample of ULIRGs is not feasible at present since most ULIRGs are too faint at  $\sim 7$  keV for current X-ray observatories.

This is where the excellent far-ultraviolet (FUV) spectroscopic sensitivity of the *Hubble Space Telescope* (*HST*) becomes handy. The FUV band is rich in spectroscopic diagnostics of the neutral, low-ionization, and high-ionization gas phases (Haislmaier et al. 2021); thus *HST* can probe all three phases at once. So far, only about a dozen ULIRGs and IR-bright quasars have been studied with *HST*, but the results have been promising. Prominent, blueshifted Ly $\alpha$  emission out to  $-1000$  km s $^{-1}$  has been detected in half of these ULIRGs. Blueshifted absorption features from high-ionization species like N V and O VI (77 and 114 eV are needed to produce N $^{4+}$  and O $^{5+}$  ions, respectively) and/or low-ionization species like Si II, Si III, Fe II, N II, and Ar I have provided additional unambiguous signatures of outflows in a few of these objects. Martin et al. (2015) have argued that the FUV-detected outflows represent clumps of gas condensing out of a fast, hot wind generated by the central starburst (Thompson et al. 2016). This picture is also consistent with the blast-wave model for quasar feedback. In this model, a fast, hot wind shocks the surrounding ISM, which then eventually cools to reform the molecular gas after having acquired a significant fraction of the initial kinetic energy of the hot wind (e.g. Weymann et al. 1985; Zubovas & King 2012, 2014; Faucher-Giguère & Quataert 2012; Nims et al. 2015; Richings & Faucher-Giguère 2018a,b; Richings et al. 2021; Girichidis et al. 2021). An alternative explanation is radiative acceleration (e.g. Ishibashi et al. 2018, 2021), which may dominate the dynamics of outflows on a wide variety of scales (e.g. Stern et al. 2016; Revalski et al. 2018; Somalwar et al. 2020).

So far, the published data set on ULIRGs and IR-bright quasars is too small to draw strong conclusions about the properties of the FUV-detected winds. There is tantalizing evidence that UV-detected AGN/starburst-driven winds are present in most ULIRGs, but the sample is very incomplete, particularly among ULIRGs with AGN and matched quasars. A more diverse sample of ULIRGs and quasars is needed to study the gaseous environments of nearby quasars and ULIRGs as a function of host properties and age across the merger sequence from ULIRGs to quasars. This issue is addressed in the present study.

In this first paper, we focus our efforts on studying the highly ionized gas, traced by N V  $\lambda\lambda 1238, 1243$  and O VI  $\lambda\lambda 1032, 1038$ , in a sample of 33 local quasars, while Paper II (Liu et al. 2021, in prep.) will present

<sup>1</sup> In this paper, we define major mergers as those involving galaxies with  $\lesssim 4:1$  stellar mass ratios.

the results on our sample of ULIRGs with AGN and compare them with those on the quasars. As stated in Hamann et al. (2019b), the quasars in the present sample are valuable for outflow studies in and of themselves because: 1) they fill a largely-unexplored niche between luminous quasars with strong broad absorption lines (BALs) with outflow velocities of up to  $0.1 - 0.2 c$  and low-luminosity Seyfert 1 galaxies with exclusively narrower outflow lines, 2) their low redshift minimizes contamination by the Ly $\alpha$  forest, and 3) the outflow lines are relatively narrow so blending is less severe. Indeed, as we discuss below, the detected outflows often are “mini-BALs” instead of BALs because their velocity widths lie below or near the threshold of  $2000 \text{ km s}^{-1}$  used for BALs (Weymann et al. 1981, 1991; Hamann & Sabra 2004; Gibson et al. 2009b).

Our quasar sample is discussed in Section 2. The extensive set of ancillary data on these quasars is summarized in Section 3. The *HST* spectra used for this study are described in Section 4 and the methods applied to analyze these data are detailed in Section 5. The results from this analysis are presented in Section 6, and discussed in more detail in Section 7. Section 8 provides a summary of the main results from this paper.

## 2. QUASAR SAMPLE

The quasars in our sample are selected using four criteria: (1) They must be part of the QUEST (Quasar/ULIRG Evolutionary Study) sample of local ( $z \lesssim 0.3$ ) ULIRGs and quasars. The QUEST sample has already been described in detail in Veilleux et al. (2009a,b) and references therein. All 33 objects in the present sample are Palomar-Green (PG) quasars from the Bright Quasar Sample (Schmidt & Green 1983), except Mrk 231, the nearest quasar known, whose UV spectrum has already been analyzed by Veilleux et al. (2013b, 2016) and will not be discussed here any further. As part of the QUEST sample, the quasars are carefully matched in terms of redshifts, bolometric luminosities, and host galaxy masses with the QUEST ULIRGs of Paper II. (2) Their bolometric luminosity must be quasar-like,  $\gtrsim 10^{45} \text{ ergs s}^{-1}$ , and dominated by the quasar rather than the starburst based on the *Spitzer* data (see criterion #3 below) or, equivalently, have 25-to-60  $\mu\text{m}$  flux ratios  $f_{25}/f_{60} \gtrsim 0.15$  (Veilleux et al. 2009a). This criterion also automatically selects UV-detected late-stage mergers or non-mergers (Veilleux et al. 2009b). (3) A strong preference is also given to the QUEST quasars with *Spitzer* mid-infrared spectra to provide valuable information on the AGN contribution to the bolometric luminosities of these objects. (4) High-quality COS spectra covering systemic N V and/or O VI must exist for

each object in the sample. Only COS data are considered to ease comparisons between spectra and avoid possible systematic errors associated with comparing data sets from different instruments. As described in Section 4, both our own and archival data are used for this study.

These criteria result in a sample of 33 objects. Table 1 lists the key properties of the quasars in our sample, many of which are derived from our extensive set of ancillary data on these objects, discussed in Section 3. As shown in Figure 1, these quasars cover the low-redshift and low bolometric luminosity ends of the PG quasar sample. They are well matched in redshift with the QUEST ULIRGs which will be studied in Paper II (Liu et al. 2021, in prep), and are representative of the entire PG quasars sample in terms of infrared excess (defined here as the infrared-to-bolometric luminosity ratio,  $L_{\text{IR}}/L_{\text{BOL}}$ ) and FIR brightness ( $L_{60 \mu\text{m}}/L_{15 \mu\text{m}}$  from Netzer et al. 2007).

## 3. ANCILLARY DATA

An extensive set of spectroscopic and photometric data exist on all of the objects in the sample. Sloan Digital Sky Survey (SDSS) optical spectra are available for all of them. High-quality optical spectra also exist in Boroson & Green (1992), and Krug (2013) presents spectra centered on Na I D  $\lambda\lambda 5890, 5896$ . As mentioned in Section 2, most of these quasars have also been studied spectroscopically in the mid-infrared with *Spitzer* (Schweitzer et al. 2006, 2008; Netzer et al. 2007; Veilleux et al. 2009a). In addition, nearly all of the quasars in this sample are part of X-QUEST, an archival *XMM-Newton* and *Chandra* X-ray spectroscopic survey of the QUEST sample (Teng & Veilleux 2010; Columns 13-17 in Table 1). VLT and Keck near-infrared spectroscopic data exist for a number of these objects (Dasyra et al. 2007).

Optical and near-infrared images of these objects have been obtained from the ground (Surace et al. 2001; Veilleux et al. 2002; Guyon et al. 2006) and with *HST* (Veilleux et al. 2006; Kim et al. 2008; Hamilton et al. 2008; Veilleux et al. 2009b), providing photometric and morphological measurements on both the quasars and host galaxies (e.g., morphological type, quasar-to-host luminosity ratio, strength of tidal features). Far-infrared photometry obtained with the *Herschel* PACS instrument exists for all of these objects (Lani et al. 2017; Shangguan et al. 2018), while far-infrared spectra centered on the OH 119  $\mu\text{m}$  feature exist for five of them (Veilleux et al. 2013a). Finally, Green Bank Telescope (GBT) H I 21-cm line emission and absorption spectra are available for 16 of these quasars (Teng et al. 2013).

The connection between UV and X-ray properties is critical, so we searched the literature for additional X-ray measurements (ignoring older ones from *ROSAT/ASCA*). These are listed and referenced in Table 1. For *Chandra* observations from [Teng & Veilleux](#)

(2010) where no absorbing column was detected, more recent constraints from [Ricci et al. \(2017\)](#) (based on *Swift/BAT* detections) are available in some cases. In these cases, we substitute the newer measurement of absorbing column.

Table 1. Properties of the QUEST Quasars in the Sample

Name	Other Name	$z$	$\log \nu L_\nu(\text{UV})$	$\log R$	Radio Class	$\alpha_{\text{OX}}$	$\log(\frac{L_{\text{bol}}}{L_\odot})$	$\alpha_{\text{AGN}}$	$\log(\frac{L_{\text{IR}}}{L_\odot})$	$\log(\frac{M_{\text{BH}}}{M_\odot})$	$\log \eta_{\text{Edd}}$	$\log(L_{\text{SX}})$	$\log(L_{\text{HX}})$	$\Gamma_X$	$N_{\text{H}}$	Ref.
(1)	(2)	(3)	(4)	(5)	(6)	(7)	(8)	(9)	(10)	(11)	(12)	(13)	(14)	(15)	(16)	(17)
PG 0007+106	III Zw 2	0.0893	44.55	+2.29	Flat	-1.43	12.24	1 <sup>a</sup>	11.63	8.07 <sup>+0.45</sup> <sub>-0.46</sub>	-0.34 <sup>+0.46</sup> <sub>-0.45</sub>	43.94	44.18	1.73 <sup>+0.04</sup> <sub>-0.04</sub>	0.11 <sup>+0.02</sup> <sub>-0.01</sub>	a, 4, 5
PG 0026+129	...	0.1454	45.32	+0.03	Quiet	-1.50	12.08	0.986 <sup>+0.014</sup> <sub>-0.027</sub>	11.71	8.49 <sup>+0.44</sup> <sub>-0.45</sub>	-0.93 <sup>+0.45</sup> <sub>-0.44</sub>	44.04 <sup>+0.05</sup> <sub>-0.05</sub>	44.40	2.00 <sup>+0.13</sup> <sub>-0.11</sub>	<0.01	g, 5
PG 0050+124	I Zw 1	0.0589	44.24	-0.48	Quiet	-1.56	12.08	0.925 <sup>+0.075</sup> <sub>-0.094</sub>	12.04	7.33 <sup>+0.62</sup> <sub>-0.62</sub>	0.20 <sup>+0.62</sup> <sub>-0.62</sub>	43.78 <sup>+0.02</sup> <sub>-0.12</sub>	43.88 <sup>+0.05</sup> <sub>-0.09</sub>	2.25 <sup>+0.05</sup> <sub>-0.03</sub>	0.09 <sup>+0.08</sup> <sub>-0.08</sub>	f, 6
PG 0157+001	Mrk 1014	0.1633	45.34	+0.33	Quiet	-1.60	12.70	0.727 <sup>+0.236</sup> <sub>-0.271</sub>	12.67	8.06 <sup>+0.61</sup> <sub>-0.62</sub>	-0.01 <sup>+0.63</sup> <sub>-0.65</sub>	43.92 <sup>+0.04</sup> <sub>-0.04</sub>	43.63 <sup>+0.11</sup> <sub>-0.25</sub>	2.09 <sup>+0.03</sup> <sub>-0.03</sub>	0.04 <sup>+0.03</sup> <sub>-0.02</sub>	6
PG 0804+761	...	0.100	45.54	-0.22	Quiet	-1.52	12.09	0.996 <sup>+0.004</sup> <sub>-0.004</sub>	11.98	8.73 <sup>+0.43</sup> <sub>-0.43</sub>	-1.16 <sup>+0.43</sup> <sub>-0.43</sub>	44.54	44.45	2.27 <sup>+0.09</sup> <sub>-0.20</sub>	0.044 <sup>+0.007</sup> <sub>-0.010</sub>	a
PG 0838+770	VII Zw 244	0.1324	44.83	-0.96	Quiet	-1.54	11.77	0.945 <sup>+0.027</sup> <sub>-0.018</sub>	11.66	8.05 <sup>+0.61</sup> <sub>-0.62</sub>	-0.82 <sup>+0.62</sup> <sub>-0.61</sub>	44.152 <sup>+0.009</sup> <sub>-0.014</sub>	43.54 <sup>+0.04</sup> <sub>-0.05</sub>	1.49 <sup>+0.08</sup> <sub>-0.08</sub>	<0.1 <sup>b</sup>	d, 4, 5
PG 0844+349	...	0.064	44.59	-1.52	Quiet	-1.54	11.45	0.971 <sup>+0.029</sup> <sub>-0.039</sub>	11.18	7.86 <sup>+0.46</sup> <sub>-0.46</sub>	-0.94 <sup>+0.49</sup> <sub>-0.46</sub>	44.152 <sup>+0.009</sup> <sub>-0.014</sub>	43.80 <sup>+0.03</sup> <sub>-0.03</sub>	2.66 <sup>+0.05</sup> <sub>-0.06</sub>	6.13 <sup>+3.03</sup> <sub>-1.39</sub>	a, 6
PG 0923+201	...	0.192	45.42	-0.85	Quiet	-1.57	12.46	0.990 <sup>+0.000</sup> <sub>-0.000</sub>	12.05	7.90 <sup>+0.62</sup> <sub>-0.62</sub>	0.04 <sup>+0.62</sup> <sub>-0.62</sub>	44.54	44.45	2.27 <sup>+0.09</sup> <sub>-0.20</sub>	0.044 <sup>+0.007</sup> <sub>-0.010</sub>	a
PG 0953+414	...	0.2341	45.95	-0.36	Quiet	-1.50	12.53	0.982 <sup>+0.018</sup> <sub>-0.018</sub>	12.20	8.33 <sup>+0.44</sup> <sub>-0.44</sub>	-0.33 <sup>+0.44</sup> <sub>-0.44</sub>	45.037 <sup>+0.006</sup> <sub>-0.009</sub>	44.81 <sup>+0.02</sup> <sub>-0.03</sub>	2.44 <sup>+0.03</sup> <sub>-0.03</sub>	18.52 <sup>+9.84</sup> <sub>-5.6</sub>	h, 6
PG 1001+054	...	0.1611	44.93	-0.30	Quiet	-2.13	11.87	0.836 <sup>+0.123</sup> <sub>-0.100</sub>	11.66	7.63 <sup>+0.61</sup> <sub>-0.62</sub>	-0.35 <sup>+0.62</sup> <sub>-0.62</sub>	43.00 <sup>+0.18</sup> <sub>-0.30</sub>	43.08 <sup>+0.15</sup> <sub>-0.60</sub>	2.01 <sup>+0.67</sup> <sub>-0.48</sub>	8.09 <sup>+5.47</sup> <sub>-3.57</sub>	e, 6
PG 1004+130	4C +13.41	0.2406	45.30	+2.36	Steep	<-2.01	12.69	0.963 <sup>+0.037</sup> <sub>-0.036</sub>	12.22	9.16 <sup>+0.61</sup> <sub>-0.62</sub>	-1.01 <sup>+0.61</sup> <sub>-0.61</sub>	43.48 <sup>+0.05</sup> <sub>-0.05</sub>	43.70 <sup>+0.20</sup> <sub>-0.13</sub>	1.67 <sup>+0.11</sup> <sub>-0.11</sub>	2.99 <sup>+2.67</sup> <sub>-1.37</sub>	e, 6
PG 1116+215	...	0.1765	45.79	-0.14	Quiet	-1.57	12.55	0.991 <sup>+0.009</sup> <sub>-0.008</sub>	12.28	8.42 <sup>+0.61</sup> <sub>-0.62</sub>	-0.39 <sup>+0.62</sup> <sub>-0.61</sub>	44.927 <sup>+0.021</sup> <sub>-0.006</sub>	44.63 <sup>+0.03</sup> <sub>-0.04</sub>	2.53 <sup>+0.04</sup> <sub>-0.03</sub>	27.21 <sup>+16.01</sup> <sub>-11.26</sub>	h, 6
PG 1126-041	Mrk 1298	0.060	44.29	-0.77	Quiet	-2.13	11.53	0.962 <sup>+0.038</sup> <sub>-0.075</sub>	11.52	7.64 <sup>+0.61</sup> <sub>-0.62</sub>	-0.65 <sup>+0.62</sup> <sub>-0.61</sub>	43.04 <sup>+0.05</sup> <sub>-0.05</sub>	43.11 <sup>+0.05</sup> <sub>-0.12</sub>	1.95 <sup>+0.10</sup> <sub>-0.10</sub>	4.66 <sup>+0.42</sup> <sub>-0.39</sub>	a, 6
PG 1211+143	...	0.0809	44.96	+1.39	Steep	-1.57	11.97	1.000 <sup>+0.000</sup> <sub>-0.000</sub>	11.74	7.85 <sup>+0.61</sup> <sub>-0.62</sub>	-0.40 <sup>+0.62</sup> <sub>-0.61</sub>	44.328 <sup>+0.005</sup> <sub>-0.007</sub>	43.94 <sup>+0.01</sup> <sub>-0.01</sub>	2.83 <sup>+0.02</sup> <sub>-0.02</sub>	12.98 <sup>+0.94</sup> <sub>-0.90</sub>	h, 6
PG 1226+023	3C 273	0.158	46.50	+3.06	Flat	-1.47	13.03	0.949 <sup>+0.051</sup> <sub>-0.128</sub>	12.80	8.41 <sup>+0.15</sup> <sub>-0.24</sub>	0.08 <sup>+0.24</sup> <sub>-0.16</sub>	45.491 <sup>+0.002</sup> <sub>-0.002</sub>	45.742 <sup>+0.008</sup> <sub>-0.008</sub>	2.07 <sup>+0.01</sup> <sub>-0.01</sub>	<0.01	a, 5, 6
PG 1229+204	Mrk 771	0.064	44.42	-0.96	Quiet	-1.49	11.57	0.985 <sup>+0.015</sup> <sub>-0.030</sub>	11.27	7.76 <sup>+0.46</sup> <sub>-0.48</sub>	-0.71 <sup>+0.48</sup> <sub>-0.46</sub>	43.785 <sup>+0.007</sup> <sub>-0.008</sub>	43.61 <sup>+0.02</sup> <sub>-0.02</sub>	2.38 <sup>+0.03</sup> <sub>-0.03</sub>	13.52 <sup>+5.77</sup> <sub>-3.36</sub>	g, 6
Mrk 231	...	0.04217	42.70	-1.92	Quiet	-1.92	12.61	0.709 <sup>+0.066</sup> <sub>-0.067</sub>	12.54	8.58 <sup>+0.50</sup> <sub>-0.50</sub>	-0.63 <sup>+0.50</sup> <sub>-0.50</sub>	42.13 <sup>+0.01</sup> <sub>-0.04</sub>	42.58 <sup>+0.01</sup> <sub>-0.11</sub>	1.40 <sup>+0.03</sup> <sub>-0.01</sub>	9.5 <sup>+2.3</sup> <sub>-1.9</sub>	b, 7, 8
PG 1302-102	PKS 1302-102	0.2784	45.83	+2.27	Flat	-1.58	12.75	0.982 <sup>+0.015</sup> <sub>-0.034</sub>	12.49	8.77 <sup>+0.61</sup> <sub>-0.62</sub>	-0.55 <sup>+0.62</sup> <sub>-0.61</sub>	44.81	44.81	1.66 <sup>+0.10</sup> <sub>-0.11</sub>	<0.06	h, 1
PG 1307+085	...	0.155	45.35	-1.00	Quiet	-1.52	12.35	0.952 <sup>+0.066</sup> <sub>-0.066</sub>	11.76	8.54 <sup>+0.46</sup> <sub>-0.46</sub>	-0.72 <sup>+0.46</sup> <sub>-0.44</sub>	44.16 <sup>+0.05</sup> <sub>-0.09</sub>	44.16 <sup>+0.05</sup> <sub>-0.09</sub>	1.89 <sup>+0.10</sup> <sub>-0.10</sub>	5.64 <sup>+2.62</sup> <sub>-1.48</sub>	a, 6
PG 1309+355	...	0.1829	45.05	+1.26	Flat	-1.71	12.32	0.870 <sup>+0.130</sup> <sub>-0.127</sub>	12.05	8.24 <sup>+0.61</sup> <sub>-0.62</sub>	-0.49 <sup>+0.62</sup> <sub>-0.62</sub>	43.87 <sup>+0.02</sup> <sub>-0.05</sub>	43.88 <sup>+0.04</sup> <sub>-0.05</sub>	2.19 <sup>+0.06</sup> <sub>-0.06</sub>	6.02 <sup>+1.84</sup> <sub>-1.84</sub>	i, 6
PG 1351+640	...	0.0882	45.22	+0.64	Quiet	-1.78	12.05	0.779 <sup>+0.143</sup> <sub>-0.221</sub>	11.87	8.72 <sup>+0.61</sup> <sub>-0.62</sub>	-1.30 <sup>+0.62</sup> <sub>-0.63</sub>	43.398 <sup>+0.007</sup> <sub>-0.023</sub>	43.23 <sup>+0.03</sup> <sub>-0.04</sub>	2.42 <sup>+0.04</sup> <sub>-0.04</sub>	14.61 <sup>+5.72</sup> <sub>-3.81</sub>	h, 6

Table 1 continued

Table 1 (continued)

Name	Other Name	$z$	$\log \nu L_\nu(\text{UV})$	$\log R$	Radio Class	$\alpha_{\text{OX}}$	$\log(L_{\text{bol}}/L_\odot)$	$\alpha_{\text{AGN}}$	$\log(L_{\text{IR}}/L_\odot)$	$\log(M_{\text{BH}}^{\text{IR}}/M_\odot)$	$\log \eta_{\text{Edd}}$	$\log(L_{\text{SX}})$	$\log(L_{\text{HX}})$	$\Gamma_X$	$N_{\text{H}}$	Ref.
(1)	(2)	(3)	(4)	(5)	(6)	(7)	(8)	(9)	(10)	(11)	(12)	(13)	(14)	(15)	(16)	(17)
PG 1411+442	...	0.0896	44.34	-0.89	Quiet	-2.03	11.79	$1.000^{+0.000}_{-0.000}$	11.66	$8.54^{+0.45}_{-0.46}$	-1.27 <sup>+0.46</sup>	$43.60^{+0.05}_{-0.06}$	$43.41^{+0.06}_{-0.18}$	$2.41^{+0.18}_{-0.15}$	$26.29^{+3.76}_{-4.08}$	h, 6
PG 1435-067	...	0.129	45.12	-1.15	Quiet	-1.63	11.92	$0.976^{+0.024}_{-0.040}$	11.47	$8.26^{+0.61}_{-0.62}$	-0.86 <sup>+0.62</sup>	$44.11^{+0.04}_{-0.04}$	$43.94^{+0.07}_{-0.08}$	$2.36^{+0.11}_{-0.10}$	<0.1 <sup>b</sup>	a, 6
PG 1440+356	Mrk 478	0.077	45.18	-0.43	Quiet	-1.38	11.81	$0.836^{+0.071}_{-0.081}$	11.76	$7.36^{+0.61}_{-0.62}$	-0.15 <sup>+0.62</sup>	$44.33^{+0.01}_{-0.01}$	$43.74^{+0.05}_{-0.06}$	$3.02^{+0.04}_{-0.04}$	$8.92^{+8.66}_{-3.51}$	a, 6
PG 1448+273	...	0.065	43.78	-0.60	Quiet	-1.59	11.44	$0.997^{+0.003}_{-0.007}$	11.19	$6.86^{+0.61}_{-0.62}$	0.06 <sup>+0.62</sup>	$44.375^{+0.005}_{-0.004}$	$43.90^{+0.01}_{-0.01}$	$2.86^{+0.01}_{-0.01}$	$14.24^{+2.88}_{-2.34}$	6
PG 1501+106	Mrk 841	0.036	44.03	-0.44	Quiet	-1.64	11.34	$1.000^{+0.000}_{-0.000}$	11.13	$8.42^{+0.61}_{-0.62}$	-1.59 <sup>+0.62</sup>	$44.049^{+0.005}_{-0.002}$	$43.833^{+0.008}_{-0.008}$	$2.46^{+0.02}_{-0.02}$	$23.12^{+6.40}_{-4.56}$	a, 6
PG 1613+658	Mrk 876	0.129	45.43	+0.00	Quiet	-1.21	12.30	$0.820^{+0.106}_{-0.092}$	12.25	$8.34^{+0.46}_{-0.51}$	-0.64 <sup>+0.51</sup>	$44.090^{+0.002}_{-0.003}$	$43.845^{+0.008}_{-0.007}$	$2.50^{+0.02}_{-0.02}$	$18.66^{+3.60}_{-2.47}$	6
PG 1617+175	Mrk 877	0.114	44.93	-0.14	Quiet	-1.64	11.75	$0.903^{+0.097}_{-0.081}$	11.55	$8.67^{+0.44}_{-0.45}$	-1.48 <sup>+0.44</sup>	$44.068^{+0.004}_{-0.004}$	$43.851^{+0.006}_{-0.006}$	$2.45^{+0.02}_{-0.02}$	$15.88^{+2.47}_{-2.07}$	6
PG 1626+554	...	0.133	45.17	-0.96	Quiet	-1.37	11.84	$0.976^{+0.024}_{-0.019}$	10.90	$8.39^{+0.61}_{-0.62}$	-1.08 <sup>+0.62</sup>	$43.740^{+0.004}_{-0.004}$	$43.672^{+0.006}_{-0.006}$	$2.26^{+0.01}_{-0.01}$	$13.01^{+0.57}_{-0.50}$	6
PG 2130+099	II Zw 136	0.063	44.46	-0.49	Quiet	-1.47	11.78	$0.995^{+0.005}_{-0.010}$	11.63	$7.43^{+0.43}_{-0.43}$	-0.17 <sup>+0.43</sup>	$43.623^{+0.004}_{-0.006}$	$43.65^{+0.01}_{-0.01}$	$2.11^{+0.02}_{-0.02}$	$11.48^{+1.69}_{-1.56}$	6
PG 2214+139	Mrk 304	0.0658	44.45	-1.30	Quiet	-2.02	11.78	$0.998^{+0.002}_{-0.004}$	11.46	$8.44^{+0.62}_{-0.62}$	-1.18 <sup>+0.62</sup>	$44.28^{+0.06}_{-0.03}$	$44.38^{+0.07}_{-0.09}$	$1.95^{+0.10}_{-0.10}$	$28.24^{+107.78}_{-20.67}$	a, 6
PG 2233+134	...	0.3265	45.94	-0.55	Quiet	-1.66	12.56	$1^d$	12.33	$7.93^{+0.61}_{-0.60}$	0.12 <sup>+0.62</sup>	$44.44^{+0.03}_{-0.02}$	$44.43^{+0.05}_{-0.06}$	$2.12^{+0.08}_{-0.08}$	$10.45^{+10.78}_{-4.77}$	6
PG 2349-014	4C-01.61	0.1742	45.51				12.59	$0.904^{+0.045}_{-0.054}$	11.90	$9.14^{+0.50}_{-0.50}$	-1.11 <sup>+0.50</sup>	$44.57$	$44.57$	$1.78^{+0.20}_{-0.39}$	<0.01	e, 5

Table 1 continued

Table 1 (continued)

Name	Other	$z$	$\log \nu L_\nu$ (UV)	$\log R$	Radio	$\alpha_{\text{OX}}$	$\log(\frac{L_{\text{bol}}}{L_\odot})$	$\alpha_{\text{AGN}}$	$\log(\frac{L_{\text{IR}}}{L_\odot})$	$\log(\frac{M_{\text{BH}}}{M_\odot})$	$\log \eta_{\text{Edd}}$	$\log(L_{\text{SX}})$	$\log(L_{\text{HX}})$	$\Gamma_X$	$N_{\text{H}}$	Ref.
(1)	(2)	(3)	[erg s <sup>-1</sup> ]	(5)	Class	(7)	(8)	(9)	(10)	(11)	(12)	[erg s <sup>-1</sup> ]	[erg s <sup>-1</sup> ]	(15)	[10 <sup>22</sup> cm <sup>-2</sup> ]	(17)

NOTE—Column (1): Object name. Column (2): Other name. Column (3): Redshifts, with reference listed in Column (17). Where available, redshifts are based on the [O III] narrow line. For 3 quasars, we use H I (de Vaucouleurs et al. 1991; Carilli et al. 1998; Springob et al. 2005) instead; for two, full-spectrum fits to SDSS spectra (Schneider et al. 2010); and for a single case, CO data (Evans et al. 2006). Column (4): Logarithm of the monochromatic luminosity at rest-frame 1125 Å derived using the Galactic extinctions from Schlafly & Finkbeiner (2011) and the reddening curve with  $R_V = 3.1$  of Fitzpatrick (1999). Column (5): logarithm of  $R$ , the ratio of radio-to-optical luminosity from Boroson & Green (1992). Column (6): Radio class – Quiet, Steep, or Flat depending on  $\log R$  and radio spectral index from Boroson & Green (1992). Column (7): X-ray to optical spectral index  $\alpha_{\text{OX}} = 0.372 \log(f_{2 \text{ keV}}/f_{3000 \text{ Å}})$  from Brandt et al. (2000), where  $f_{2 \text{ keV}}$  and  $f_{3000 \text{ Å}}$  are the rest-frame flux densities at 2 keV and 3000 Å, respectively. (For Mrk 231, we report the value from Teng et al. (2014).) Column (8): Bolometric luminosity in solar units calculated from  $7 \times L(5100 \text{ Å}) + L_{\text{IR}}$  (Netzer et al. 2007), where  $L(5100 \text{ Å})$  is the continuum luminosity  $\lambda L_\lambda$  at 5100 Å rest wavelength and  $L_{\text{IR}}$  is the 1 – 1000  $\mu\text{m}$  infrared luminosity listed in column (10). We adopt a cosmology of  $H_0 = 69.3 \text{ km s}^{-1}$ ;  $\Omega_m = 0.287$ ;  $\Omega_\lambda = 0.713$  (WMAP9). Column (9): Fraction of the bolometric luminosity produced by the AGN, i.e.  $\alpha_{\text{AGN}} = L_{\text{AGN}}/L_{\text{BOL}}$ , based on the *Spitzer* results (Veilleux et al. 2009a). The error bars are computed from the lowest and highest values among the six methods from this paper. Column (10): Logarithm of the 1 – 1000  $\mu\text{m}$  infrared luminosity in solar units from Zhuang et al. (2018), except Mrk 231 (U et al. 2013), PG 1626+554 (Lyu et al. 2017), and PG 2349–014 (Veilleux et al. 2009b). Column (11): Logarithm of the black hole mass in solar units from reverberation mapping (RM) measurements from The AGN Black Hole Mass Database (Bentz & Katz 2015) or, if unavailable, single-epoch measurements from Vestergaard & Peterson (2006), normalized down from  $f = 5.5$  (Onken et al. 2004) to  $f = 4.3$  to match RM scaling. According to Vestergaard & Peterson (2006), single-epoch measurements should have an extra 0.43 error added in quadrature. For PG 2349–014, we used the more uncertain photometric measurement of Veilleux et al. (2009b). For 3C 273, we recorded the GRAVITY measurement (Gravity Collaboration et al. 2018). Column (12): Logarithm of the ratio of the bolometric luminosity to the Eddington luminosity. Column (13): Luminosity in the soft X-rays (0.5 – 2 keV). Column (14): Luminosity of the hard X-rays (2 – 10 keV). Column (15): Photon index of the best-fit absorbed power-law distribution to the X-ray emission ( $dN/dE \propto E^{-\Gamma_X}$  where  $E$  is the X-ray photon energy). Column (16): Column density in units of 10<sup>22</sup> cm<sup>-2</sup>. For most data from Teng & Veilleux (2010), this is from the best-fit absorbed power-law. Where this best fit is unabsorbed and *Swift*/*BAT* data are available, we substitute  $N_{\text{H}}$  from Ricci et al. (2017). For X-ray related quantities, different rows = different observations, dates. Column (17): References for the redshift and X-ray measurements.

**References**—Redshift: (a) Boroson & Green 1992; (b) Carilli et al. 1998; (c) de Vaucouleurs et al. 1991; (d) Evans et al. 2006; (e) Hewett & Wild 2010; (f) Ho & Kim 2009; (g) Hu et al. 2020; (h) Marziani et al. 1996; (i) Schneider et al. 2010; (j) Springob et al. 2005; X-ray: (1) Inoue et al. 2007; (2) Jin et al. 2012; (3) Laha et al. 2018; (4) Piconcelli et al. 2005; (5) Ricci et al. 2017; (6) Teng & Veilleux 2010; (7) Teng et al. 2014; (8) Veilleux et al. 2014; (9) Waddell & Gallo 2020

<sup>a</sup>No measurement; we assume a value of 1.

<sup>b</sup>Best-fit value is 0; we assume an upper limit of 10<sup>21</sup> cm<sup>-2</sup>.

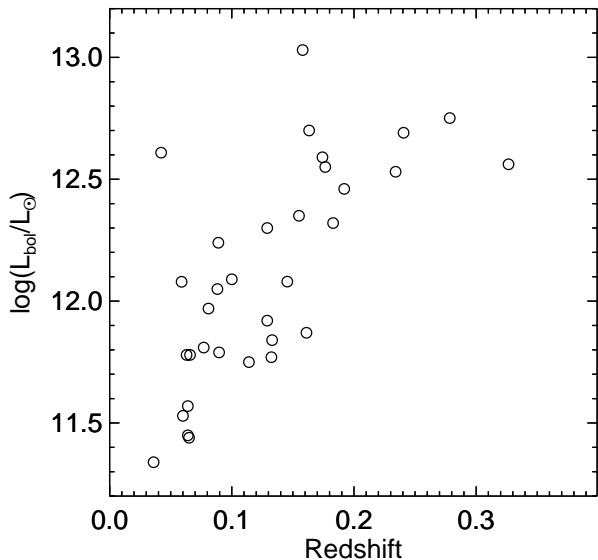


**Figure 1.** Bolometric (AGN + starburst) luminosities of the QUEST quasars in the sample as a function of their redshifts.

#### 4. HST DATA

We obtained high-quality spectra for 19 quasars using the Cosmic Origins Spectrograph (COS) with grating G130M under *HST* PID 12569 in Cycle 19 (PI Veilleux). We acquired multi-epoch COS/G130M data on PG 1411+442 under programs 13451, 14460, and 14885 (PI Hamann). We searched for archival COS/G130M spectra of other quasars in the QUEST sample, as well as for multi-epoch data on the subsample we observed. We found archival data on 14 additional QUEST quasars and recent multi-epoch exposures for three quasars in the subsample first observed in Cycle 19. We list the characteristics of these observations in Table 2.

Since most of the Cycle 19 COS data have not yet been the subject of a paper (the exceptions are Mrk 231 and PG 1411+442; Veilleux et al. 2013b, 2016; Hamann et al. 2019b), we briefly summarize here how they were obtained. A total of 24 orbits were allocated for these 19 targets with most targets requiring one orbit. The exceptions are PG 1004+130 (2 orbits) and Mrk 231 (5 orbits). All but Mrk 231 are point sources with accurate positions; they were acquired directly using ACQ/PEAKXD and ACQ/PEAKD. For Mrk 231, a NUV image was obtained with ACQ/IMAGE. All observations were observed in time-tag mode to allow us to exclude poor quality data and improve thermal correction and background removal. We split the exposures into four segments of similar durations at two FP\_POS settings (#2 and #4) and two wavelength settings (CEN-

WAVE) separated by  $\sim 20$  Å. This observing strategy reduces the fixed pattern noise and fills up the chip gap without excessive overheads.

The observations include at least 1150–1450 Å in the observer’s frame. This range includes redshifted O VI  $\lambda\lambda$  1032, 1038, N V  $\lambda\lambda$ 1238, 1243, Ly $\alpha$   $\lambda$ 1216 and/or Ly $\beta$   $\lambda$ 1025 in emission and/or absorption. In at least two cases (PG 1126–041, PG 1411+442, and perhaps also PG 1001+054 and PG 1004+130; see Sec. 7.4), the weaker P V  $\lambda\lambda$ 1117, 1128 absorption lines are also detected. The specific lines covered depend on the quasar redshift. The short-wavelength cutoff of the COS prevents us from searching for O VI systems in quasars with  $z \lesssim 0.11$ , while N V systems are redshifted out of the COS data in quasars with  $z \gtrsim 0.18$ . It is therefore possible to study both O VI and N V only over a limited range of quasar redshifts. Nevertheless, we achieve our science goals by covering at least one H I Lyman series line and one high-ionization doublet (O VI and/or N V). In at least two cases (PG 1411+442 and PG 1004+130), weaker and/or lower-ionization lines, such as C II  $\lambda$ 1335, C III  $\lambda$ 977, N III  $\lambda$ 990, O I  $\lambda$ 1304, Si II  $\lambda$ 1260, Si III  $\lambda$ 1206, and Si IV  $\lambda\lambda$ 1394, 1403, are also present in the spectra. These lines may be used to help constrain the location, ionization, total column densities ( $N_H$ ) and metal abundances in the absorbing gas (e.g. Hamann et al. 2019b). PG 1004+130, one of the highest-redshift sources in our sample, also shows S VI  $\lambda\lambda$ 933, 945.

All of our sample have data with CENWAVE of 1291, 1300, 1309, 1318, and/or 1327, and almost all of the data (with the exception of the final round of data on PG 1001+054) were obtained in COS lifetime positions (LP) 1–3. For these CENWAVE settings, the spectral resolution of COS increases with wavelength and has degraded somewhat with changes in LP, but is still  $>10^4$  at all wavelengths. This corresponds to resolution better than  $30 \text{ km s}^{-1}$  FWHM at all wavelengths, ranging up to a peak of  $\sim 15 \text{ km s}^{-1}$  at LP1 and 1450 Å. Three quasars have additional data from CENWAVE 1055, 1096, or 1222 observations. For these CENWAVE values, the spectral resolution peaks in the FUVB (blue) segment at  $>10^4$ , but is lower in FUYA, with average values of  $\sim 3000$ , 5000, and  $10^4$ , respectively.

We downloaded all exposures from the Hubble Legacy Archive and determined that they were processed by CALCOS v3.3.10. For each quasar, we coadded all exposures with CENWAVE 1222–1327 into a single spectrum using v3.3 of *coadd\_x1d.pro* (Danforth et al. 2010), setting BIN=3. The resulting median S/N per binned pixel over 1290–1310 Å is 11.5, with a standard deviation of 10.9 and a range of 2–52. (The low end of the range arises in a strong N V BAL in PG 1126–041.) We



**Table 2.** Summary of the Observations

Name	Range [Å]	CENWAVE [Å]	$t_{exp}$ [s]	Date	PID	PI
(1)	(2)	(3)	(4)	(5)	(6)	(7)
PG 0007+106	1151–1470	1309/1327	1868	2011-12-14	12569	S. Veilleux
PG 0026+129	1133–1451	1291/1309	1868	2011-10-25	12569	S. Veilleux
PG 0050+124	1151–1470	1309/1327	1868	2012-11-01	12569	S. Veilleux
	1133–1465	1291/1309/1327	7621	2015-01-20	13811	E. Costantini
PG 0157+001	1151–1469	1309/1327	1828	2012-01-25	12569	S. Veilleux
PG 0804+761	1136–1458	1291/1300/1309/1318	5510	2010-06-12	11686	N. Arav
PG 0838+770	1136–1458	1291/1300/1309/1318	8865	2009-09-24	11520	J. Green
PG 0844+349	1151–1470	1309/1327	1900	2012-03-06	12569	S. Veilleux
PG 0923+201	1133–1451	1291/1309	1860	2012-03-14	12569	S. Veilleux
PG 0953+414	1136–1458	1291/1300/1309/1318	4785	2011-10-18	12038	J. Green
PG 1001+054	1066–1367	1222	2068	2014-04-04	13423	R. Cooke
	1140–1455	1291/1300/1309/1318	3165	2014-06-19	13347	J. Bregman
	1131–1429	1291	2902	2019-03-26	15227	J. Burchett
PG 1004+130	1133–1451	1291/1309	4107	2011-12-21	12569	S. Veilleux
PG 1116+215	1136–1458	1291/1300/1309/1318	4677	2011-10-25	12038	J. Green
PG 1126–041	1152–1470	1309/1327	1856	2012-04-15	12569	S. Veilleux
	901–1200	1055	1874	2014-06-01	13429	M. Giustini
	1171–1467	1327	1580	2014-06-01	13429	M. Giustini
	900–1200	1055	1874	2014-06-12	13429	M. Giustini
	1171–1467	1327	1580	2014-06-12	13429	M. Giustini
	900–1200	1055	1874	2014-06-28	13429	M. Giustini
	1171–1467	1327	1580	2014-06-28	13429	M. Giustini
	901–1200	1055	1837	2015-06-14	13836	M. Giustini
	1171–1468	1327	1540	2015-06-14	13429	M. Giustini
PG 1211+143	1171–1472	1327	2320	2015-04-14	13947	J. Lee
PG 1226+023	1135–1470	1291/1300/1309/1318/1327	4002	2012-04-22	12038	J. Green
PG 1229+204	1152–1469	1309/1327	1868	2012-04-26	12569	S. Veilleux
Mrk 231	1152–1472	1309/1327	12536	2011-10-15	12569	S. Veilleux
PG 1302–102	1136–1458	1291/1300/1309/1318	5979	2011-08-16	12038	J. Green
PG 1307+085	1152–1470	1309/1327	1836	2012-06-16	12569	S. Veilleux
PG 1309+355	1133–1451	1291/1309	1896	2011-12-06	12569	S. Veilleux
PG 1351+640	1152–1470	1309/1327	2108	2011-10-21	12569	S. Veilleux
PG 1411+442	1152–1470	1309	1936	2011-10-23	12569	S. Veilleux
	941–1241	1096	4954	2015-02-12	13451	F. Hamann
	1152–1453	1309	1917	2015-02-12	13451	F. Hamann
	941–1241	1096	2407	2016-04-16	14460	F. Hamann
	1152–1453	1309	1954	2016-04-16	14460	F. Hamann
	941–1241	1096	1783	2017-06-10	14885	F. Hamann
	1152–1453	1309	1847	2017-06-10	14885	F. Hamann
PG 1435–067	1133–1451	1291/1309	1864	2012-02-29	12569	S. Veilleux
PG 1440+356	1152–1470	1309/1327	1924	2012-01-26	12569	S. Veilleux
PG 1448+273	1136–1448	1291/1309	2946	2011-06-18	12248	J. Tumlinson
PG 1501+106	1132–1434	1291	3121	2014-07-06	13448	A. Fox
PG 1613+658	1145–1467	1300/1309/1318/1327	9499	2010-04-08	11524	J. Green
	1133–1429	1291	3080	2010-04-09	11686	N. Arav
PG 1617+175	1133–1451	1291/1309	1844	2012-06-16	12569	S. Veilleux
PG 1626+554	1136–1458	1291/1300/1309/1318	3318	2011-06-15	12029	J. Green
PG 2130+099	1135–1458	1291/1300/1309/1318	5513	2010-10-28	11524	J. Green
PG 2214+139	1152–1463	1309/1327	1401	2011-11-08	12569	S. Veilleux
	1138–1434	1291	2082	2012-09-21	12604	A. Fox
PG 2233+134	1171–1472	1327	2104	2014-06-18	13423	R. Cooke
PG 2349–014	1152–1470	1309/1327	1844	2011-10-20	12569	S. Veilleux

NOTE—Column (1): Name of object; Column (2): Wavelength range, in Å; Column (3): CENWAVE setting(s); Column (4): Exposure time, in seconds; Column (5): Start date; Column (6): Proposal ID; Column (7): Program principal investigator.

separately coadded the two quasar datasets with CENWAVE 1055 and 1096.

## 5. DATA ANALYSIS

We conducted a uniform analysis of the high-ionization absorbers in our sample. In this section, we describe the methods we used to identify and characterize these absorption features.

We used v0.5 of the publicly available, IDL-based IFS-FIT package (Rupke 2014; Rupke & Veilleux 2015) to

model the absorption lines. The rest of the software used to model the data (continuum fitting, plotting, regressions) is contained in or called from our public COSQUEST repository on GitHub (Rupke 2021a).

### 5.1. Model Fitting

The starting point of the analysis is to identify the various emission and absorption lines produced by the quasars and their environments. Since our program is focused on QSO and ULIRG outflows, we only identify

and measure absorption lines within  $\sim 10,000 \text{ km s}^{-1}$  of the QSO redshifts. We refer to these lines as “associated” absorbers. Identifications of the foreground “intervening” absorbers can be found in Tripp et al. (2008), Savage et al. (2014), and Danforth et al. (2016). We first compare each quasar spectrum against a list of common UV absorbers in quasar spectra (Prochaska et al. 2001, Figure 2). We list the quasar redshifts in Table 1. Most of these redshifts are derived from narrow optical emission lines ([O III], H $\beta$ ) and may underestimate the true recession velocities since some fraction of the line emission may arise from the outflowing material itself (e.g. Rupke et al. 2017). See Teng et al. (2013) for a comparison of these measurements with the H I 21-cm emission and absorption line profiles.

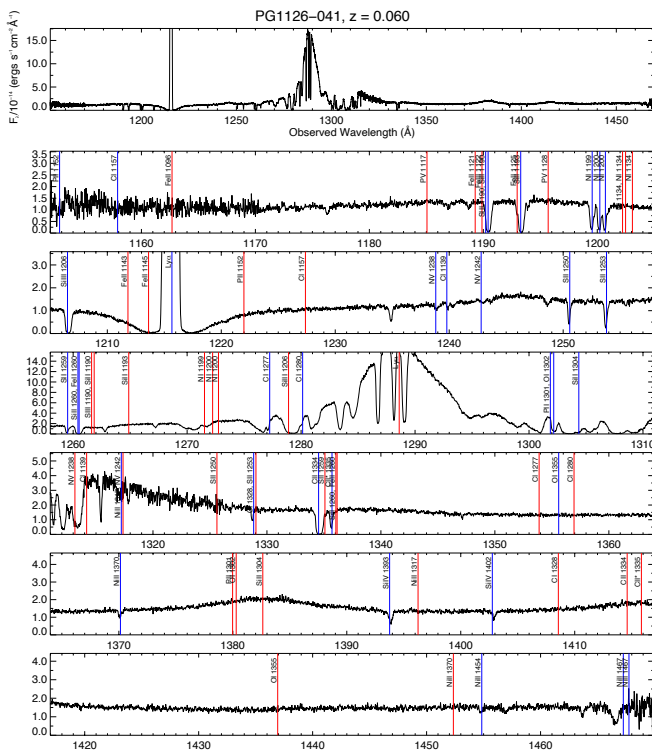


**Figure 2.** An example of a FUV spectrum used in the study. Shown here is the COS spectrum of PG 1126–041, where the data are displayed in black and the expected positions of the features in the Milky Way and quasar rest-frames are indicated in blue and red, respectively.

Next, we fit the continuum and broad line emission (Ly $\alpha$ , N V, and O VI) in three separate spectral windows around Ly $\alpha$ , N V, and O VI+Ly $\beta$ . In the two quasars in which we fit P V, this continuum region is also fit separately. Within each of these windows, we use a piecewise function of 1–4 segments in the majority of cases. In relatively featureless spectral regions, these segments are low-order polynomials. In more com-

plex spectral regions we employ cubic B-splines. The B-splines are themselves piecewise polynomials, and we separate the spline knots by a typical interval of 3 Å. We invoke BSPLINE\_ITERFIT from the SDSS IDLUTILS library to fit the B-splines.

In seven cases, the fits with piecewise functions are poorly constrained. For PG 1001+054, PG 1004+130, PG 1411+442, and PG 1617+175, PG2130+099, and PG2214+139 this is due to broad, deep absorption features over which it is difficult to fit polynomials or splines. For a seventh quasar—PG 1351+640—the poor constraints are due to several narrow absorbers near the peak of Ly $\alpha$ . In two of these cases, we instead use a Lorentzian profile to fit Ly $\alpha$ . For the five others we use the BOSS template from Harris et al. (2016), scale it multiplicatively by a low-order power law, and add a linear pedestal.

After fitting the continuum, we normalize the data in each spectral window by dividing by this fit.

We characterize the doublet absorption features (N V  $\lambda\lambda 1238, 1243$ ; O VI  $\lambda\lambda 1032, 1038$ ; and P V  $\lambda\lambda 1117, 1128$ ) in the quasar spectra using simple model fits. *Our primary objectives are to estimate the overall equivalent widths and kinematics of the outflowing gas associated with these features* (mass, momentum, and energy estimates are beyond the scope of the present paper, except for a few special cases discussed in Section 7.4). We are not aiming to derive precise column densities from the (often saturated) absorption line profiles, so the use of the precise COS line-spread function (LSF) is not required here (we return to this point at the end of this section). If the lines within these doublets were unblended, fits to the intensity profiles of the individual lines would thus be sufficient. However, the doublet lines are often strongly blended because of (1) strong blueshifts due to high outflow velocities and (2) broad line profiles due to multiple clouds along the line of sight and/or large linewidths. We thus adopt the doublet fitting procedure of Rupke et al. (2005), which is optimized for blended doublets. In this method, the total absorption profiles of a feature are fit as the product of multiple doublet components. Each component is a Gaussian in optical depth  $\tau$  vs wavelength with a constant covering factor  $C_f$ . Within each doublet the two lines have a constant  $\tau$  ratio. This allows us to simultaneously fit  $\tau$  and  $C_f$ , which are otherwise degenerate in the fit of a single line. The free parameters in the fit to each doublet component are thus  $C_f$ , peak  $\tau$ , velocity width, and central wavelength. The determination of the number of components needed in the fit is subjective and non-linear – it depends on the line complexity and data quality. The main goal here is to get a good fit to the absorption

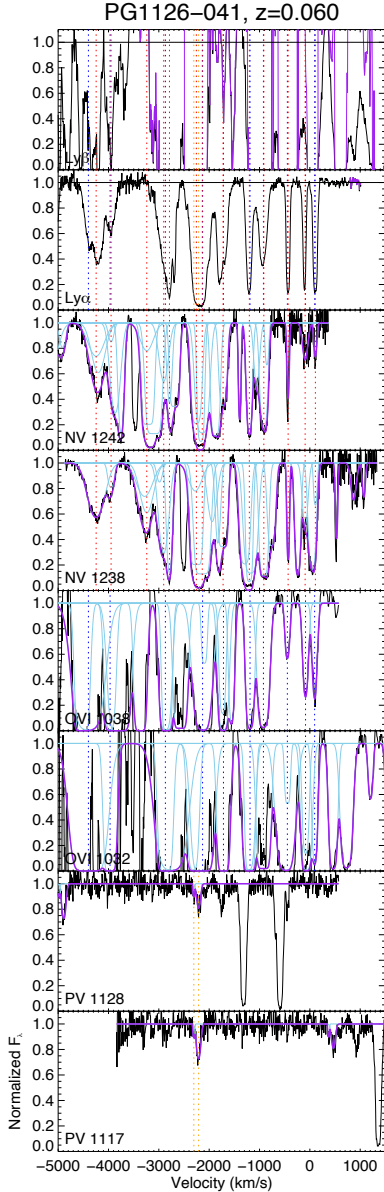


**Figure 3.** An example of interline comparison that is used to identify absorbing systems associated with the quasars. The results shown here are for PG 1126–041, produced by dividing the spectrum shown in Fig. 2 by a smooth polynomial/spline/template fit to the continuum near the key absorption lines of our study and plotting the results in velocity space in the quasar rest frame. The data are in black, the components used to fit the absorption profiles are shown in blue, and the overall fit is shown in purple. The velocity centroids of the main absorbing systems are indicated by blue (O VI) or red (Ly $\alpha$ , Ly $\beta$ , N V, P V) vertical dotted lines. The two strong lines in the panel labeled P V  $\lambda$ 1128 are Galactic ISM features without counterparts in P V  $\lambda$ 1117 or any of the other lines.

features to derive the equivalent widths and kinemat-

ics of the outflowing gas associated with these features. We do not attach a physical meaning to the individual components in the fit.

The general expression for the normalized intensity of a doublet component is

$$I(\lambda) = 1 - C_f + C_f e^{-\tau_{\text{low}}(\lambda) - \tau_{\text{high}}(\lambda)}, \quad (1)$$

where  $C_f$  is the line-of-sight covering factor (or the fraction of the background source producing the continuum that is covered by the absorbing gas; though scattering into the line of sight can also play a role) and  $\tau_{\text{low}}$  and  $\tau_{\text{high}}$  are the intrinsic optical depths of the lower- and higher-wavelength lines in the doublet (Rupke et al. 2005). The background light source is assumed to be spatially uniform. The covering factor is the same for both lines of the doublet. The peak (and total) optical depths of the resonant doublet lines in O VI, N V, and P V are related by a constant factor  $\tau_{\text{low}}/\tau_{\text{high}} = 2.00$  because of the 4-fold degeneracy in the upper state of the higher energy transition compared to the 2-fold degeneracy in the lower state. (The higher degeneracy is due in turn to its higher total angular momentum quantum number  $j$ ). For more than one doublet component, we use the product of the intensities of the individual components, which is the partially-overlapping case of Rupke et al. (2005).

Because the doublet profile shape—i.e., relative depths of the two lines and trough shape—does not change significantly above optical depths  $\tau_{\text{high}}$  of a few, we set a limit of  $\tau_{\text{high}} \leq 5$ . Out of 59 O VI components, 19 have  $\tau_{\text{high}} = 5$ , or 32%. For N V, 13 of 62 components have  $\tau_{\text{high}} = 5$ , or 21%.

The results from these fits are also used to calculate the total velocity-integrated equivalent widths of the absorbers in the object’s rest frame,

$$W_{\text{eq}} = \int [1 - f(v)] dv, \quad (2)$$

the weighted average outflow velocity,

$$v_{\text{wtavg}} = \frac{\int v [1 - f(v)] dv}{W_{\text{eq}}}, \quad (3)$$

and the weighted outflow velocity dispersion,

$$\sigma_{\text{rms}} = \left( \frac{\int (v - v_{\text{wtavg}})^2 [1 - f(v)] dv}{W_{\text{eq}}} \right)^{\frac{1}{2}}, \quad (4)$$

a measure of the second moment in velocity space of the absorbers in each quasar. These quantities are similar to those defined by Trump et al. (2006), but without the constraints on depth, width, or velocity. These constraints have little effect on the results for our sample,

but we find it useful to include possibly inflowing absorbers. Note that  $W_{\text{eq}}$ ,  $v_{\text{wtavg}}$ , and  $\sigma_{\text{rms}}$  are not corrected for partial covering. To test the impact of this assumption on our results, we have recomputed them after changing the absorption lines so that they have  $C_f = 1$  instead of the measured  $C_f$ , and then redid the regression analysis discussed in Sec. 5.2. Only very small changes of order 1% in the  $p$ -values are observed if we correct for partial covering.

Figure 3 shows the fits to the spectrum presented in Figure 2. The fits to all of the features detected in the FUV spectra of the 33 quasars in our sample are presented in Appendix A, and the results derived from these fits are tabulated in Table 3.

We computed errors in best-fit parameters and derived model quantities by refitting the model spectrum 1000 times. In each case we added Gaussian-distributed random errors to each pixel in the model with  $\sigma$  equal to the measurement error. These formal errors are small due to the high S/N in our data. Errors due to continuum placement are likely to dominate the true error budget.

We also estimated upper limits to the doublet equivalent width in cases where we did not detect N V and/or O VI. To do so, we assumed an optically-thick ( $\tau_{1243}$  or  $\tau_{1038} = 5$ ),  $v = 0$ ,  $\sigma = 50 \text{ km s}^{-1}$  absorption line. We set the covering factor equal to half the root-mean-square deviation in the continuum within  $\pm 0.5 \text{ \AA}$  of the expected rest-frame location of each line in the doublet. (The factor-of-2 accounts for fitting 2 lines instead of 1.) We set the limit equal to the resulting model equivalent width.

The optical depths and covering factors derived from our fitting scheme are approximations. Though it is a physically-motivated way to decompose strongly-blended doublets, the method implicitly assumes that the velocity dependences of  $C_f$  and  $\tau$  can be described as the sum of discrete independent Gaussians. In reality, they are probably more complex functions of velocity (e.g. Arav et al. 2005, 2008). In several cases—the N V absorbers in PG 1001+054, PG 1411+442, PG 1617+175, and PG2214+139, and the O VI absorbers in PG 1001+054 and PG 1004+130—the fits include very broad components that cannot be distinguished from complexes of narrower lines given the data quality. In two O VI absorbers (PG 0923+201 and PG 1309+355), there are no data on the blue line because it is contaminated by geocoronal Ly $\alpha$ , so any constraints on  $\tau$  and  $C_f$  come solely from line shape. Finally, in four O VI fits (PG 1001+054, PG 1004+130, PG 1126–041, and PG 1617+175), the Ly $\beta$  and O VI absorption lines blend together and cannot be easily separated in the fit. In three of these cases (all but

PG 1001+054), we simply fit the visible absorption as due solely to O VI at wavelengths in which there is at least some O VI absorption contributing to the spectrum. For the fourth case, we are able to roughly separate the lines by fitting only down to a specific wavelength. A detailed object-by-object discussion is given in Appendix A.

Despite these caveats, the fitting procedure is sufficient to meet our primary objectives of estimating the overall equivalent widths and kinematics of these features. The  $3\text{-}\sigma$  detection limit on the doublet equivalent widths is typically  $\sim 20 \text{ m\AA}$  in our data although it varies from one spectrum to the other.

We have conducted detailed tests of the impact of the COS LSF on our measurements to verify that the use of the precise COS LSF is not required here. In one series of simulations, we created a series of fake, saturated Voigt line profiles with a median S/N of 5 per pixel and line widths ranging from  $\sigma = 10 \text{ km s}^{-1}$  to  $50 \text{ km s}^{-1}$ . We convolved the profiles with the LSF downloaded from the COS website. We find that the LSF causes a difference of up to only  $\sim 10\%$  on the line width and covering fraction measurements for lines with  $\sigma \geq 20 \text{ km s}^{-1}$  (the corresponding Doppler  $b$  parameter of the Voigt profile is  $\sqrt{2} \sigma \simeq 28 \text{ km s}^{-1}$ ), which is smaller than the values measured for nearly all of the absorbers detected in our objects (Table 3). We have also run a COS LSF analysis on a ULIRG with narrow N V absorption features, taken from the sample of Paper II. Using the method described here, we get a Doppler  $b$  parameter of  $78 \text{ km s}^{-1}$  and covering fraction of 0.84, while the COS LSF gives  $83 \text{ km s}^{-1}$  and 0.82, respectively, confirming that the results for the relatively broad absorbers reported in the present paper are reliable.

## 5.2. Regressions

To search for connections between outflow and quasar/host properties, we computed linear regressions between the properties in Tables 1 and 3. In most cases, we apply the Bayesian model in LINMIX\_ERR (Kelly 2007). We use the Metropolis-Hastings sampler and a single Gaussian to represent the distribution of quasar/host parameters (except for  $W_{\text{eq}}$  vs. AGN fraction, for which we used NGAUSS=3). LINMIX\_ERR permits censored y-values, which is the case for  $W_{\text{eq}}$ .

When we compute the regressions for the independent variable  $N_{\text{H}}$ , however, the x-axis values are also censored. In this case we turn to the method of Isobe et al. (1986) for computing the Kendall tau correlation coefficient with censored data in both axes. We use the implementation of pymccorrelation (Privon et al. 2020), which in turn perturbs the data in Monte Carlo fash-

**Table 3.** Results from the Multi-Component Fits to the Absorbers

Name	Line	$W_{\text{eq}}$ Å	$v_{\text{wtavg}}$ km s <sup>-1</sup>	$\sigma_{\text{rms}}$ km s <sup>-1</sup>	# comp.
(1)	(2)	(3)	(4)	(5)	(6)
PG0007+106	N V	<0.16			
PG0026+129	N V	<0.09			
	O VI	<0.12			
PG0050+124	N V	$0.88^{+0.019}_{-0.017}$	$-1106.3^{+19.0}_{-18.7}$	$595.0^{+18.0}_{-16.4}$	6
PG0157+001	N V	<0.13			
	O VI	<0.09			
PG0804+761	N V	$0.02^{+0.003}_{-0.003}$	$591.0^{+1.8}_{-1.7}$	$12.3^{+1.9}_{-1.8}$	1
	O VI	$0.18^{+0.009}_{-0.007}$	$571.0^{+1.6}_{-1.5}$	$27.8^{+1.1}_{-1.1}$	1
PG0838+770	N V	<0.12			
	O VI	<0.06			
PG0844+349	N V	$0.73^{+0.011}_{-0.011}$	$151.4^{+0.8}_{-0.8}$	$31.8^{+0.5}_{-0.5}$	2
PG0923+201	O VI	$4.48^{+0.072}_{-0.072}$	$-3048.3^{+11.4}_{-11.9}$	$335.6^{+9.3}_{-8.7}$	1
PG0953+414	O VI	$0.20^{+0.006}_{-0.006}$	$-825.4^{+14.7}_{-13.9}$	$418.3^{+7.2}_{-7.1}$	2
PG1001+054	N V	$6.07^{+0.058}_{-0.059}$	$-5969.9^{+24.0}_{-37.4}$	$1326.5^{+18.0}_{-11.7}$	4
	O VI	$11.61^{+0.080}_{-0.072}$	$-5743.9^{+33.2}_{-83.1}$	$1092.4^{+32.7}_{-27.6}$	6
PG1004+130	O VI	$24.29^{+0.245}_{-0.277}$	$-5335.7^{+80.0}_{-75.4}$	$2970.2^{+72.3}_{-47.4}$	12
PG1116+215	O VI	$0.27^{+0.008}_{-0.008}$	$-2271.6^{+43.2}_{-46.3}$	$908.7^{+22.1}_{-25.6}$	2
PG1126-041	N V	$10.66^{+0.037}_{-0.034}$	$-2085.5^{+10.0}_{-9.8}$	$1076.1^{+6.9}_{-7.2}$	13
	O VI	$16.80^{+1.891}_{-1.616}$	$-2559.2^{+298.8}_{-251.5}$	$1482.2^{+132.6}_{-169.4}$	10
	P V	$0.21^{+0.017}_{-0.017}$	$-2234.2^{+5.9}_{-6.1}$	$48.2^{+4.3}_{-3.8}$	2
PG1211+143	N V	<0.05			
PG1226+023	N V	<0.04			
	O VI	<0.04			
PG1229+204	N V	<0.09			
Mrk 231	N V	<0.18			
PG1302-102	O VI	<0.05			
PG1307+085	N V	<0.10			
	O VI	$0.15^{+0.017}_{-0.016}$	$-3406.2^{+11.9}_{-14.1}$	$66.8^{+11.8}_{-14.1}$	2
PG1309+355	O VI	$8.57^{+0.038}_{-0.031}$	$-893.9^{+4.9}_{-4.7}$	$364.5^{+3.2}_{-3.1}$	7
PG1351+640	N V	$4.36^{+0.036}_{-0.034}$	$-1264.4^{+10.0}_{-11.4}$	$428.4^{+4.8}_{-3.8}$	9
PG1411+442	N V	$10.30^{+0.019}_{-0.018}$	$-1594.8^{+2.6}_{-2.4}$	$562.7^{+2.5}_{-2.3}$	4
	P V	$0.83^{+0.028}_{-0.028}$	$-1754.6^{+5.9}_{-5.5}$	$131.0^{+3.8}_{-3.6}$	2
PG1435-067	N V	<0.15			
	O VI	<0.08			
PG1440+356	N V	$0.89^{+0.023}_{-0.021}$	$-1478.4^{+28.1}_{-26.7}$	$775.3^{+27.0}_{-25.8}$	3
PG1448+273	N V	$3.22^{+0.038}_{-0.033}$	$-229.8^{+2.2}_{-2.1}$	$164.1^{+1.0}_{-1.0}$	4
PG1613+658	N V	$0.14^{+0.005}_{-0.004}$	$-3714.6^{+6.1}_{-5.5}$	$121.8^{+3.2}_{-3.6}$	2
	O VI	$0.68^{+0.008}_{-0.008}$	$-3691.1^{+2.0}_{-1.8}$	$126.6^{+0.8}_{-0.8}$	2
PG1617+175	N V	$3.00^{+0.059}_{-0.055}$	$-3094.7^{+19.9}_{-23.8}$	$526.8^{+34.3}_{-22.5}$	5
	O VI	$6.08^{+0.173}_{-0.173}$	$-3323.7^{+113.3}_{-133.0}$	$920.2^{+83.2}_{-71.6}$	8
	P V	$0.06^{+0.040}_{-0.033}$	$-3355.0^{+55.1}_{-38.0}$	$42.1^{+46.1}_{-25.8}$	1
PG1626+554	N V	<0.08			
	O VI	<0.06			
PG2130+099	N V	$0.76^{+0.013}_{-0.013}$	$-1312.3^{+9.9}_{-9.6}$	$540.3^{+9.5}_{-9.3}$	3
PG2214+139	N V	$8.01^{+0.024}_{-0.023}$	$-1461.1^{+17.9}_{-17.9}$	$681.7^{+21.9}_{-20.2}$	5
PG2233+134	O VI	$0.17^{+0.025}_{-0.024}$	$-211.2^{+3.0}_{-3.0}$	$17.3^{+3.2}_{-2.9}$	1
PG2349-014	N V	<0.12			

NOTE—Column (1): Name of object. Column (2): N V means N V  $\lambda$ 1238, 1243, O VI means O VI  $\lambda$ 1032, 1038, and P V means P V  $\lambda$ 1117, 1128. N V or O VI is not listed when it lies outside of the spectral range of the data. Column (3): Velocity-integrated equivalent widths (eq. 2). Column (4): Average depth-weighted outflow velocity (eq. 3), which is a measure of the average velocity of the outflow systems in each object. Column (5): Average depth-weighted outflow velocity dispersion (eq. 4), which is a measure of the range in velocity of the outflow systems in each quasar. Column (6): Number of absorption components.

ion to compute the errors in the correlation coefficient (Curran 2014).

For both regression methods, we computed the significance of a correlation as the fraction of cross-correlation values  $r < 0$  ( $r > 0$ ) for a positive (negative) best-fit  $r$ . For LINMIX\_ERR, the  $r$  values are draws from the posterior distribution, while for pymccorrelation they are results of the Monte Carlo perturbations.

We do not consider the N V and O VI points independent for the purposes of the regressions. Therefore, where both doublets are present in the data for a given quasar, we compute the average measurement (either detection or limit) from the two lines. If only one line is detected, we use that measurement rather than averaging a detection and a limit. Where multiple X-ray measurements exist for a quasar, we take the average. Errors in  $L_{\text{BOL}}$ ,  $L_{\text{IR}}/L_{\text{BOL}}$ ,  $L_{\text{FIR}}/L_{\text{BOL}}$ , and  $\alpha_{\text{OX}}$  are unknown, so for the purposes of regression we fix the errors to 0.1 dex. For  $\nu L_{\nu}(\text{UV})$ , we ignore the negligible statistical measurement errors.

## 6. RESULTS

The results from our spectral analysis of the *HST* spectra are summarized in Table 3. In this section, we investigate whether the presence or nature of quasar-driven outflows and starburst winds correlate with the properties of the quasars and host galaxies. The quantities that we consider in our correlation matrix are listed in Table 1 and defined in the notes to that table. The results from the statistical and regression analyses are summarized in Tables 4 and 5.

Note that we do not make a distinction between quasar-driven outflows and starburst-driven winds in this section, and we only consider absorption lines within  $10,000 \text{ km s}^{-1}$  of the QSO redshift (inclusion of lines at greater displacements leads to unacceptable contamination by intervening absorbers). A more comprehensive assessment of the detected outflows is conducted in Section 7, after we have considered the line profiles more fully, including signs of saturation and/or partial covering of the continuum source (Sec. 6.2) and the overall kinematics of the outflowing gas (Sec. 6.4). Similarly, the comparison of our results with those from previous studies is postponed until Section 7, once the results from our spectral analysis have been fully presented.

### 6.1. Rate of Incidence of Outflows

Figures 4 and 5 show the median velocities in the quasar rest frame of all of the detected N V and O VI absorption-line systems, sorted from top to bottom by decreasing redshift and bolometric luminosity, respectively. The first of these figures clearly illustrates the

fact mentioned in Section 4 that our ability to detect the N V and O VI features is limited by the spectral coverage of the COS data to  $z \lesssim 0.18$  and  $z \gtrsim 0.11$ , respectively (systems outside of the spectral range are indicated by an “x” in this figure and Fig. 5).

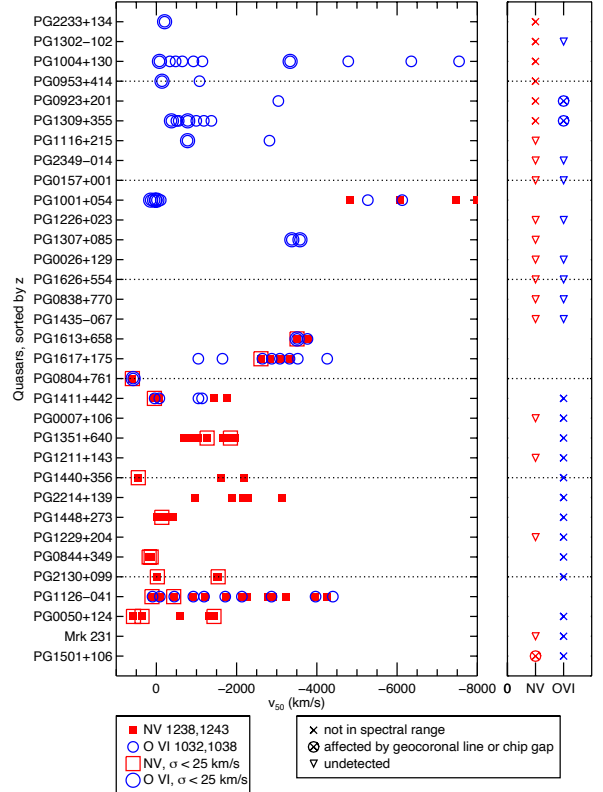


**Figure 4.** Median velocities of the N V and O VI absorbing systems detected in the QUEST quasars of our sample. Note that the faster outflows with more negative velocities lie on the right in this figure. The objects are sorted from top to bottom in order of decreasing redshift. Red symbols mark N V  $\lambda\lambda 1238, 1243$  and blue symbols mark O VI  $\lambda\lambda 1032, 1038$ . Open symbols indicate systems with velocity dispersion  $\sigma < 25 \text{ km s}^{-1}$ . The two columns on the right indicate whether N V (red) or O VI (blue) is within the spectral range of the data (“x” indicates that it is not), affected by geocoronal line or chip gap (encircled “x”), or simply undetected (downward-pointing triangle). A lack of symbol marks a detection.

A cursory examination of Figures 4 and 5 shows that blueshifted N V or O VI absorption systems suggestive of outflows (with equivalent widths above our  $3\text{-}\sigma$  detection limit of  $\sim 20 \text{ m}\text{\AA}$ ) are detected in about 60% of the quasars in our sample, and there is no obvious trend in the rate of incidence with redshift or bolometric luminosity.

The results of a more quantitative analysis based on  $\beta$  distributions (Cameron 2011) are listed in Table 4. The

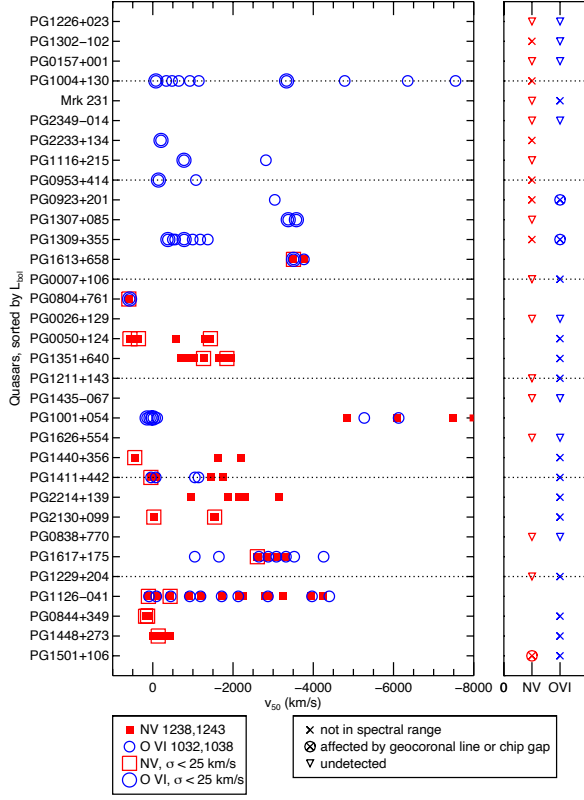


**Figure 5.** Same as Fig. 4, but the objects are sorted from top to bottom in order of decreasing bolometric luminosity.

overall rate of incidence of N V or O VI absorbers is 61% with a 1- $\sigma$  range of (52% – 68%), once taking into account the spectral coverage of the data. This rate is virtually the same for N V and O VI. Among quasars with  $\log L_{\text{BOL}}/L_{\odot} > 12.0$ , this rate is 61% with a 1- $\sigma$  range of (49% – 71%), while it is 60% (47% – 71%) among the systems of lower luminosities. These rates are thus not significantly different from each other, and are similar to the rate of incidence of O VI outflows in local Seyfert 1 galaxies (Kris 2004a,b) as well as C IV (Crenshaw et al. 1999) or X-ray (Reynolds 1997; George et al. 1998) absorption.

We have also searched for trends between the rate of incidence of outflows and several other quantities. The detection rate of outflows (79%) among quasars that have strongly absorbed X-ray continua ( $N_{\text{H}} > 10^{22} \text{ cm}^{-2}$ ) is significantly higher than those that do not (25%) (Table 4). These rates differ at the 2- $\sigma$  level (95.4%), where the ranges of the incidence rate are 56 – 92% for quasars with absorbed X-ray continua and 9 – 54% for the others. Using the `scipy.stats` implementation of the Fisher exact test, the null hypothesis that galaxies with strongly- and weakly-absorbed X-ray continua UV absorbers are equally likely to show N V or O VI absorbers is rejected at the 99.2% level. The

**Table 4.** Rate of Incidence of Outflows

Line	Detection	Total	Fraction (1- $\sigma$ range)
(1)	(2)	(3)	(4)
All Quasars			
N V	13	27	0.48 (0.39 – 0.58)
O VI	12	20	0.60 (0.49 – 0.70)
Both	5	14	0.36 (0.25 – 0.50)
Any	20	33	0.61 (0.52 – 0.68)
$\log L_{\text{BOL}}/L_{\odot} \geq 12.0$			
N V	4	12	0.33 (0.23 – 0.48)
O VI	9	14	0.64 (0.50 – 0.75)
Both	2	8	0.25 (0.16 – 0.44)
Any	11	18	0.61 (0.49 – 0.71)
$\log L_{\text{BOL}}/L_{\odot} < 12.0$			
N V	9	15	0.60 (0.47 – 0.71)
O VI	3	6	0.50 (0.32 – 0.68)
Both	3	6	0.50 (0.32 – 0.68)
Any	9	15	0.60 (0.47 – 0.71)
$N_{\text{H}} > 10^{22} \text{ cm}^{-2}$			
N V	10	16	0.62 (0.50 – 0.73)
O VI	8	8	1.00 (0.81 – 0.98)
Both	3	5	0.60 (0.38 – 0.76)
Any	15	19	0.79 (0.67 – 0.85)
$N_{\text{H}} \leq 10^{22} \text{ cm}^{-2}$			
N V	2	10	0.20 (0.13 – 0.37)
O VI	2	10	0.20 (0.13 – 0.37)
Both	1	8	0.12 (0.08 – 0.32)
Any	3	12	0.25 (0.17 – 0.41)
$\alpha_{\text{ox}} \geq -1.6$			
N V	7	17	0.41 (0.31 – 0.53)
O VI	6	12	0.50 (0.37 – 0.63)
Both	2	9	0.22 (0.14 – 0.41)
Any	11	20	0.55 (0.44 – 0.65)
$\alpha_{\text{ox}} < -1.6$			
N V	6	9	0.67 (0.49 – 0.78)
O VI	6	7	0.86 (0.64 – 0.91)
Both	3	4	0.75 (0.48 – 0.85)
Any	9	12	0.75 (0.59 – 0.83)

NOTE—Column (1): Feature(s) used in the statistical analysis. “Both” means both N V and O VI doublets and “Any” means either N V or O VI doublet or both; Column (2): Number of objects with detected outflows; Column (3): Number of objects in total with the appropriate redshift; Column (4): Fraction of objects with detected outflows. The two numbers in parentheses indicate the 1- $\sigma$  range (68% probability) of the fraction of objects with detected outflows, computed from the  $\beta$  distribution (Cameron 2011).

**Table 5.** Linear Regression Results

$y$	$x$	$N$	$p$	$r$
(1)	(2)	(3)	(4)	(5)
$W_{\text{eq}}$	$\log(L_{\text{BOL}}/L_{\odot})$	32	0.046	$-0.34^{+0.19}_{-0.17}$
$W_{\text{eq}}$	$\log[\lambda L_{1125}/\text{erg s}^{-1}]$	32	0.140	$-0.22^{+0.25}_{-0.21}$
$W_{\text{eq}}$	AGN fraction	32	0.094	$0.78^{+0.19}_{-0.61}$
$W_{\text{eq}}$	$\log(L_{\text{AGN}}/L_{\odot})$	32	0.054	$-0.33^{+0.19}_{-0.16}$
$W_{\text{eq}}$	$\log(M_{\text{BH}}/M_{\odot})$	32	0.289	$-0.33^{+0.55}_{-0.43}$
$W_{\text{eq}}$	Eddington Ratio	32	0.168	$-0.42^{+0.44}_{-0.38}$
$W_{\text{eq}}$	$\frac{\alpha_{\text{OX}}}{\log(L_{\text{IR}}/L_{\text{BOL}})}$	31	0.002	$-0.62^{+0.17}_{-0.13}$
$W_{\text{eq}}$	$\log(L_{\text{FIR}}/L_{\text{BOL}})$	32	0.067	$0.37^{+0.20}_{-0.25}$
$W_{\text{eq}}$	$\log[L_{\text{FIR}}/L_{\text{BOL}}]$	30	0.094	$-0.29^{+0.22}_{-0.19}$
$W_{\text{eq}}$	$\log[N(\text{H})/\text{cm}^{-2}]$	30	<0.001	$0.19^{+0.03}_{-0.03}$
$W_{\text{eq}}$	$\Gamma$	30	0.143	$0.25^{+0.20}_{-0.23}$
$W_{\text{eq}}$	$\log[F(0.5 - 2 \text{ keV})/\text{erg s}^{-1} \text{ cm}^{-2}]$	26	0.005	$-0.54^{+0.18}_{-0.14}$
$W_{\text{eq}}$	$\log[F(2 - 10 \text{ keV})/\text{erg s}^{-1} \text{ cm}^{-2}]$	29	0.002	$-0.55^{+0.18}_{-0.14}$
$W_{\text{eq}}$	$\log[L(0.5 - 2 \text{ keV})/\text{erg s}^{-1}]$	26	0.072	$-0.33^{+0.22}_{-0.20}$
$W_{\text{eq}}$	$\log[L(2 - 10 \text{ keV})/\text{erg s}^{-1}]$	30	0.009	$-0.51^{+0.20}_{-0.15}$
$W_{\text{eq}}$	$\log[L(0.5 - 10 \text{ keV})/\text{erg s}^{-1}]$	26	0.051	$-0.38^{+0.23}_{-0.18}$
$W_{\text{eq}}$	$\log[L(0.5 - 2 \text{ keV})/L(0.5 - 10 \text{ keV})]$	26	0.192	$0.21^{+0.22}_{-0.24}$
$W_{\text{eq}}$	$\log[L(0.5 - 10 \text{ keV})/L_{\text{BOL}}]$	26	0.211	$-0.20^{+0.25}_{-0.21}$
$v_{\text{wtavg}}$	$\log(L_{\text{BOL}}/L_{\odot})$	20	0.138	$-0.27^{+0.25}_{-0.25}$
$v_{\text{wtavg}}$	$\log[\lambda L_{1125}/\text{erg s}^{-1}]$	20	0.283	$-0.15^{+0.25}_{-0.22}$
$v_{\text{wtavg}}$	$\alpha_{\text{OX}}$	20	0.103	$0.31^{+0.21}_{-0.24}$
$v_{\text{wtavg}}$	$\log(L_{\text{IR}}/L_{\text{BOL}})$	20	0.115	$0.37^{+0.25}_{-0.30}$
$v_{\text{wtavg}}$	$\log(L_{\text{FIR}}/L_{\text{BOL}})$	20	0.496	$0.00^{+0.25}_{-0.26}$
$v_{\text{wtavg}}$	AGN fraction	20	0.340	$0.35^{+0.49}_{-0.30}$
$v_{\text{wtavg}}$	$\log(L_{\text{AGN}}/L_{\odot})$	20	0.150	$-0.24^{+0.23}_{-0.21}$
$v_{\text{wtavg}}$	$\log(M_{\text{BH}}/M_{\odot})$	20	0.286	$-0.31^{+0.56}_{-0.42}$
$v_{\text{wtavg}}$	Eddington Ratio	20	0.414	$0.13^{+0.53}_{-0.59}$
$v_{\text{wtavg}}$	$\log[N(\text{H})/\text{cm}^{-2}]$	18	0.034	$-0.15^{+0.08}_{-0.08}$
$v_{\text{wtavg}}$	$\Gamma$	18	0.011	$0.67^{+0.14}_{-0.22}$
$v_{\text{wtavg}}$	$\log[F(0.5 - 2 \text{ keV})/\text{erg s}^{-1} \text{ cm}^{-2}]$	17	0.008	$0.61^{+0.15}_{-0.21}$
$v_{\text{wtavg}}$	$\log[F(2 - 10 \text{ keV})/\text{erg s}^{-1} \text{ cm}^{-2}]$	17	0.016	$0.57^{+0.16}_{-0.23}$
$v_{\text{wtavg}}$	$\log[L(0.5 - 2 \text{ keV})/\text{erg s}^{-1}]$	17	0.087	$0.36^{+0.22}_{-0.26}$
$v_{\text{wtavg}}$	$\log[L(2 - 10 \text{ keV})/\text{erg s}^{-1}]$	18	0.264	$0.17^{+0.25}_{-0.28}$
$v_{\text{wtavg}}$	$\log[L(0.5 - 10 \text{ keV})/\text{erg s}^{-1}]$	17	0.211	$0.23^{+0.25}_{-0.28}$
$v_{\text{wtavg}}$	$\log[L(0.5 - 2 \text{ keV})/L(0.5 - 10 \text{ keV})]$	17	0.006	$0.69^{+0.13}_{-0.20}$
$v_{\text{wtavg}}$	$\log[L(0.5 - 10 \text{ keV})/L_{\text{BOL}}]$	17	0.009	$0.64^{+0.14}_{-0.20}$
$\sigma_{\text{rms}}$	$\log(L_{\text{BOL}}/L_{\odot})$	20	0.238	$0.18^{+0.23}_{-0.25}$
$\sigma_{\text{rms}}$	$\log[\lambda L_{1125}/\text{erg s}^{-1}]$	20	0.425	$-0.04^{+0.24}_{-0.24}$
$\sigma_{\text{rms}}$	$\frac{\alpha_{\text{OX}}}{\log(L_{\text{IR}}/L_{\text{BOL}})}$	20	0.004	$-0.55^{+0.20}_{-0.15}$
$\sigma_{\text{rms}}$	$\log(L_{\text{IR}}/L_{\text{BOL}})$	20	0.305	$-0.16^{+0.32}_{-0.30}$
$\sigma_{\text{rms}}$	$\log(L_{\text{FIR}}/L_{\text{BOL}})$	20	0.433	$-0.04^{+0.25}_{-0.25}$
$\sigma_{\text{rms}}$	AGN fraction	20	0.389	$-0.13^{+0.55}_{-0.58}$
$\sigma_{\text{rms}}$	$\log(L_{\text{AGN}}/L_{\odot})$	20	0.247	$0.17^{+0.23}_{-0.25}$
$\sigma_{\text{rms}}$	$\log(M_{\text{BH}}/M_{\odot})$	20	0.301	$0.29^{+0.43}_{-0.59}$
$\sigma_{\text{rms}}$	Eddington Ratio	20	0.374	$-0.18^{+0.58}_{-0.49}$
$\sigma_{\text{rms}}$	$\log[N(\text{H})/\text{cm}^{-2}]$	18	0.086	$0.10^{+0.08}_{-0.07}$
$\sigma_{\text{rms}}$	$\Gamma$	18	0.048	$-0.46^{+0.26}_{-0.20}$
$\sigma_{\text{rms}}$	$\log[F(0.5 - 2 \text{ keV})/\text{erg s}^{-1} \text{ cm}^{-2}]$	17	0.016	$-0.56^{+0.22}_{-0.16}$
$\sigma_{\text{rms}}$	$\log[F(2 - 10 \text{ keV})/\text{erg s}^{-1} \text{ cm}^{-2}]$	17	0.015	$-0.55^{+0.22}_{-0.16}$
$\sigma_{\text{rms}}$	$\log[L(0.5 - 2 \text{ keV})/\text{erg s}^{-1}]$	17	0.066	$-0.40^{+0.26}_{-0.21}$
$\sigma_{\text{rms}}$	$\log[L(2 - 10 \text{ keV})/\text{erg s}^{-1}]$	18	0.137	$-0.28^{+0.26}_{-0.23}$
$\sigma_{\text{rms}}$	$\log[L(0.5 - 10 \text{ keV})/\text{erg s}^{-1}]$	17	0.120	$-0.32^{+0.27}_{-0.23}$
$\sigma_{\text{rms}}$	$\log[L(0.5 - 2 \text{ keV})/L(0.5 - 10 \text{ keV})]$	17	0.022	$-0.54^{+0.24}_{-0.18}$
$\sigma_{\text{rms}}$	$\log[L(0.5 - 10 \text{ keV})/L_{\text{BOL}}]$	17	0.008	$-0.61^{+0.21}_{-0.15}$

NOTE—Column (1): Dependent variable (absorption line property). Column (2): Independent variable (quasar/host property). Column (3): Number of points. Column (4):  $p$ -value of null hypothesis (no correlation). Column (5): Correlation coefficient and  $1\sigma$  errors. Underlined entries under col. (2) indicate significant correlations with  $p$ -values below 0.05.

rate of incidence of outflows among quasars with a steep X-ray to optical spectral index ( $\alpha_{\text{OX}} < -1.6$ ; 75%) is also higher than those with a shallow index (55%), although the Fisher exact test shows that this difference is not significant ( $p = 0.45$ ). A similar dependence on the X-ray properties of the quasars has been reported in several studies of higher luminosity quasars and lower luminosity Seyfert 1 galaxies using C IV  $\lambda\lambda 1548, 1550$  as a tracer of warm ionized outflows. We return to this result in Sections 6.3 and 6.4, and 7.

## 6.2. Optical Depths and Covering Factors

The distributions of the N V  $\lambda 1243$  and O VI  $\lambda 1038$  optical depths and covering factors derived from the individual components in the multi-component fits are presented as histograms in Figure 6.

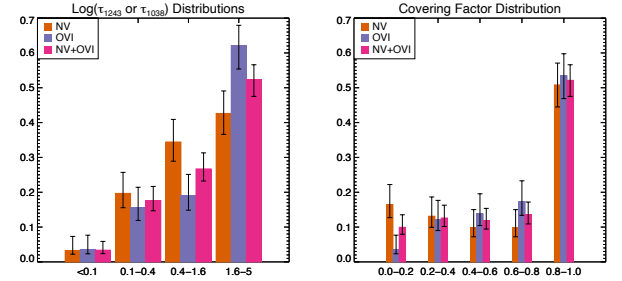


**Figure 6.** Distributions of the optical depths (left) and covering factors (right) of the individual components used to fit the profiles of the N V (orange), O VI (purple), or joint N V + O VI (pink) absorption features.

Again, we repeat that the optical depths and covering factors presented here are only approximations. Nevertheless, it is clear from the left panel in Figure 6 that a significant fraction of the absorbing systems are affected by saturation effects ( $\tau_{1243}$  or  $\tau_{1038} > 1$ ), therefore making the equivalent widths of the N V and O VI features unreliable indicators of the total column densities of highly ionized gas in many of these cases.

The right panel of Figure 6 shows that the mode of the distribution of covering factors is consistent with unity, but  $\sim 50\%$  of the N V and O VI absorbers only partially cover the FUV quasar continuum emission (+ possibly the broad emission line region – BELR; Fig. 6), consistent with small clouds located relatively near the quasars. As described at the end of Sec. 5.1, emission inflow of the absorption profiles associated with the broad wings of the COS LSF is negligible and thus does not affect this conclusion. We return to this result in Section 7.1.

## 6.3. Outflow Equivalent Widths



The velocity-integrated equivalent widths ( $W_{\text{eq}}$ ; eq. 2) of the outflow systems in each quasar are listed in Table 3. They span a broad range from  $\sim 25 \text{ \AA}$  down to  $20 \text{ m\AA}$ , near our  $3\text{-}\sigma$  detection limit.

The equivalent widths of the outflows were compared against the properties of the quasars and host galaxies listed in Table 1. Some of the results are shown in Figure 7. By and large, we do not find any significant trends between  $W_{\text{eq}}$  and any of the quasar and host properties, except with some of the quantities that are derived from the X-ray data (Table 5). Taken at face value, this result is surprising since, for instance, it means that the equivalent width of the outflow is largely agnostic of the properties of the central engine over a range of  $\sim 1.5$  dex in power (FUV, bolometric, or quasar-only luminosity),  $\sim 2.0$  dex in Eddington ratio, and  $\sim 2.5$  dex in black hole mass. The lack of correlations with the properties of the hosts is less surprising since the quasar sample spans a relatively narrow range of values in these quantities so the lack of correlation with these quantities may be attributed to the lower dynamical range.

Examples of trends between  $W_{\text{eq}}$  and the X-ray properties of the quasars are shown in panels (e), (f), and (g) of Figure 7. In panel (e), the equivalent width of the outflow decreases with increasing HX luminosity. Panel (f) in this figure illustrates the dependence of the rate of incidence of these outflows on the X-ray column densities already pointed out in Section 6.1. The stronger highly ionized outflows with  $W_{\text{eq}} \gtrsim 1 \text{ \AA}$  are only present in quasars with X-ray column densities above  $\sim 10^{22} \text{ cm}^{-2}$ . While it is a required condition for a strong outflow, it is not a sufficient condition since most quasars with these X-ray absorbing column densities show either weak outflows in the FUV ( $W_{\text{eq}} < 0.3 \text{ \AA}$ ) or none at all. Panel (g) also shows a distinct trend for strong outflows with  $W_{\text{eq}} \gtrsim 1 \text{ \AA}$  among objects with  $\alpha_{\text{OX}} \lesssim -1.7$ . A similar trend is observed when normalizing the X-ray luminosities to the bolometric luminosities (not shown), but disappears when considering only the X-ray slope (e.g. the SX/HX ratio or index of the best-fit absorbed power-law distribution to the X-rays; not shown). Similar results have been found when considering C IV outflows (e.g. Brandt et al. 2000; Laor & Brandt 2002; Baskin & Laor 2005; Gibson et al. 2009a,b). We return to this issue in Section 7 below.

#### 6.4. Outflow Kinematics

Figure 8 shows the distributions of the velocity centroids and dispersions ( $\sigma$ ) of the various individual components that were used to fit the N V and O VI absorbers in the quasar sample. About half of all of the individual components have blueshifted (outflow) velocities

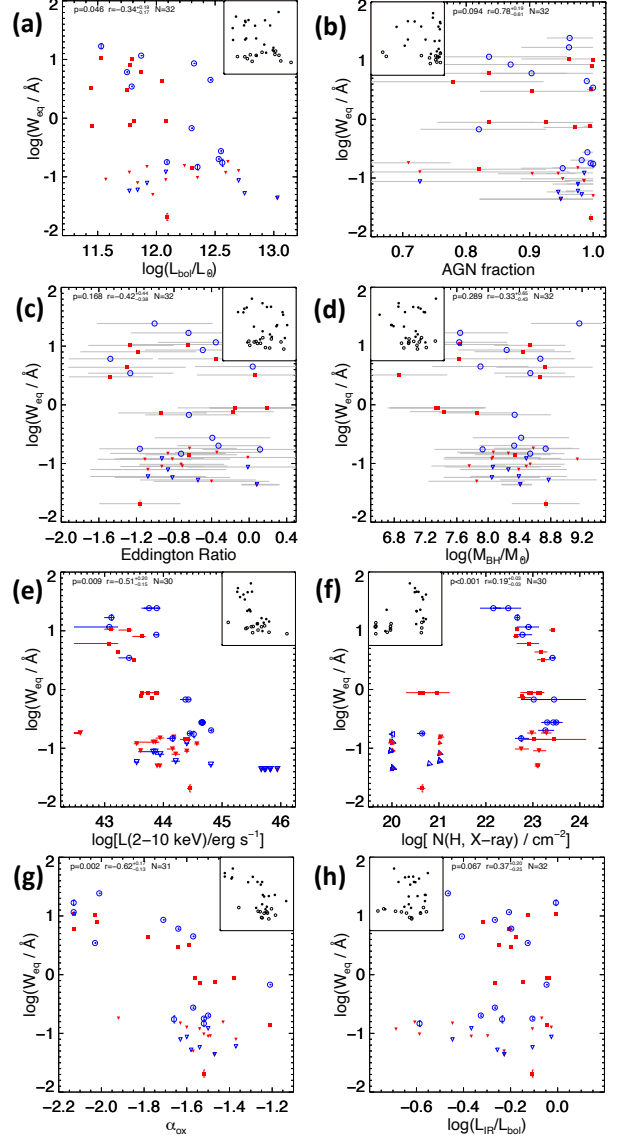


**Figure 7.** The velocity-integrated equivalent widths,  $W_{\text{eq}}$ , of the outflow systems in the QUEST quasars are plotted as a function of the (a) bolometric luminosities, (b) AGN bolometric fractions, (c) Eddington ratios, (d) black hole masses, (e) hard X-ray ( $2 - 10 \text{ keV}$ ) luminosities, (f) X-ray absorbing column densities, (g) X-ray to optical spectral indices, and (h) ratios of the infrared luminosities to the bolometric luminosities. Red squares mark N V  $\lambda\lambda 1238, 1243$  and blue circles mark O VI  $\lambda\lambda 1032, 1038$ . Triangles indicate upper limits (in one or both quantities). The regression results ( $p$ -values, correlation coefficients  $r$  with  $1\sigma$  errors, and number of points  $N$ ; Section 5) are shown at the top of each panel. The actual points used in the regression, in which N V and O VI quantities and/or X-ray measurements are averaged for a given quasar, are shown in each inset panel. The solid points are detections, while the open points are censored values in one or both quantities plotted.

that lie between  $[-2000, 0] \text{ km s}^{-1}$  and have  $1\text{-}\sigma$  widths

less than  $40 \text{ km s}^{-1}$ . In a blindly selected sample of O VI absorbers, Tripp et al. (2008) similarly found that the majority of associated absorbers are within  $2000 \text{ km s}^{-1}$  of the QSO redshift (see their Figure 15). Likewise, they found that the O VI line widths are  $< 40 \text{ km s}^{-1}$ . Up to  $\sim 10\%$  of the individual components in the present survey have redshifted velocities of up to a few  $\times 100 \text{ km s}^{-1}$ ; some of them may be attributed to uncertain or systematically blueshifted systemic velocities derived from the quasar emission lines (Sec. 5) rather than actual inflows.

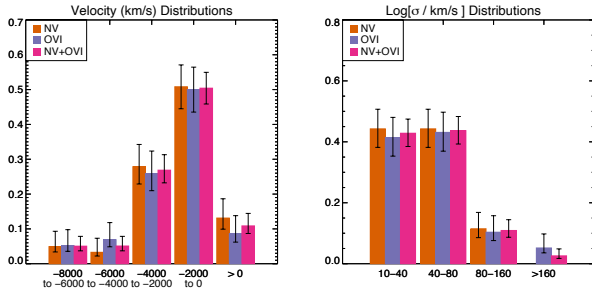


**Figure 8.** Distributions of the median velocities (left) and velocity dispersions (right) of the individual components used to fit the profiles of the N V (orange), O VI (purple), and joint N V + O VI (pink) absorption features.

More physically meaningful kinematic quantities are the weighted average velocities and velocity dispersions of the outflow systems in each object (eqs. 3 and 4). Of the 20 detected absorbers in Table 3, 8 (3) have weighted average outflow velocities (velocity dispersion) in excess of  $2000$  ( $1000$ )  $\text{km s}^{-1}$ .

We find in Table 5 that there is no distinct trend between the weighted outflow velocities and velocity dispersions and the quasar and host properties, except for the lack of outflows in X-ray unabsorbed quasars (Fig. 10), pointed out in Sec. 6.1, and the larger weighted outflow velocity dispersions among X-ray faint sources with  $\alpha_{\text{OX}} \lesssim -2$ . The lack of a correlation between outflow velocities and the quasar luminosities seems at odds with those from most previous C IV absorption-line studies (e.g. Perry & O’Dell 1978; Brandt et al. 2000; Laor & Brandt 2002; Ganguly et al. 2007; Ganguly & Brotherton 2008; Gibson et al. 2009a,b; Zhang et al. 2014; Rankine et al. 2020) and other multi-wavelength analyses (e.g., references in Sec. 1 and Veilleux et al. 2020). We examine this issue in more detail in Section 7 below.

## 7. DISCUSSION

### 7.1. Origins of the Absorption Features

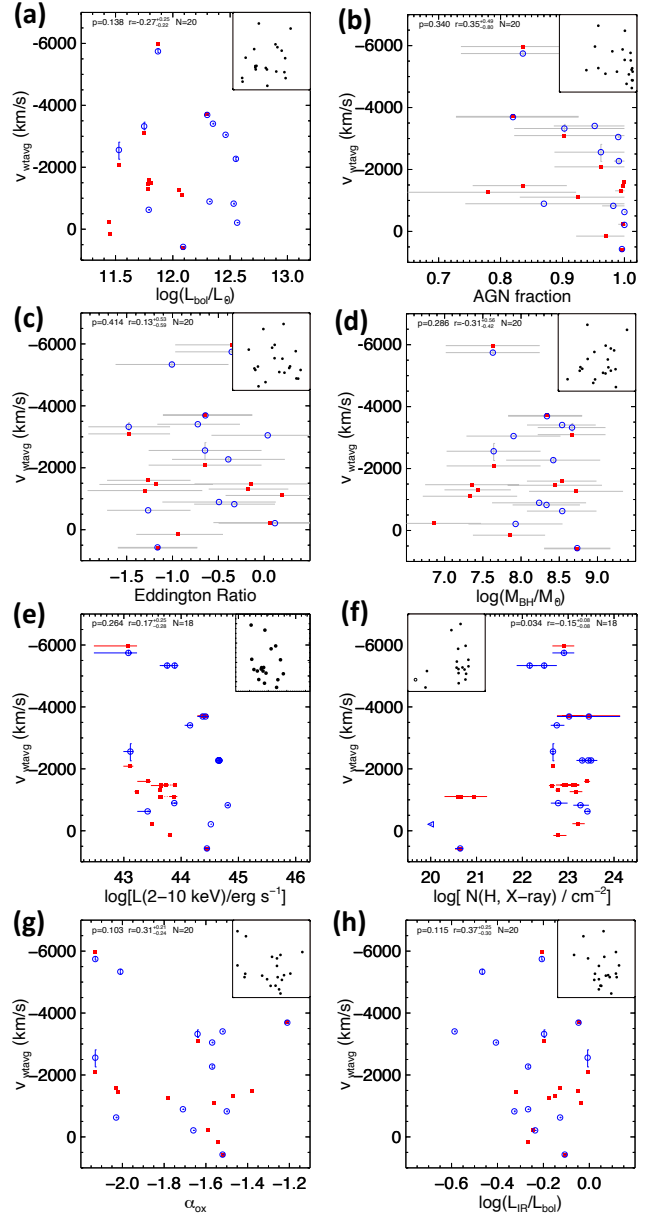


**Figure 9.** Same as Fig. 7 but the weighted average velocities.

The blueshifted N V and O VI absorption features reported in Section 6 may have several origins: quasar-driven outflows, starburst-driven winds, tidal debris from the galaxy mergers, and intervening CGM. Here we do not consider contamination of the quasar spectra by young stars since none of them show the obvious spectral signatures of young stars (e.g., narrow and shallow N V or O VI absorption troughs accompanied by redshifted emission). This is only an issue among starburst-ULIRGs (e.g. Martin et al. 2015).

Telltale signs that the detected lines are formed in a quasar-driven outflow include (1) line profiles that are

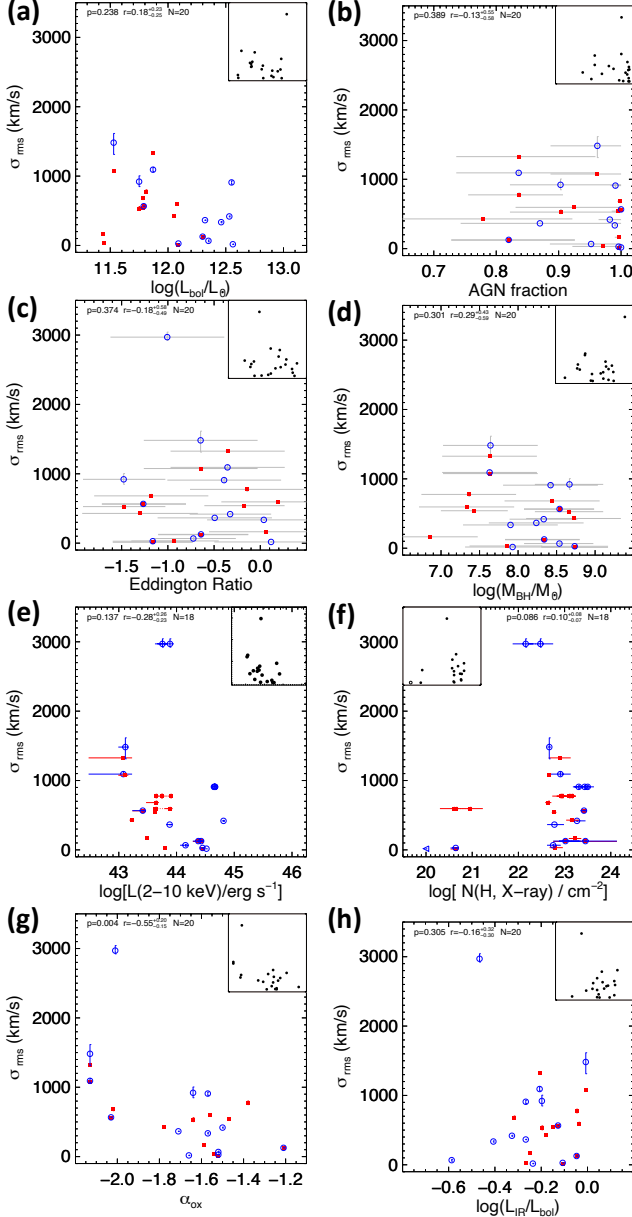


**Figure 10.** Same as Fig. 7 but for the weighted velocity dispersions.

blueshifted, broad, and smooth compared to the thermal line widths ( $\lesssim 10 - 20 \text{ km s}^{-1}$  for highly ionized  $\text{N}^{4+}$ ,  $\text{P}^{4+}$ , and  $\text{O}^{5+}$  ions at  $T \simeq 10^{4.5-5.5} \text{ K}$ ), (2) line ratios within the multiplets  $\text{N V } \lambda 1238/\lambda 1243$ ,  $\text{O VI } \lambda 1032/\lambda 1038$ , and  $\text{P V } \lambda 1117/\lambda 1128$  that imply partial covering of the quasar emission source, and (3) and large column densities in these high-ionization ions (Hamann et al. 1997b,a; Tripp et al. 2008; Hamann et al. 2019b).  $\text{N V}$  is typically very weak or absent in intervening systems (Werk et al. 2016). High  $\text{N V}/\text{H I}$  and  $\text{O VI}/\text{H I}$  are also much higher in associated absorbers than in intervening systems (e.g., Tripp et al. 2008).

Among the 20 quasars with  $\text{N V}$  or  $\text{O VI}$  absorption systems suggestive of outflows, 17 objects have absorption line profiles that meet the first of the above criteria (the only exceptions are PG 0804+761, PG 0844+349, and PG 2233+134). Many of the quasars with blueshifted  $\text{N V}$  or  $\text{O VI}$  absorption lines show  $\text{N V } \lambda 1238/\lambda 1243$  and/or  $\text{O VI } \lambda 1032/\lambda 1038$  line ratios that also meet criteria #2 and #3 (Fig. 6). Mrk 231 does not formally meet these criteria (since it has no  $\text{N V}$  absorption line and  $\text{O VI}$  falls outside of the spectral range of the data), but it shows all of the characteristics of a FeLoBAL at visible and NUV wavelengths (and its  $\text{Ly}\alpha$  line emission is highly blueshifted; Veilleux et al. 2013b, 2016, and references therein), so we include it here among those with quasar-driven outflows. So, overall, at least 18 quasars in our sample have absorption features suggestive of quasar-driven outflows.

In 15 of the 20 absorber detections, the velocity widths,  $\text{FWHM}_{\text{rms}} \equiv 2.355 \sigma_{\text{rms}}$ , are below the minimum of  $2000 \text{ km s}^{-1}$  generally used for BALs (Weymann et al. 1981, 1991; Hamann & Sabra 2004; Gibson et al. 2009a,b), so they fall in the category of mini-BALs ( $500 < \text{FWHM}_{\text{rms}} < 2000 \text{ km s}^{-1}$ ) or NALs ( $\text{FWHM}_{\text{rms}} < 500 \text{ km s}^{-1}$ ). Moreover, in many cases, the profiles are highly structured rather than smooth, and thus do not meet the “BAL-nicity” criterion to be true BALs.

The weak and narrow redshifted absorption features in PG 0804+761 and PG 0844+349 are good candidates for infalling tidal debris.

## 7.2. Location and Structure of the Mini-BALs

### 7.2.1. Depths of the Absorption Profiles

The depths of the mini-BALs may be used to put constraints on the location of the outflowing absorbers. The source of the FUV continuum in these quasars is presumed to be the accretion disk on scale of  $\sim \text{few} \times 10^{15} \text{ cm}$  ( $\lesssim 0.01 \text{ pc}$ ), where we used equation (6) in Hamann et al. (2019a) assuming an Eddington ratio  $\eta_{\text{Edd}} = 0.1$ . But it is clear from the spectra that in many cases (e.g., PG 1001+054, 1004+130, 1126–041, 1309+355, 1351+640, 1411+442, 2214+139) the mini-BALs absorb not only the FUV continuum emission but also a significant fraction of the  $\text{Ly}\alpha$ ,  $\text{N V}$ , and  $\text{O VI}$  line emission produced in the BELR. The gas producing the mini-BALs must therefore be located outside of the BELR on scales larger than

$$r_{\text{BELR}} = 0.1 \left( \frac{L_{\text{AGN}}}{10^{46} \text{ erg s}^{-1}} \right)^{1/2} \text{ pc} \quad (5)$$

(e.g. Kaspi et al. 2005, 2007; Bentz et al. 2013). The radius of the outer boundary of the BELR,  $r_{\text{out}}$ , is likely set by dust sublimation (Netzer & Laor 1993; Baskin &

Laor 2018). For gas densities of  $10^5 - 10^{10} \text{ cm}^{-3}$ , Baskin & Laor (2018) derive

$$r_{\text{out}} \simeq r_{\text{subl}} \simeq (3 - 6)r_{\text{BELR}} \quad (6)$$

$$= (0.3 - 0.6) \left( \frac{L_{\text{AGN}}}{10^{46} \text{ erg s}^{-1}} \right)^{1/2} \text{ pc}, \quad (7)$$

where graphite grains of size  $\sim 0.05 \mu\text{m}$  is assumed (Fig. 5 in Baskin & Laor 2018). Note that these values are smaller than those in Barvainis (1987) and Veilleux et al. (2020), which are based on silicate grains and lower gas densities (thus lower evaporation temperatures).

More can be said about the structure of the absorbing gas from the fact that the N V and O VI absorption features are optically thick ( $\tau \gtrsim 1 - 5$ ; Fig. 6) but are not completely dark. The covering factors derived from the multi-component fits to the N V and O VI mini-BALs range from 0.1 to 1, a direct indication that the absorbing material is compact and spatially inhomogeneous. The often structured velocity profiles of the N V and O VI mini-BALs (N V in PG 1411+442 is arguably the only exception) also suggest a high level of kinematic sub-structures in the outflows, different from the smooth BALs observed in high-luminosity quasars. These properties of the mini-BALs may indicate one of two things: (1) Our line of sight is not aligned along the direction of the outflowing stream of gas as in the case for the BALs (e.g. Murray et al. 1995; Elvis 2000; Ganguly et al. 2001), but instead intercepts only a small fraction of this stream and results in a covering factor of the background emission that is highly dependent on the inhomogeneity of the outflowing gas. (2) Another equally plausible explanation is that (structured) mini-BALs form in more sparse outflows or (in the unified outflow model discussed for high- $z$  quasars) in more sparse outflow regions, e.g., at higher latitudes above the disk.

### 7.2.2. Variability of the Absorption Profiles

Additional constraints on the location and structure of the BALs and mini-BALS in our sample may be obtained from profile variability. There is a vast literature on this topic (e.g., Gibson et al. 2008; Hamann et al. 2008; Gibson et al. 2010; Capellupo et al. 2012; Filiz Ak et al. 2012, 2013; Grier et al. 2015; He et al. 2019; Yi et al. 2019, and references therein). In our sample, four of the mini-BALs (PG 1001+054, PG 1126-041, PG 1411+442, and PG 2214+139) have been observed at two different epochs or more, and can therefore be searched for mini-BAL profile variations. The emergence of a dense [ $\log n_{\text{H}}(\text{cm}^{-3}) \gtrsim 7$ ] new outflow absorption-line system in PG 1411+442 was reported in Hamann et al. (2019b) and the detailed inference of a distance  $\lesssim 0.4 \text{ pc}$  from the quasar is not repeated here.

We present the archival COS spectra for the other three objects in Figure 11, normalized to the same FUV continuum level to emphasize absorption profile variations.

In PG 1001+054 (Fig. 11a), the dramatic (72%) decrease in the FUV continuum emission from June 2014 to March 2019 is accompanied by a strengthening of the broad Ly $\alpha$ , N V, and O VI emission lines in terms of equivalent widths but no obvious change in the mini-BAL profiles. In PG 1126-041 (Fig. 11b), the more modest (20%) decrease of the continuum emission from April 2012 to June 2014 are not accompanied by any obvious variations in the equivalent widths of any of the broad emission and absorption lines except for the most blueshifted N V absorption features below  $-3000 \text{ km s}^{-1}$  which show variations on timescales perhaps as short as 12 days. The broad emission and absorption lines in PG 2214+139 (Fig. 11c) show no variations between November 2011 and September 2021 despite a 26% increase in the strength of the FUV continuum emission.

The fast 12-day variability of the high-velocity N V mini-BAL in PG 1126-041 may be interpreted in two different ways. One possibility is that transverse motions of the outflowing clouds across our line of sight to the continuum source and BELR are responsible for these changes (as in PG 1411+442; Hamann et al. 2019b). A variant on this idea is that the changes in profiles are due instead to the dissolution and creation of the absorbing clouds/clumps in the outflow as they transit in front of the continuum source. In the other scenario, changes in the ionization structure of the absorbing clouds due to changes in the incident quasar flux cause the absorbing N V and O VI columns to vary and reproduce the observations. If this is the case, the variability timescale sets a constraint on the ionization or recombination timescale, which depends solely on the incident ionizing continuum and gas density ( $\sim 10^5 \text{ yrs}/n_{\text{H}}$ , where  $n_{\text{H}}$  is the number density of the clouds in  $\text{cm}^{-3}$ ; e.g., He et al. 2019).

This last scenario predicts that changes in the FUV continuum of the quasar will produce changes in the mini-BAL. While changes are indeed observed in both the FUV continuum emission and high-velocity N V mini-BAL of PG 1126-041, the amplitudes of these changes are not correlated. From 2012-04-15 to 2014-06-01, the continuum emission strengthened while the N V mini-BAL weakened. From 2014-06-01 to 2014-06-12, both the continuum emission and N V mini-BAL weakened. Finally, from 2014-06-12 to 2014-06-28, the continuum emission remained constant to within 1% but the N V mini-BAL strengthened slightly. This lack of a direct connection between variations in the continuum and the N V mini-BAL seems to disfavor the scenario where

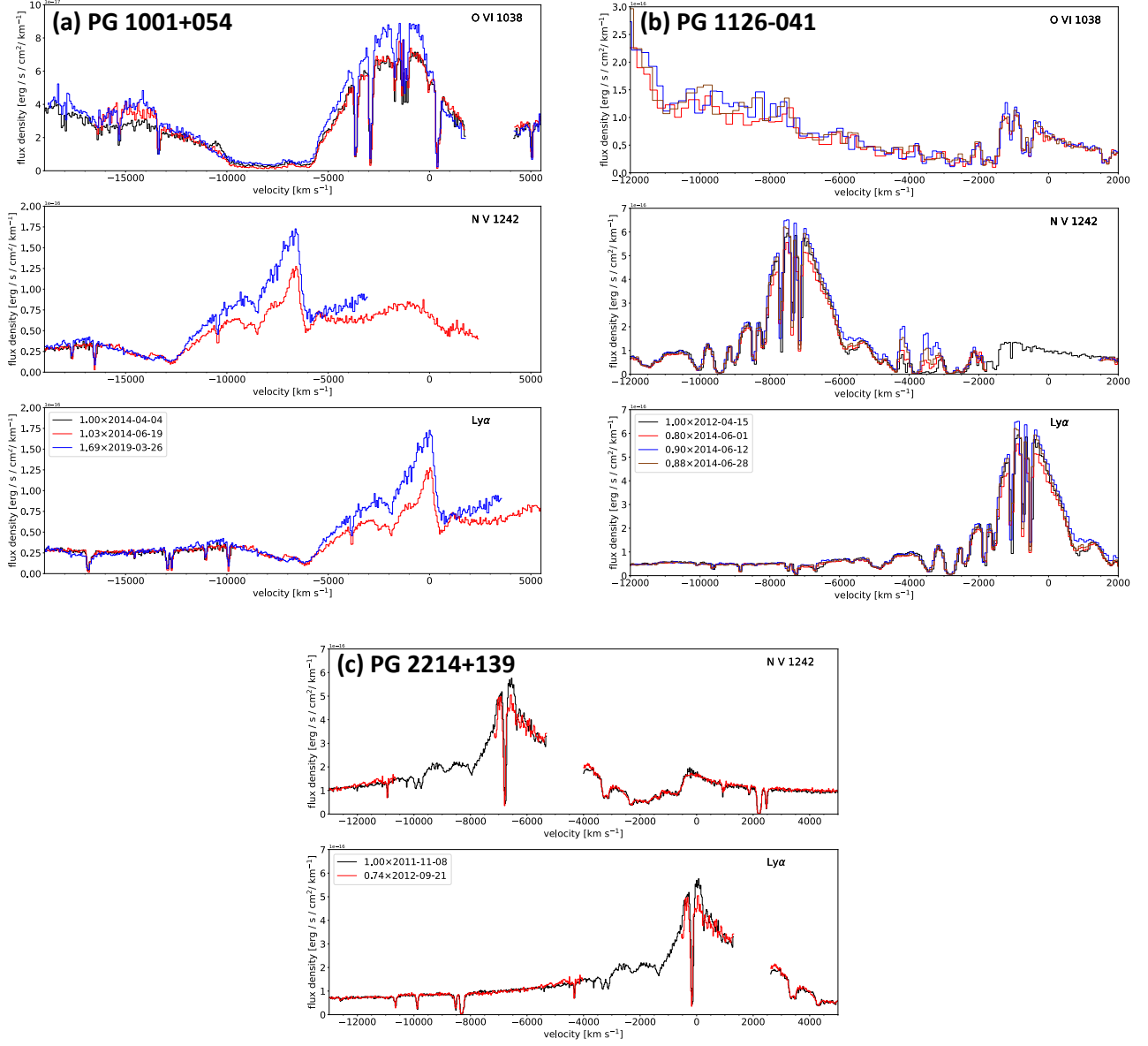


**Figure 11.** Multi-epoch comparisons of the mini-BALs in (a) PG 1001+054, (b) PG 1126–041, and (c) PG 2214+139. All spectra are normalized to match the continuum level blueward of Ly $\alpha$  or redward of N V and O VI. The multiplicative factor is indicated in the caption.

the mini-BAL variations are associated with changes in the ionization structure of the absorbing clouds, unless  $\log n_H(\text{cm}^{-3}) \lesssim 5-6$  in which case  $r \gg r_{\text{out}}$  and time delays associated with the finite recombination timescale could be at play (cf. Hamann et al. 2019b).

While more detailed modeling of the mini-BAL of PG 1126–041 is beyond the scope of the present paper, the fact that the mini-BAL variations are only observed in N V and only at high velocities may be an optical depth effect: the cloud complex that produces the Ly $\alpha$  and O VI mini-BALs and low-velocity N V mini-BAL may be so optically thick to be immune to variations in the ionizing continuum or tangential movement of the

absorbing gas across the continuum source (we return to this topic in Sec. 7.4 below).

### 7.3. Driving Mechanisms of the Mini-BALs

As reviewed in, for instance, Veilleux et al. (2020), the absorbing clouds making up the mini-BALs may be material (1) entrained in a hot, fast-moving fluid, or (2) pushed outward by radiation or cosmic ray pressure, or (3) created *in-situ* from the hot wind material itself. In the first two scenarios, the equation of motion of the outflowing absorbers of mass  $M_{\text{abs}}$  that subtends a solid angle  $\Omega_{\text{abs}}$  is

$$\frac{d}{dt} [M_{\text{abs}}(r) \dot{r}] = \Omega_{\text{abs}} r^2 (P_{\text{th}} + P_{\text{CR}} + P_{\text{jet}})$$

$$+ \left( \frac{\Omega_{abs}}{4\pi} \right) \left( \frac{\tilde{\tau} L_{bol}}{c} \right) - \frac{GM(r)M_{abs}(r)}{r^2}, \quad (8)$$

where  $M(r)$  is the galaxy mass enclosed within a radius  $r$  and  $\tilde{\tau}$  is a volume- and frequency-integrated optical depth that takes into account both single- and multiple-scattering processes in cases of highly optically thick clouds (Hopkins et al. 2014, 2020).<sup>2</sup> The terms on the right in Equation 8 are the forces due to the thermal, cosmic ray, and jet ram pressures, the radiation pressure, and gravity, respectively. Magneto-hydrodynamical effects are assumed to be negligible at the distances of these absorbing clouds. The quasars in our sample do not have powerful radio jets so the jet ram pressure term can safely be neglected. Similarly, the relatively modest radio luminosities of the mini-BAL quasars relative to their optical and bolometric luminosities (Column 6 in Table 1) suggest that cosmic-ray electrons do not play an important dynamical role in accelerating the BAL clouds. Indeed the fraction of BAL quasars seems to vary inversely with the radio loudness parameter,  $R$  (Column 5 in Table 1; e.g., Becker et al. 2001; Shankar et al. 2008). Below, we consider the remaining thermal and radiation pressure terms separately. In reality, these pressure forces may act together to drive the mini-BAL outflows (see Sec. 7.4 for a closer look at the mini-BAL PG 1126–041 in this context).

### 7.3.1. Thermal Wind and Blast Wave

For many years, ram-pressure acceleration of pre-existing clouds has been considered a serious contender to explain BALs in quasars given the need for a much hotter, rarefied medium to confine the clouds as they are being accelerated (e.g. Weymann et al. 1985). However, it is notoriously difficult to accelerate dense gas clouds from rest up to the typical (mini-)BAL velocities by a warm, fast thermal wind without destroying them in the process through Rayleigh-Taylor fragmentation and shear-driven Kelvin-Helmholtz instabilities (e.g. Cooper et al. 2009; Scannapieco & Brüggén 2015; Schneider & Robertson 2015, 2017). Radiative cooling and magnetic fields may act to slow down cloud disruption (Marcolini et al. 2005; Cooper et al. 2009; Banda-Barragán et al. 2016, 2018, 2020; Grønnow et al. 2018). Radiative cooling of the warm mixed gas can not only prevent disruption, but it may cause the cloud to grow in mass (e.g., Gronke & Oh 2018, 2020; Girichidis et al. 2021), al-

though there are caveats (Schneider et al. 2020). An alternative scenario is that the BAL and mini-BAL clouds are created *in-situ* via thermal instabilities and condensation from the hot gas with a cooling time shorter than its dynamical time (Efstathiou 2000; Silich et al. 2003). This is the idea behind the “blast wave” simulations of Richings & Faucher-Giguère (2018a,b); see also Weymann et al. (1985); Zubovas & King (2012, 2014); Faucher-Giguère & Quataert (2012); Nims et al. (2015).

In these simulations, a fast (presumably X-ray emitting) AGN wind with outward radial velocity of 30,000  $\text{km s}^{-1}$  is injected in the central 1 pc and collides violently with the host ISM. The resulting shocked wind material reaches a very high temperature ( $\sim 10^{10}$  K; Nims et al. 2015) that does not efficiently cool, but instead propagates outward as an adiabatic (energy-driven) hot bubble. This expanding bubble sweeps up gas and drives an outer shock into the host ISM raising its temperature to a few  $\times 10^7$  K (Nims et al. 2015). Radiative cooling of the shocked ISM eventually becomes important and the outflowing material reforms as cool neutral and molecular gas, but by that time, the outflowing material has acquired a significant fraction of the initial kinetic energy of the hot wind. These simulations predict that the cooling radius, i.e. the radius at which the gas cools to  $10^4$  K, increases from 100 pc to 1 kpc for AGN with luminosities from  $10^{44}$  to  $10^{47}$   $\text{erg s}^{-1}$ , respectively (Fig. 7 of Richings & Faucher-Giguère 2018b). This cooling radius is also the expected location of the gas clouds producing the N V and O VI mini-BALs, as the cooling gas rapidly transitions from  $\sim 10^7$  K to  $\sim 10^4$  K. This large radius is well outside the lower limit on the distance of the mini-BAL from the quasars derived above so it is not inconsistent with our data. However, one should note that the inner X-ray wind in quasars is presumed to be much smaller in reality than the value of 1 pc assumed in the simulations so the cooling radius may have to be scaled down accordingly. Moreover, these models do not address how the BELRs would be restored after the passage of the blast wave. Finally, the detailed analysis of the BAL in PG 1411+442 firmly rule out (at least in that case) absorption at these large distances.

### 7.3.2. Radiative Acceleration

Although ram-pressure acceleration has been a serious contender, overall the favored explanation for the large velocities of the BALs and mini-BALs is that the gas absorbers have been accelerated by the radiation pressure forces associated with the intense radiation field that is emanating from the quasars (e.g., Arav et al. 1994; Giustini & Proga 2019). Strong support for this sce-

<sup>2</sup> More explicitly,  $\tilde{\tau} \equiv (1 - e^{-\tau_{\text{single}}})(1 + \tau_{\text{eff,IR}})$ . The value of  $\tilde{\tau}$  therefore ranges from  $\sim \tau_{\text{single}} = \tau_{\text{UV/optical}} \ll 1$  in the optically thin case to  $\sim (1 + \tau_{\text{eff,IR}}) \gtrsim 1$  in the infrared optically-thick limit (the effective infrared optical depth,  $\tau_{\text{eff,IR}}$ , is also sometimes called the “boost factor”; Veilleux et al. (2020)).

nario comes from the observed trends for the maximum velocity of the absorption to increase on average with increasing optical, UV, or bolometric luminosity and the Eddington ratio (e.g., Perry & O’Dell 1978; Brandt et al. 2000; Laor & Brandt 2002; Ganguly et al. 2007; Ganguly & Brotherton 2008; Gibson et al. 2009b; Zhang et al. 2014). Note, however, that the overall correlations noted in these studies are often quite modest and sometimes only visible when considering the upper envelope of the velocity distribution and only when the sample of AGN span 2-3 orders of magnitude in luminosity (sometimes combining NALs, mini-BALs, and BALs together). While more recent studies (e.g., Rankine et al. 2020) have confirmed and indeed strengthened the existence of some of these correlations, all of the cited results relate to the C IV absorption, rather than the N V and O VI features. The statistics on N V and particularly O VI absorbers are much poorer.

*Far Ultraviolet Spectroscopic Explorer (FUSE)* observations of Seyfert galaxies of relatively low luminosities ( $10^{38} - 10^{42}$  erg s $^{-1}$ ) show either no or very weak trends of increasing maximum velocities with increasing luminosities and no trend at all with the Eddington ratio (Kriss 2004a,b; Dunn et al. 2008). O VI and N V BALs in high-redshift, high-luminosity quasars (Baskin et al. 2013; Hamann et al. 2019a) have maximum velocities that correlate with their C IV counterparts, but the range in AGN luminosity of their sample is too small to test the luminosity dependence of the maximum velocities. More fundamentally, there is also a trend between line widths and optical depth. The most extreme example of this trend is P V, which coexists with C IV having the same ionization requirements, but is always weaker and narrower than C IV (Hamann et al. 2019a). The reason is that P V traces only the highest column density regions with smaller covering fractions, while C IV can have significant absorption in more diffuse gas occupying a larger volume. This evidence for optical depth-dependent covering factors is a signature of inhomogeneous partial covering.

Overall, given the complex results from these previous studies, it is perhaps not surprising to find no significant correlations in our sample of QUEST quasars between (maximum) outflow velocities and the AGN luminosities (Sec. 6.4). Theoretically, the noise in the trends between the outflow kinematics and AGN luminosity is *expected* in the radiative acceleration scenario given projection effects that reduce the measured outflow velocities and variance in both the (minimum) launching radius (e.g. Laor & Brandt 2002) and efficiency of radiative acceleration associated with the complex micro-physics of the photon interaction with the clouds - this complexity is

hidden in the quantity  $\tilde{\tau}$  in equation 8. A similar trend of increasing variance in the maximum velocity with increasing AGN luminosity is observed in the other cooler gas phases of AGN-driven outflows (e.g., Veilleux et al. 2020; Fluetsch et al. 2020).

Additional evidence that radiation pressure plays an important role in accelerating the absorbers in quasars comes from the significant dependence of the incidence rate, equivalent width, and weighted outflow velocity dispersion of the blueshifted absorbers on the X-ray properties of the quasars. This effect has been reported in numerous studies of nearby and distant AGN, based largely on C IV and Si IV (e.g., Laor & Brandt 2002; Gibson et al. 2009b), and is also clearly present in our sample of quasars based on N V and O VI (Sec. 6.1, 6.3, and 6.4). More specifically, we find that mini-BALs and BALs are broader, stronger, and more common among X-ray faint quasars with steep optical-to-X-ray slopes  $\alpha_{\text{OX}} \lesssim -1.7$  and hydrogen column densities  $N_{\text{H}}$  in excess of  $\sim 10^{22}$  cm $^{-2}$  (Sec. 6). This result is expected in the context of radiative acceleration since the combined radiative force (“force multiplier”; Arav & Li 1994) is greatly reduced when the gas is over-ionized by the hard far-UV/X-rays, becoming too transparent to be radiatively accelerated. This over-ionized “failed-wind” material may act as a radiative shield to produce the spectral softening needed for efficient radiative acceleration of the outflow material downstream (Murray et al. 1995; Proga & Kallman 2004; Proga 2007; Sim et al. 2010). However, the strong near-UV absorption lines near systemic velocity expected in this scenario are not observed (Hamann et al. 2013). Alternatively, the spectrum emerging from the accretion disk may be intrinsically softer/fainter in the hard far-UV/X-rays than commonly assumed (e.g. Laor & Davis 2014). Weak-lined “wind-dominated” quasars, such as Mrk 231, PHL 1811 and its analogs, which are intrinsically faint and unabsorbed in the X-rays, may be naturally explained in this fashion (Richards et al. 2011; Wu et al. 2011; Luo et al. 2015; Veilleux et al. 2016). While a connection should exist between the X-ray warm absorbers and the UV absorption-line outflows, a direct one-to-one kinematic correspondence between the two classes of absorbers is often not seen because the gas in the warm absorbers is too highly ionized to produce measurable lines in the UV spectra (Kaspi et al. 2000, 2001; Gabel et al. 2003; Kraemer et al. 2001; Krongold et al. 2003; Arav et al. 2015; Laha et al. 2021, and references therein). We return to this point in Section 7.4 when discussing the mini-BAL in PG 1126–041 (the case of PG 1211+143 is briefly discussed in Appendix A).

Another observational characteristic of outflows that favors radiative acceleration is the phenomenon of line-locking observed in perhaps as many as  $\sim 2/3$  of all NAL and (mini-)BAL outflows (e.g., Hamann et al. 2011; Bowler et al. 2014; Lu & Lin 2018; Mas-Ribas & Mauland 2019, and references therein). This is observed in outflows where multiple absorbers are present but are separated by the exact same velocity separation as the doublet of C IV ( $499 \text{ km s}^{-1}$ ), N V ( $962 \text{ km s}^{-1}$ ), or O VI ( $1650 \text{ km s}^{-1}$ ). Previous studies have shown that the probability of a line-locking signature accidentally occurring over a relatively small redshift path is negligible (e.g., Foltz et al. 1987; Srianand 2000; Srianand et al. 2002; Ganguly et al. 2003; Benn et al. 2005). Radiative acceleration is a natural explanation for line-locking (e.g., Mushotzky et al. 1972; Scargle 1973; Braun & Milgrom 1989).

The best case for line-locking in our data is that of PG 1351+640, where two deep absorption troughs are detected in Ly $\alpha$ , extending over  $-[2200, 1500] \text{ km s}^{-1}$  and  $-[1400, 600] \text{ km s}^{-1}$ , roughly separated by the velocity split of the N V doublet lines ( $\Delta v \approx 900 - 1000 \text{ km s}^{-1} \approx \Delta v_{\text{NV}}$ ; Fig. 12). This results in a N V mini-BAL that looks like a “triplet” in this object. Another case of line-locking may be present in PG 1126–041, where some of the deepest Ly $\alpha$  troughs are separated by  $\Delta v \approx 900 - 1000 \text{ km s}^{-1} \approx \Delta v_{\text{NV}}$  (Fig. 3).

Note, finally, that radiation pressure on dust grains has also been invoked as an important contributor to the radiative acceleration given that (mini-)BAL QSOs, particularly LoBALs and FeLoBALs, have more reddened UV spectra than non-BAL QSOs (e.g., Allen et al. 2011; Hamann et al. 2019a, and references therein). This result has been interpreted to mean that BAL and mini-BAL clouds have large columns of ionized + neutral gas ( $\log N_{\text{H}}(\text{cm}^{-2}) \gtrsim 23$ ) and enough dust to provide extinction equivalent to at least  $A_V \sim 1\text{-}2 \text{ mag}$ . in some cases (this is discussed in Sec. 7.4 in the context of PG 1126–041, but see also the results on Mrk 231 and PG 1411+442; Veilleux et al. 2016; Hamann et al. 2019b, respectively). Under these circumstances, the (mini-)BAL clouds may be subject to larger radiative forces than dustless clouds since the dust cross section, and thus  $\tilde{\tau}$  in equation 8, in the UV optical is  $> 1\text{-}2$  orders of magnitude than the Thompson scattering cross section of electrons. Unfortunately, we do not have a reliable reddening indicator of the FUV continuum emission in our quasars, so we cannot directly compare our data with those of BAL and non-BAL QSOs. On the other hand, radiation that will be absorbed by the dust in the broad absorption line regions (BALRs) will be re-emitted in the infrared so our measurements of the

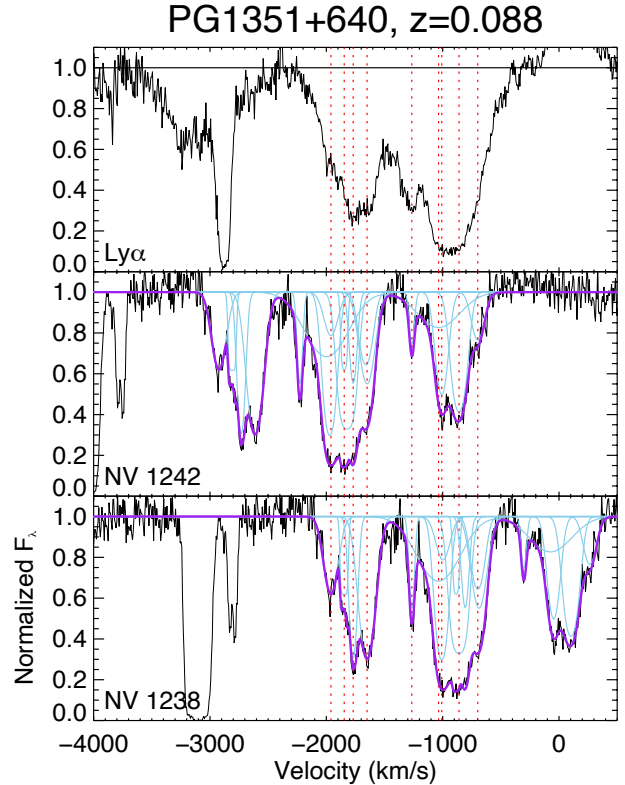


**Figure 12.** Line-locking in PG 1351+640. The two deep Ly $\alpha$  absorption troughs are separated by the velocity split of the N V doublet lines, resulting in a N V complex that looks like a “triplet”.

infrared excess in our quasars may serve as a surrogate for the amount of dust in the BALRs. The lack of obvious correlation between BAL properties in our quasar sample and the mid-, far-, and total ( $1 - 1000 \mu\text{m}$ ) infrared excesses (e.g., Figs. 7 and 10) indicates one of two things: (1) radiative acceleration on dust is not important in the BALRs of these objects or (2) the various infrared excesses are dominated by dust emission from outside of the BALR, e.g. dust in the host galaxy itself.

#### 7.4. *P V Mini-BAL in PG 1126–041 and Other Quasars*

In this last section, we take a closer look at the mini-BAL system in PG 1126–041. A mini-BAL extending from  $-1000$  to  $-5000 \text{ km s}^{-1}$  was first reported in the N V, C IV, and S IV absorption lines of this object by Wang & Wang (1999); Wang et al. (1999), based on the analysis of old low-resolution spectra obtained with IUE and the Goddard High-Resolution Spectrograph (GHRS) on *HST*. Variable and much faster ( $\sim 16,500 \text{ km s}^{-1}$ ) X-ray absorption has also been detected in this object (Wang & Wang 1999; Wang et al. 1999; Gius-



tini et al. 2011). Interestingly, this object is among the least luminous AGN ( $\log L_{\text{BOL}}/L_{\odot} = 11.52$ ) in our sample, intermediate between quasars and typical Seyfert 1 galaxies. Mini-BALs with outflow velocities of up to  $\sim 5000 \text{ km s}^{-1}$  and widths ( $\text{FWHM}_{\text{rms}} \equiv 2.355 \sigma_{\text{rms}}$ )  $> 1000 \text{ km s}^{-1}$  are relatively rare in such low-luminosity systems (e.g., Kriss 2004a,b; Dunn et al. 2008; Crenshaw & Kraemer 2012). On the other hand, PG 1126–041 is also the object in our sample with the steepest X-ray to optical index ( $\alpha_{\text{OX}} = -2.13$ , a virtual tie with PG 1001+054, which also harbors a mini-BAL) and is among those with the largest infrared excess (Table 1), reinforcing the view expressed in Section 7.3.2 that X-ray absorbed or intrinsically weak quasars are more likely to host BALs and mini-BALs.

Apart from the line-locking signatures found in the N V mini-BAL of this object, which we argued in Sec. 7.3 favors radiative driving, the most remarkable aspect of this mini-BAL is the detection of a narrow P V  $\lambda\lambda 1117, 1128$  cloud at a velocity of  $-2200 \text{ km s}^{-1}$  (Fig. 3). Large ionized-gas column densities are needed to produce this feature given the low abundance of phosphorus relative to hydrogen ( $\log(\text{P}/\text{H})_{\odot} = -5.54$ ; Lodders 2003). The multi-component fit of each line in the P V doublet requires two components with nearly identical median velocities ( $-2196$  and  $-2203 \text{ km s}^{-1}$ ) but different velocity dispersions ( $24$  and  $74 \text{ km s}^{-1}$ ), covering factors ( $0.37$  and  $0.10$ , respectively), and optical depths ( $0.7$  and  $2.6$ , respectively). The total equivalent width of this doublet is  $0.3 \text{ \AA}$ .

Taken at face value, the results from the fits suggest that the P V lines are only moderately optically thick and therefore more reliable indicators of the total ionized column densities of this cloud than the highly saturated N V and O VI features. This is supported by the  $\sim 2:1$  intensity ratio of the P V lines. An optical depth of order unity in P V  $\lambda 1128$  implies an ionized hydrogen column density  $\log N_{\text{H}}(\text{cm}^{-2}) \approx 22.3$ , assuming a solar P/H abundance ratio and ionization corrections based on detailed photoionization calculations for typical BALs and mini-BALs (ionization parameters  $\log U \gtrsim -0.5$ ; Hamann 1998; Leighly et al. 2011; Borguet et al. 2012, 2013; Baskin et al. 2014; Capellupo et al. 2017; Moravec et al. 2017; Hamann et al. 2019a, and references therein). This column density is remarkably consistent with the expectations from radiation pressure confined cloud models (Baskin et al. 2014).

This value of the total column density may be used to estimate the minimum kinematic energy of this outflowing cloud using (eq. 2 from Hamann et al. 2019a)

$$E_{\text{kin}} = 1.5 \times 10^{52} \left( \frac{Q}{0.15} \right) \left( \frac{N_{\text{H}}}{2 \times 10^{22} \text{ cm}^{-2}} \right) \left( \frac{r}{1 \text{ pc}} \right)^2$$

$$\times \left( \frac{v}{2200 \text{ km s}^{-1}} \right)^2 \text{ ergs}, \quad (9)$$

where  $Q$  is an approximate global outflow covering factor based on the incidence of mini-BALs in the SDSS quasars (Trump et al. 2006; Knigge et al. 2008; Gibson et al. 2009b; Allen et al. 2011) and  $r = 1 \text{ pc}$  is a placeholder radial distance that we adopt for illustration purposes (it may underestimate the actual distance of the absorbers from the source; see Sec. 7.2 and Arav et al. 2020, and references therein). Following Hamann et al. (2019b), we estimate the time-averaged kinetic energy luminosity,  $L_{\text{kin}}$ , by dividing  $E_{\text{kin}}$  by a characteristic flow time,  $r/v \approx 450 \text{ yr}$ . This yields  $L_{\text{kin}} \gtrsim 1 \times 10^{42} \text{ erg s}^{-1}$ . In these units,  $L_{\text{BOL}} = 1.3 \times 10^{45} \text{ erg s}^{-1}$  so  $L_{\text{kin}}/L_{\text{BOL}} \gtrsim 0.001$ . Taken at face value, this ratio is too small to significantly affect the evolution of the galaxy host (e.g.,  $L_{\text{kin}} \gtrsim 0.005 L_{\text{Edd}}$  is needed according to Hopkins & Elvis 2010), unless (1)  $r$  is severely underestimated or (2) the other clouds at lower and higher velocities involved in this mini-BAL contribute significantly to  $L_{\text{kin}}$ . This second possibility seems unlikely given the lack of P V detection in these clouds which suggests column densities  $\log N_{\text{H}}(\text{cm}^{-2}) \lesssim 22$ .

Next, we use the total column density of the P V cloud in PG 1126–041 to estimate the time-averaged momentum outflow rate of this cloud,  $\dot{p} = 2L_{\text{kin}}/v \approx 1 \times 10^{34} \text{ dynes}$ , and compare this value with the radiation pressure,  $L_{\text{BOL}}/c = 4 \times 10^{34} \text{ dynes}$ . Given that  $\dot{p}/(L_{\text{BOL}}/c) \sim 0.2$ , radiation pressure can thus in principle accelerate this cloud, although a contribution from a thermally driven wind as detailed in Section 7.3.1 cannot be formally ruled out.

Finally, we apply Equation 9 and calculate  $L_{\text{kin}}/L_{\text{BOL}}$  for the other mini-BALs in our sample with solid and tentative P V detections. For PG 1411+442, the only other mini-BAL in the sample with a definite P V detection, we get  $L_{\text{kin}}/L_{\text{BOL}} \gtrsim 0.01$  and  $\dot{p}/(L_{\text{BOL}}/c) \sim 1$ , for an outflow velocity of  $-1800 \text{ km s}^{-1}$  (Table 3), a total column density  $\log N_{\text{H}}(\text{cm}^{-2}) \gtrsim 23.4$ , and a BELR-like distance  $\lesssim 0.4 \text{ pc}$  from the central light source derived by Hamann et al. (2019b) using several absorption lines and detailed photoionization simulations. This BAL may thus be sufficient to impact the host galaxy evolution. P V is also tentatively detected in PG 1001+054 and PG 1004+130 at velocities of  $\sim [-4000, -6,000] \text{ km s}^{-1}$  (Fig. 13). In both cases, the equivalent widths of P V 1117 and 1128 are very similar, implying saturation and  $\log N_{\text{H}}(\text{cm}^{-2}) \gtrsim 22.3$ . These numbers yield outflows with kinetic-to-bolometric luminosity ratios that are higher than that of PG 1126–041 but lower than that of PG 1411+442, and thus marginally sufficient to impact the host galaxy evolution. Overall, the mini-BALs in the QUEST quasars are less powerful than the

P V BALs detected in  $z_e \gtrsim 1.6$  SDSS quasars (Moravec et al. 2017) but perhaps more common (4/33  $\sim 10\%$ ) than at high luminosities/redshifts (detection rate of only 3–6% among the  $z_e \gtrsim 2.6$  BAL quasars in the SDSS-III BOSS quasar catalog Capellupo et al. 2017).

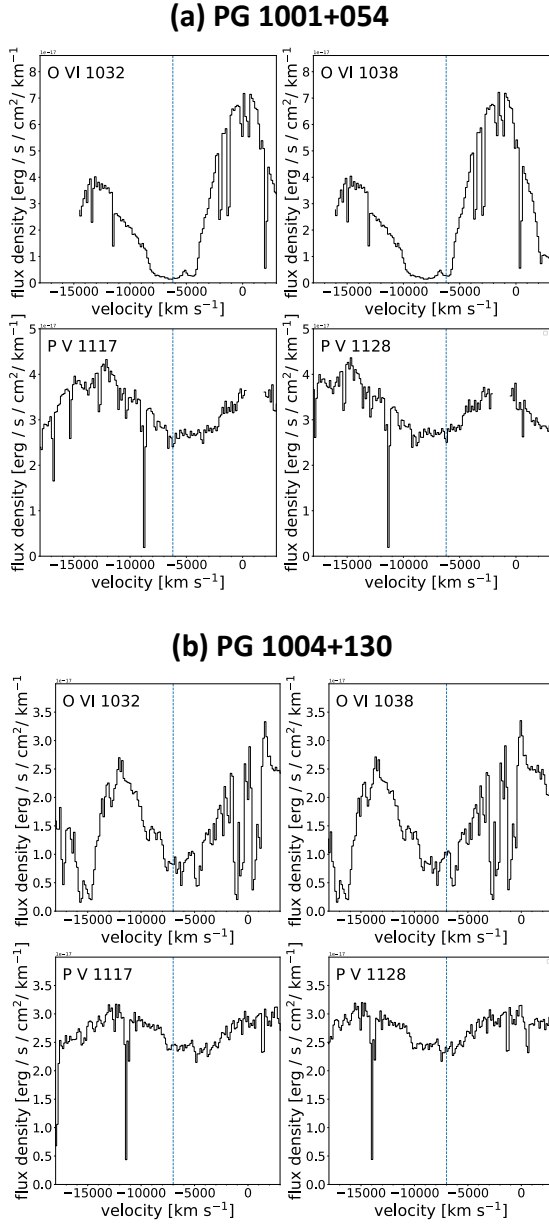


**Figure 13.** Tentative detection of P V in (a) PG 1001+054 and (b) PG 1004+130. The spectra have been heavily binned to emphasize the broad but shallow features. The deep and narrow absorption lines in the velocity range  $-[8,000, 14,000]$   $\text{km s}^{-1}$  in the P V 1117, 1128 panels of both PG 1001+054 and PG 1004+130 are due to intervening MW ISM (Si II 1259, 1260 + Fe II 1260 and C II 1334 + C II\* 1335, respectively).

## 8. SUMMARY

As part I of a *HST* FUV spectroscopic study of the QUEST (Quasar/ULIRG Evolutionary Study) sample of local quasars and ULIRGs, we have conducted a uniform analysis of the COS spectra of 33  $z \lesssim 0.3$  Palomar-Green quasars. The main conclusions from our analysis are the following:

1. Highly ionized outflows traced by blueshifted N V  $\lambda\lambda 1238, 1243$  and O VI  $\lambda\lambda 1032, 1038$  absorption lines with equivalent widths larger than  $\sim 20$  mÅ are present in about 60% of the QUEST quasars. This detection rate is similar to that of warm-ionized outflows traced by blueshifted C IV  $\lambda\lambda 1548, 1550$  absorption lines in local Seyfert galaxies and more distant, higher luminosity quasars.
2. The N V and O VI features in the QUEST quasars span a broad range of properties, both in terms of equivalent widths (from 20 mÅ to 25 Å) and kinematics (outflow velocities from a few  $\times 100$   $\text{km s}^{-1}$  up to  $\sim 10,000$   $\text{km s}^{-1}$ ).
3. The rate of incidence and equivalent widths of the highly ionized outflows are higher among X-ray weak sources with X-ray to optical spectral indices  $\alpha_{\text{OX}} \lesssim -1.7$  and X-ray column densities  $\log N_{\text{H}}(\text{cm}^{-2}) \gtrsim 22$ . The weighted outflow velocity dispersions are highest in the X-ray weakest sources with X-ray to optical spectral indices  $\alpha_{\text{OX}} \lesssim -2$ . These results are qualitatively similar to AGN-driven warm ionized outflows traced by the C IV  $\lambda\lambda 1548, 1550$  absorption lines. These results favor radiative acceleration of the absorbers, where the X-rays are either absorbed or intrinsically weak in the wind-dominated systems. Line-locking is detected in the Ly $\alpha$  absorption throughs of one or two objects, providing additional evidence that radiation pressure plays an important role in accelerating these absorbers.
4. There is no significant trend between the weighted average velocity of the highly ionized outflows and the properties of the quasars and host galaxies. This negative result is likely due in part to the fact that the range of properties of the QUEST quasar sample is narrow in comparison to those of other studies.
5. Blueshifted P V broad absorption lines are clearly detected in PG 1126–041 and PG 1411+442 (previously reported in Hamann et al. 2019b), and also

possibly in PG 1001+054 and PG 1004+130. Using the results from the analysis of Hamann et al. (2019b), these features imply column densities of  $\sim 10^{22.3} \text{ cm}^{-2}$  or larger and time-averaged outflow kinetic power to bolometric luminosity ratios of  $\gtrsim 0.1\%$  if a conservatively small radial distance of 1 pc from the P V absorbers is assumed.

Paper II of this series (Liu et al. 2021, in prep.) will present the results from our analysis of the COS spectra on the QUEST ULIRGs. These results will be combined with those from the present paper to provide a more complete picture of the gaseous environments of quasars and ULIRGs as a function of host galaxy properties and age across the merger sequence from ULIRGs to quasars.

#### ACKNOWLEDGMENTS

The authors thank the anonymous referee for suggestions which improved this paper. SV, WL, and TMT acknowledge partial support for this work provided by NASA through grant numbers *HST* GO-1256901A and GO-1256901B, GO-13460.001-A and GO-13460.001-B, and GO-15662.001-A and GO-15662.001-B from the Space Telescope Science Institute, which is operated by AURA, Inc., under NASA contract NAS 5-26555. Based on observations made with the NASA/ESA Hubble Space Telescope, and obtained from the Hubble Legacy Archive, which is a collaboration between the Space Telescope Science Institute (STScI/NASA), the Space Telescope European Coordinating Facility (ST-ECF/ESA) and the Canadian Astronomy Data Centre (CADM/NRC/CSA). The authors also made use of NASA’s Astrophysics Data System Abstract Service and the NASA/IPAC Extragalactic Database (NED), which is operated by the Jet Propulsion Laboratory, California Institute of Technology, under contract with the National Aeronautics and Space Administration.

*Software:* COSQUEST (Rupke 2021a), IFSFIT (Rupke 2014; Rupke & Veilleux 2015; Rupke 2021b), LINMIX\_ERR (Kelly 2007), pymccorrelation (Privon et al. 2020), scipy (Virtanen et al. 2020), DRTOOLS (Rupke 2021c)

## APPENDIX

## A. DETAILED RESULTS FROM THE SPECTRAL ANALYSIS

Figures 14a–14t present the fits to the detected N V, O VI, and P V absorption systems in our sample. The results from these fits are listed in Table 3 in the main body of the paper. Here we summarize the results from our spectral analysis for each object in the sample.

*PG 0007+106.*—There are no associated N V absorbers in this system, although two deep blueshifted and redshifted Ly $\alpha$  absorption features are present at  $|v| < 400 \text{ km s}^{-1}$ .

*PG 0026+129.*—There are no associated N V or O VI absorbers in this object.

*PG 0050+124 (I Zw 1).*—N V and Ly $\alpha$  absorbers are detected at  $-553$ ,  $-1315$ , and  $-1467 \text{ km s}^{-1}$  in this object. Variable warm absorbers at  $-1870$  and  $-2500 \text{ km s}^{-1}$  have been reported by [Silva et al. \(2018\)](#) in *XMM-Newton* RGS spectra obtained in 2015.

*PG 0157+001 (Mrk 1014).*—There are no associated N V or O VI absorbers in this system.

*PG 0804+761.*—This is a rare case for infall where a strong redshifted absorption system at  $+600 \text{ km s}^{-1}$  is observed in Ly $\alpha$ , and a corresponding weaker feature is also detected in N V and O VI. The stronger features in the panel of Figure 14b labeled O VI 1037 are Fe II features from the MW ISM.

*PG 0838+770.*—A weak low- $|v|$  absorption feature is seen in Ly $\alpha$  but not N V or O VI.

*PG 0844+349.*—A strong slightly redshifted double-component absorption feature, likely associated with tidal debris, is present at  $+140 \text{ km s}^{-1}$  and  $+190 \text{ km s}^{-1}$  in both Ly $\alpha$  and N V, but the feature at  $\sim 1288.9 \text{ \AA}$  has no corresponding N V and is presumed to be Ly $\alpha$  from intervening CGM.

*PG 0923+201.*—A single broad absorber is observed at  $-3300 \text{ km s}^{-1}$  in Ly $\alpha$ , Ly $\beta$ , and O VI 1032 and 1038 although the glare of the geocoronal Ly $\alpha$  airglow truncates the blue wing of the O VI 1032 absorption line.

*PG 0953+414.*—Two faint O VI features are detected at  $-140$  and  $-1074 \text{ km s}^{-1}$ . The first feature is also visible in Ly $\alpha$  and Ly $\beta$ , but the more blueshifted feature is not. The strong feature near  $1271 \text{ \AA}$  cannot be fit with O VI and thus is likely Ly $\alpha$  from intervening CGM.

*PG 1001+054.*—The multi-epoch COS spectra shown in Figure 11 are co-added for this analysis given the lack of variability in the absorption line profiles (Sec. 7.2). This is a special case because of the way the broad, high-velocity N V absorption absorbs the Ly $\alpha$  profile and the O VI absorption is deep, nearly dark, and highly saturated. The three methods discussed in Section 5 were attempted to deal with the Ly $\alpha$  + N V blend, and in the end method #3 was used for the final fit: (1) The use of polynomials/splines to fit the blue and red sides of Ly $\alpha$  is problematic because it does not appear to yield a symmetric Ly $\alpha$  line and seems to miss N V absorption that appears in Ly $\alpha$ . (2) A Lorentzian fit to Ly $\alpha$  works reasonably well in that it yields a symmetric line, but the line properties are highly unconstrained (particularly in terms of height) and sensitive to the choice of which continuum regions are fit. (3) After trying the QSO templates from [Vanden Berk et al. \(2001\)](#), [Stevans et al. \(2014\)](#), and [Harris et al. \(2016\)](#), we settled on the last one. We scaled the template using a constant offset, a constant multiplier, and a scaling according to  $\lambda^p$  (arbitrary power  $p$ ) to account for differences between the spectral index and that of the template (following [Harris et al. 2016](#)). We fit only the blue side of Ly $\alpha$  (and the far-red side) as well as some continuum regions in between O VI and Ly $\alpha$ N V that are fairly line-free. This underpredicts the strength of highly-ionized lines, but is the best compromise solution. If the lines are fit as well, the blue side of Ly $\alpha$  is not properly fit. The resulting fit to N V seems to work reasonably well, although the fit results are obviously illustrative in terms of velocity space and certainly do not get the optical depth correct. There seems to be a narrow Ly $\alpha$  near  $-4000 \text{ km s}^{-1}$  that is barely detected in N V, but the fit has difficulties capturing it. The broad, highly saturated, nearly dark O VI is fit over  $-[6000, 4000] \text{ km s}^{-1}$  but not  $-[8000, 6000] \text{ km s}^{-1}$  to account for Ly $\beta$  contamination. Broad blueshifted P V 1117, 1128 at  $\sim -[6000, 4000] \text{ km s}^{-1}$  is also tentatively detected in this object but no attempt is made to fit this faint feature (Fig. 13a).

*PG 1004+130.*—This is another special case (see [Wills et al. 1999](#); [Brandt et al. 2000](#), for some previous analyses). It is difficult to fit the “continuum” shape and O VI profile simultaneously. The present fit is the best available compromise. It is clear that Ly $\beta$  / O VI are interacting with each other so the O VI fit should be taken only as illustrative. There are higher-order Lyman lines in the spectrum that are not considered. The Ly $\gamma$  region is shown but is not considered in the fits to O VI (the many narrow features in the Ly $\gamma$  region are Galactic ISM lines). Blueshifted P V 1117 + 1128 at  $-[6000, 4000] \text{ km s}^{-1}$  is tentatively detected but no attempt is made to fit this faint feature (Fig.

13b).

*PG 1116+215.*—There are several narrow absorption features blueward of Ly $\alpha$ , O VI, and Ly $\beta$  in this system, but only two of them are paired in O VI  $\lambda$ 1032 and  $\lambda$ 1038, corresponding to  $-771$  and  $-2825$  km s $^{-1}$ . Presumably, the orphan features are intervening Ly $\alpha$  absorbers. [Savage et al. \(2014\)](#) also report an O VI system at 1175 and 1181 Å, but it is not shown here as it is very narrow and very high velocity, and is intervening CGM (there are nearby galaxies at the same redshift [Tripp et al. 1998](#)).

*PG 1126–041.*—Several separate COS/G130M spectra exist for this object (Table 2). Our analysis uses the co-added spectrum. Broad blueshifted absorption features are clearly detected in Ly $\alpha$ , N V, and O VI (Fig. 3). A narrow P V feature is observed at  $-2200$  km s $^{-1}$ , indicative of large ionized column densities. This P V detection is discussed in more detail in Section 7.4. 2014 and 2015 COS/G160M spectra centered around  $\sim 1450$  Å show strong C IV  $\lambda\lambda$ 1548, 1550 absorption throughs similar to those of N V and O VI, but only weak and narrow blueshifted S IV  $\lambda\lambda$ 1392, 1402 absorption features with  $|v| \lesssim 500$  km s $^{-1}$ ; the analysis of these features is beyond the scope of the present study.

*PG 1211+143.*—There are no associated N V absorption systems in this object. A broad absorption feature at the observed wavelength of 1240 Å has been interpreted by [Kriss et al. \(2018\)](#) as a highly blueshifted ( $-16,980$  km s $^{-1}$ ) and broad (FWHM  $\approx 1080$  km s $^{-1}$ ) Ly $\alpha$  absorption from a fast wind. It may correspond to one of the ultra-fast outflowing systems detected in the X-rays ([Danehkar et al. 2018](#), and references therein). However, since it is not detected in N V it is not included in the statistical analysis of Section 6.

*PG 1226+023 (3C 273).*—The FUV spectrum of 3C 273 has been used extensively to study the low- $z$  IGM (e.g., [Tripp et al. 2008](#); [Savage et al. 2014](#)). There are no associated N V or O VI absorption systems in this object.

*PG 1229+204.*—There are no associated N V absorption systems in this object. The many unidentified features shortward of Ly $\alpha$  in the quasar rest-frame (e.g., 1289.5, 1282, 1223.2, 1220.4 Å) may be Ly $\alpha$  from intervening CGM.

*Mrk 231.*—The 2011 COS/G130M spectrum of this object was presented in [Veilleux et al. \(2013a\)](#), while the 2014 COS/G140L and G230L spectra were presented in [Veilleux et al. \(2016\)](#). The COS/G130M spectrum shows Ly $\alpha$  emission that is broad ( $\gtrsim 10,000$  km s $^{-1}$ ) and highly blueshifted (centroid at  $\sim -3500$  km s $^{-1}$ ). In contrast, blueshifted absorption features are only present above  $\sim 2200$  Å. These results have been discussed in details in [Veilleux et al. \(2016\)](#), and this discussion is not repeated here. This outflow is considered a non-detection in our analysis in Section 6 since it has no N V absorption systems, but has all of the characteristics of a FeLoBAL at visible and NUV wavelengths and is considered as such in our discussion (Sec. 7).

*PG 1302–102.*—There are no associated O VI absorbing systems in this object, but several intervening Ly $\alpha$  and metal-line systems have been reported by [Cooksey et al. \(2008\)](#).

*PG 1307+085.*—The weak O VI absorber at  $\sim -3400$  km s $^{-1}$  is also detected in Ly $\alpha$  and Ly $\beta$ . The other feature at  $\sim -3600$  km s $^{-1}$  is seen only in Ly $\beta$  and Ly $\alpha$  and is presumed to be from intervening CGM.

*PG 1309+355.*—A broad absorption feature is visible in Ly $\alpha$ , extending blueward to  $\sim -1600$  km s $^{-1}$ . This feature is also detected in both O VI lines, but is truncated by the gap associated with the strong geocoronal Ly $\alpha$  emission. Strong absorption features are detected coincident with P V 1117 and 1128 near systemic velocity, but given their equivalent widths they are likely of Galactic origin (e.g. C II 1334).

*PG 1351+640.*—Two deep broad absorption throughs are detected in N V and Ly $\alpha$  of this object, extending over  $[-2200, -1500]$  km s $^{-1}$  and  $[-1400, -600]$  km s $^{-1}$ . They are roughly separated by the velocity separation of the N V doublet lines, resulting in a N V “triplet”, so this is a good case for line locking (Sec. 7.3.2). The template fit to the Ly $\alpha$  line emission works well in the very narrow region in which it is used, but mostly because it gets the smooth profile in this region better than a spline+polynomial fit. The central peak is steeper than the template, and it is possible that the bluest absorption region in Ly $\alpha$  at  $[-3500, 2500]$  km s $^{-1}$  is caused by a weak peak rather than a true absorption, since it does not line up with anything in N V. The N V template fit, again over this limited range, is quite good and more trustworthy over a wider wavelength range. It is actually quite comparable to the spline fit. It does not get the steep central peak in Ly $\alpha$  on the red side.

*PG 1411+442.*—This object has been the subject of a detailed analysis by [Hamann et al. \(2019b\)](#). A deep broad absorption through that extends over  $[-2800, -900]$  km s $^{-1}$  is present in N V and Ly $\alpha$ . Strong P V absorption is also detected over  $[-2200, 1400]$  km s $^{-1}$  in this object. The absorption profiles presented here should be taken only as illustrative. They are produced using a simple spline/polynomial fit to the line emission + continuum. The quasar template is much too broad to match the observed emission line profiles of Ly $\alpha$  and N V.

*PG 1435–067.*—There are no associated N V or O VI absorption systems in this object, but a faint Ly $\alpha$  absorber appears to be present at  $\sim 1369.3$  Å or  $\sim -700$  km s $^{-1}$ . The other bluer narrow absorption features are likely Ly $\alpha$

absorption from the intervening CGM.

*PG 1440+356.*—Two blueshifted N V absorbers are observed at  $-2190$  and  $-1610$   $\text{km s}^{-1}$ , and a fainter redshifted one at  $+460$   $\text{km s}^{-1}$  is also detected in both lines of the doublet. Note that the strongest of the blueshifted N V systems does not have a good match in velocity space with Ly $\alpha$ . The strong line near  $1334$  Å is produced in the Galactic ISM, while the strong line blueward of Ly $\alpha$  is presumably produced by intervening CGM. The Ly $\alpha$  line at  $+200$   $\text{km s}^{-1}$  may be systemic within the uncertainties on the redshift or a signature of inflow.

*PG 1448+273.*—A broad (FWZI  $\approx 700$   $\text{km s}^{-1}$ ) multi-component absorption feature is detected in both N V and Ly $\alpha$ . The narrow Ly $\alpha$  feature at  $\sim -2700$   $\text{km s}^{-1}$  is likely produced by intervening CGM, while the deep saturated feature at  $1280$  Å is C I from Galactic ISM.

*PG 1501+106.*—Three strong absorption features are seen blueward of Ly $\alpha$  at  $\sim 1253.0$ ,  $1255.8$ , and  $1257.2$  Å, corresponding to  $\sim -1500$ ,  $-800$ , and  $-500$   $\text{km s}^{-1}$ , respectively (the absorption near  $0$   $\text{km s}^{-1}$  is at least partly due to S II from Galactic ISM). Despite the chip gap at the position of the N V doublet, the present data allow us to rule out the presence of a N V  $\lambda 1238$  counterpart to the most highly blueshifted of these Ly $\alpha$  features since it would lie near  $\sim 1276.5$  Å and is not present in the data.

*PG 1613+658.*—Two weak narrow absorption features are detected at  $-3503$  and  $-3764$   $\text{km s}^{-1}$  in N V, O VI, and Ly $\alpha$ . The other features around N V are of Galactic ISM origin, while those in O VI and Ly $\alpha$  are likely due to intervening CGM.

*PG 1617+175.*—A broad ( $\sim 1000$   $\text{km s}^{-1}$ ) blueshifted absorption feature centered around  $\sim -3000$   $\text{km s}^{-1}$  is detected in N V, O VI, and Ly $\alpha$ . Three narrow absorbers at  $-3300$ ,  $-1630$ , and  $-1040$   $\text{km s}^{-1}$  are also detected in O VI and Ly $\alpha$  but are very weak or absent in N V.

*PG 1626+554.*—The two distinct blueshifted Ly $\alpha$  absorption features at  $1378.8$  Å and  $1374.7$  Å, corresponding to  $-740$  and  $-570$   $\text{km s}^{-1}$  in the quasar rest frame, are also detected in Ly $\beta$  but not in N V. A faint depression at  $1166.9$  Å may be the  $-570$   $\text{km s}^{-1}$  counterpart of O VI  $1032$  but it is not detected in the fainter O VI  $1038$ . This feature was judged too uncertain to be a detection in our analysis.

*PG 2130+099.*—Two deep and narrow absorption features at  $\sim -1500$  and  $0$   $\text{km s}^{-1}$  are detected in N V and Ly $\alpha$  of this object.

*PG 2214+139.*—Our analysis is based on the co-added spectrum of this object given the lack of variability in the absorption lines between 2011 and 2012 (Fig. 11). This object shows complex N V troughs that extend from  $\sim -3400$  to  $-400$   $\text{km s}^{-1}$  and are loosely matched to the complex absorption feature at Ly $\alpha$ , except for the sharp Ly $\alpha$  absorption feature near  $-100$   $\text{km s}^{-1}$ , which is not detected in N V.

*PG 2233+134.*—This object shows a faint and narrow absorber at  $\sim -200$   $\text{km s}^{-1}$  in O VI and Ly $\beta$ . The Ly $\beta$  absorber at  $\sim -1300$   $\text{km s}^{-1}$  also seems to have a weak O VI counterpart but the fit is inconclusive and is therefore not included in the statistics for this object. The other stronger lines in this spectral region do not match Galactic ISM features so they are likely produced by intervening CGM.

*PG 2349-014.*—There are no N V or O V  $\lambda 1032$  absorbers in this object (O VI  $\lambda 1038$  is lost in the glare of geocoronal Ly $\alpha$ ).

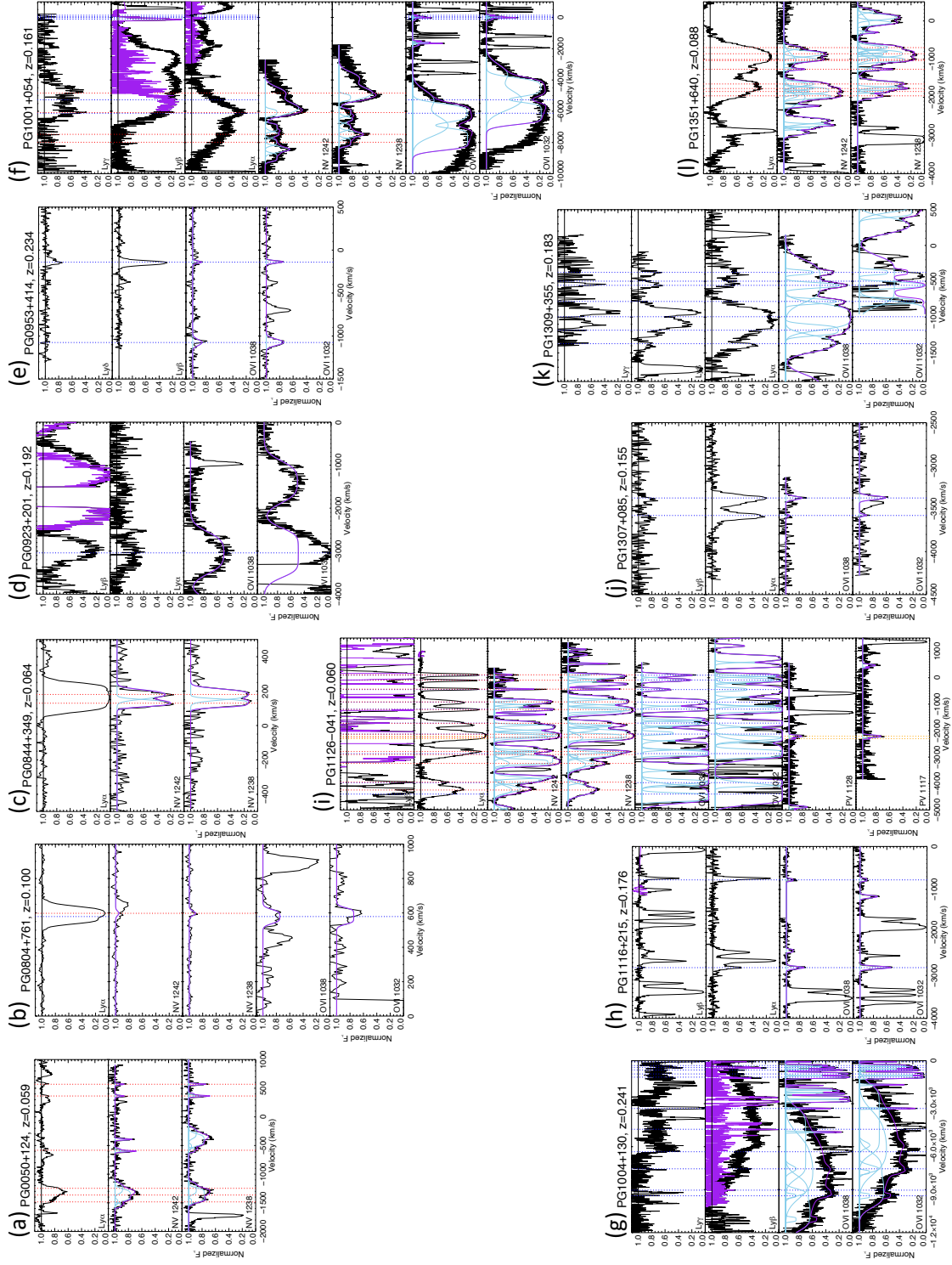


**Figure 14.** [Part I] Interline comparison of the absorbing systems in each quasar with detected N V or O VI absorption lines, produced by plotting the normalized spectrum in velocity space relative to the quasar rest frame. The data are in black, the individual components used to fit the absorption profiles are shown in cyan, and the overall fit is shown in purple. The velocity centroids of the main absorbing systems are indicated by vertical red (Ly $\alpha$ , Ly $\beta$ , N V, P V) and blue (O VI) dotted lines.

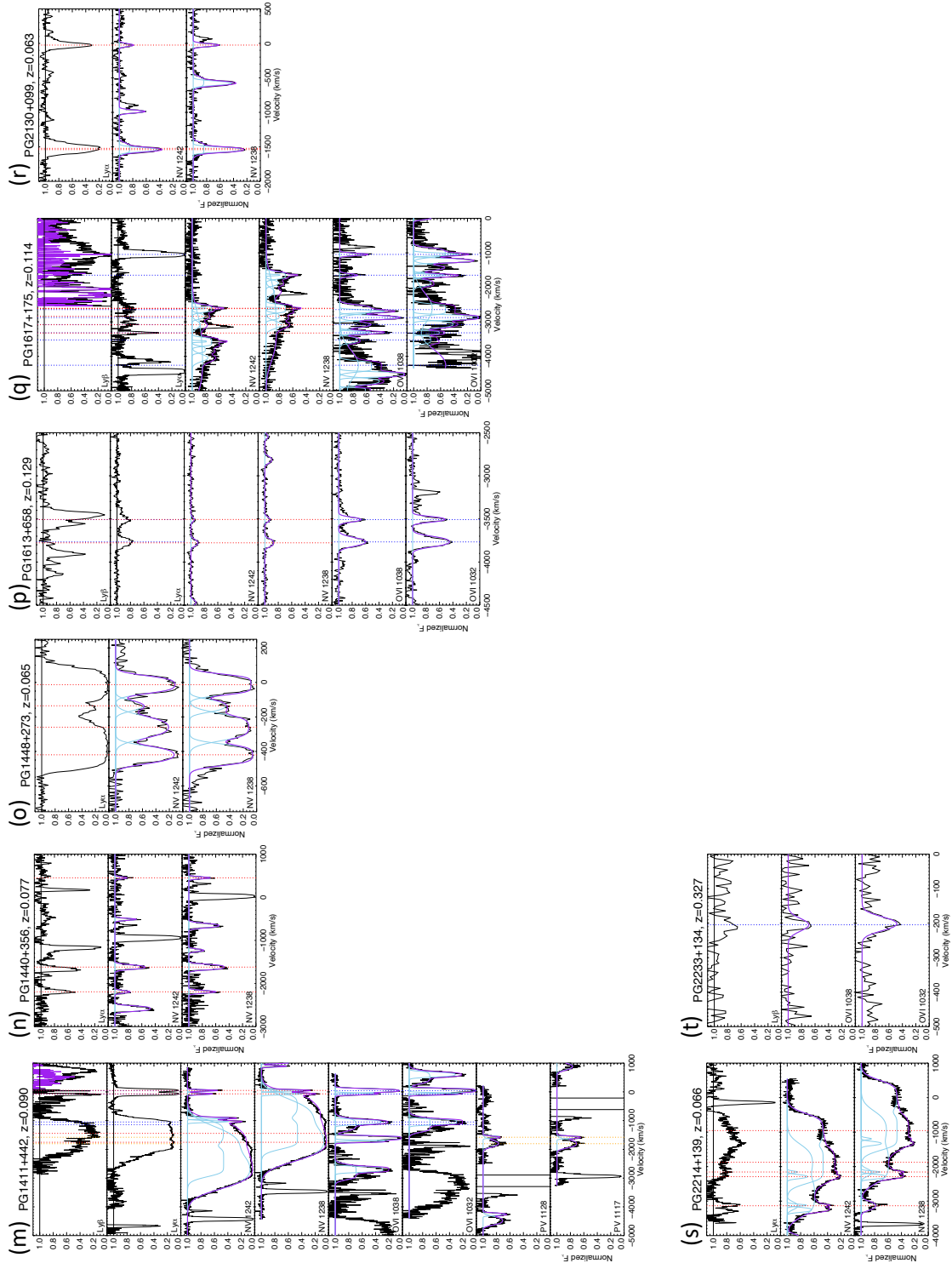


Figure 13. [Part II] Same as previous figure.



## REFERENCES

- Allen, J. T., Hewett, P. C., Maddox, N., Richards, G. T., & Belokurov, V. 2011, *MNRAS*, 410, 860, doi: [10.1111/j.1365-2966.2010.17489.x](https://doi.org/10.1111/j.1365-2966.2010.17489.x)
- Arav, N., Kaastra, J., Kriss, G. A., et al. 2005, *ApJ*, 620, 665, doi: [10.1086/425560](https://doi.org/10.1086/425560)
- Arav, N., & Li, Z.-Y. 1994, *ApJ*, 427, 700, doi: [10.1086/174177](https://doi.org/10.1086/174177)
- Arav, N., Li, Z.-Y., & Begelman, M. C. 1994, *ApJ*, 432, 62, doi: [10.1086/174549](https://doi.org/10.1086/174549)
- Arav, N., Moe, M., Costantini, E., et al. 2008, *ApJ*, 681, 954, doi: [10.1086/588651](https://doi.org/10.1086/588651)
- Arav, N., Xu, X., Miller, T., Kriss, G. A., & Plesha, R. 2020, *ApJS*, 247, 37, doi: [10.3847/1538-4365/ab66af](https://doi.org/10.3847/1538-4365/ab66af)
- Arav, N., Chamberlain, C., Kriss, G. A., et al. 2015, *A&A*, 577, A37, doi: [10.1051/0004-6361/201425302](https://doi.org/10.1051/0004-6361/201425302)
- Banda-Barragán, W. E., Brüggén, M., Federrath, C., et al. 2020, *MNRAS*, 499, 2173, doi: [10.1093/mnras/staa2904](https://doi.org/10.1093/mnras/staa2904)
- Banda-Barragán, W. E., Federrath, C., Crocker, R. M., & Bicknell, G. V. 2018, *MNRAS*, 473, 3454, doi: [10.1093/mnras/stx2541](https://doi.org/10.1093/mnras/stx2541)
- Banda-Barragán, W. E., Parkin, E. R., Federrath, C., Crocker, R. M., & Bicknell, G. V. 2016, *MNRAS*, 455, 1309, doi: [10.1093/mnras/stv2405](https://doi.org/10.1093/mnras/stv2405)
- Barvainis, R. 1987, *ApJ*, 320, 537, doi: [10.1086/165571](https://doi.org/10.1086/165571)
- Baskin, A., & Laor, A. 2005, *MNRAS*, 356, 1029, doi: [10.1111/j.1365-2966.2004.08525.x](https://doi.org/10.1111/j.1365-2966.2004.08525.x)
- . 2018, *MNRAS*, 474, 1970, doi: [10.1093/mnras/stx2850](https://doi.org/10.1093/mnras/stx2850)
- Baskin, A., Laor, A., & Hamann, F. 2013, *MNRAS*, 432, 1525, doi: [10.1093/mnras/stt582](https://doi.org/10.1093/mnras/stt582)
- Baskin, A., Laor, A., & Stern, J. 2014, *MNRAS*, 445, 3025, doi: [10.1093/mnras/stu1732](https://doi.org/10.1093/mnras/stu1732)
- Becker, R. H., White, R. L., Gregg, M. D., et al. 2001, *ApJS*, 135, 227, doi: [10.1086/321798](https://doi.org/10.1086/321798)
- Benn, C. R., Carballo, R., Holt, J., et al. 2005, *MNRAS*, 360, 1455, doi: [10.1111/j.1365-2966.2005.09143.x](https://doi.org/10.1111/j.1365-2966.2005.09143.x)
- Bentz, M. C., & Katz, S. 2015, *PASP*, 127, 67, doi: [10.1086/679601](https://doi.org/10.1086/679601)
- Bentz, M. C., Denney, K. D., Grier, C. J., et al. 2013, *ApJ*, 767, 149, doi: [10.1088/0004-637X/767/2/149](https://doi.org/10.1088/0004-637X/767/2/149)
- Borguet, B. C. J., Arav, N., Edmonds, D., Chamberlain, C., & Benn, C. 2013, *ApJ*, 762, 49, doi: [10.1088/0004-637X/762/1/49](https://doi.org/10.1088/0004-637X/762/1/49)
- Borguet, B. C. J., Edmonds, D., Arav, N., Benn, C., & Chamberlain, C. 2012, *ApJ*, 758, 69, doi: [10.1088/0004-637X/758/1/69](https://doi.org/10.1088/0004-637X/758/1/69)
- Boroson, T. A., & Green, R. F. 1992, *ApJS*, 80, 109, doi: [10.1086/191661](https://doi.org/10.1086/191661)
- Bowler, R. A. A., Hewett, P. C., Allen, J. T., & Ferland, G. J. 2014, *MNRAS*, 445, 359, doi: [10.1093/mnras/stu1730](https://doi.org/10.1093/mnras/stu1730)
- Brandt, W. N., Laor, A., & Wills, B. J. 2000, *ApJ*, 528, 637, doi: [10.1086/308207](https://doi.org/10.1086/308207)
- Braun, E., & Milgrom, M. 1989, *ApJ*, 342, 100, doi: [10.1086/167578](https://doi.org/10.1086/167578)
- Cameron, E. 2011, *PASA*, 28, 128, doi: [10.1071/AS10046](https://doi.org/10.1071/AS10046)
- Capellupo, D. M., Hamann, F., Shields, J. C., Rodríguez Hidalgo, P., & Barlow, T. A. 2012, *MNRAS*, 422, 3249, doi: [10.1111/j.1365-2966.2012.20846.x](https://doi.org/10.1111/j.1365-2966.2012.20846.x)
- Capellupo, D. M., Hamann, F., Herbst, H., et al. 2017, *MNRAS*, 469, 323, doi: [10.1093/mnras/stx870](https://doi.org/10.1093/mnras/stx870)
- Carilli, C. L., Wrobel, J. M., & Ulvestad, J. S. 1998, *AJ*, 115, 928, doi: [10.1086/300253](https://doi.org/10.1086/300253)
- Cicone, C., Maiolino, R., Sturm, E., et al. 2014, *A&A*, 562, A21, doi: [10.1051/0004-6361/201322464](https://doi.org/10.1051/0004-6361/201322464)
- Cooksey, K. L., Prochaska, J. X., Chen, H.-W., Mulchaey, J. S., & Weiner, B. J. 2008, *ApJ*, 676, 262, doi: [10.1086/528704](https://doi.org/10.1086/528704)
- Cooper, J. L., Bicknell, G. V., Sutherland, R. S., & Bland-Hawthorn, J. 2009, *ApJ*, 703, 330, doi: [10.1088/0004-637X/703/1/330](https://doi.org/10.1088/0004-637X/703/1/330)
- Crenshaw, D. M., & Kraemer, S. B. 2012, *ApJ*, 753, 75, doi: [10.1088/0004-637X/753/1/75](https://doi.org/10.1088/0004-637X/753/1/75)
- Crenshaw, D. M., Kraemer, S. B., Boggess, A., et al. 1999, *ApJ*, 516, 750, doi: [10.1086/307144](https://doi.org/10.1086/307144)
- Curran, P. A. 2014, arXiv e-prints, arXiv:1411.3816. <https://arxiv.org/abs/1411.3816>
- Danehkar, A., Nowak, M. A., Lee, J. C., et al. 2018, *ApJ*, 853, 165, doi: [10.3847/1538-4357/aaa427](https://doi.org/10.3847/1538-4357/aaa427)
- Danforth, C. W., Keeney, B. A., Stocke, J. T., Shull, J. M., & Yao, Y. 2010, *ApJ*, 720, 976, doi: [10.1088/0004-637X/720/1/976](https://doi.org/10.1088/0004-637X/720/1/976)
- Danforth, C. W., Keeney, B. A., Tilton, E. M., et al. 2016, *ApJ*, 817, 111, doi: [10.3847/0004-637X/817/2/111](https://doi.org/10.3847/0004-637X/817/2/111)
- Dasyra, K. M., Tacconi, L. J., Davies, R. I., et al. 2007, *ApJ*, 657, 102, doi: [10.1086/510552](https://doi.org/10.1086/510552)
- de Vaucouleurs, G., de Vaucouleurs, A., Corwin, Herold G., J., et al. 1991, *Third Reference Catalogue of Bright Galaxies*
- Dunn, J. P., Crenshaw, D. M., Kraemer, S. B., & Trippe, M. L. 2008, *AJ*, 136, 1201, doi: [10.1088/0004-6256/136/3/1201](https://doi.org/10.1088/0004-6256/136/3/1201)
- Efstathiou, G. 2000, *MNRAS*, 317, 697, doi: [10.1046/j.1365-8711.2000.03665.x](https://doi.org/10.1046/j.1365-8711.2000.03665.x)
- Elvis, M. 2000, *ApJ*, 545, 63, doi: [10.1086/317778](https://doi.org/10.1086/317778)
- Evans, A. S., Solomon, P. M., Tacconi, L. J., Vavilkin, T., & Downes, D. 2006, *AJ*, 132, 2398, doi: [10.1086/508416](https://doi.org/10.1086/508416)

- Faucher-Giguère, C.-A., & Quataert, E. 2012, *MNRAS*, 425, 605, doi: [10.1111/j.1365-2966.2012.21512.x](https://doi.org/10.1111/j.1365-2966.2012.21512.x)
- Filiz Ak, N., Brandt, W. N., Hall, P. B., et al. 2012, *ApJ*, 757, 114, doi: [10.1088/0004-637X/757/2/114](https://doi.org/10.1088/0004-637X/757/2/114)
- . 2013, *ApJ*, 777, 168, doi: [10.1088/0004-637X/777/2/168](https://doi.org/10.1088/0004-637X/777/2/168)
- Fitzpatrick, E. L. 1999, *PASP*, 111, 63, doi: [10.1086/316293](https://doi.org/10.1086/316293)
- Fluetsch, A., Maiolino, R., Carniani, S., et al. 2019, *MNRAS*, 483, 4586, doi: [10.1093/mnras/sty3449](https://doi.org/10.1093/mnras/sty3449)
- . 2020, arXiv e-prints, arXiv:2006.13232. <https://arxiv.org/abs/2006.13232>
- Foltz, C. B., Weymann, R. J., Morris, S. L., & Turnshek, D. A. 1987, *ApJ*, 317, 450, doi: [10.1086/165290](https://doi.org/10.1086/165290)
- Gabel, J. R., Crenshaw, D. M., Kraemer, S. B., et al. 2003, *ApJ*, 583, 178, doi: [10.1086/345096](https://doi.org/10.1086/345096)
- Ganguly, R., Bond, N. A., Charlton, J. C., et al. 2001, *ApJ*, 549, 133, doi: [10.1086/319082](https://doi.org/10.1086/319082)
- Ganguly, R., & Brotherton, M. S. 2008, *ApJ*, 672, 102, doi: [10.1086/524106](https://doi.org/10.1086/524106)
- Ganguly, R., Brotherton, M. S., Cales, S., et al. 2007, *ApJ*, 665, 990, doi: [10.1086/519759](https://doi.org/10.1086/519759)
- Ganguly, R., Masiero, J., Charlton, J. C., & Sembach, K. R. 2003, *ApJ*, 598, 922, doi: [10.1086/379057](https://doi.org/10.1086/379057)
- George, I. M., Turner, T. J., Netzer, H., et al. 1998, *ApJS*, 114, 73, doi: [10.1086/313067](https://doi.org/10.1086/313067)
- Gibson, R. R., Brandt, W. N., Gallagher, S. C., Hewett, P. C., & Schneider, D. P. 2010, *ApJ*, 713, 220, doi: [10.1088/0004-637X/713/1/220](https://doi.org/10.1088/0004-637X/713/1/220)
- Gibson, R. R., Brandt, W. N., Gallagher, S. C., & Schneider, D. P. 2009a, *ApJ*, 696, 924, doi: [10.1088/0004-637X/696/1/924](https://doi.org/10.1088/0004-637X/696/1/924)
- Gibson, R. R., Brandt, W. N., Schneider, D. P., & Gallagher, S. C. 2008, *ApJ*, 675, 985, doi: [10.1086/527462](https://doi.org/10.1086/527462)
- Gibson, R. R., Jiang, L., Brandt, W. N., et al. 2009b, *ApJ*, 692, 758, doi: [10.1088/0004-637X/692/1/758](https://doi.org/10.1088/0004-637X/692/1/758)
- Girichidis, P., Naab, T., Walch, S., & Berlok, T. 2021, *MNRAS*, doi: [10.1093/mnras/stab1203](https://doi.org/10.1093/mnras/stab1203)
- Giustini, M., & Proga, D. 2019, *A&A*, 630, A94, doi: [10.1051/0004-6361/201833810](https://doi.org/10.1051/0004-6361/201833810)
- Giustini, M., Cappi, M., Chartas, G., et al. 2011, *A&A*, 536, A49, doi: [10.1051/0004-6361/201117732](https://doi.org/10.1051/0004-6361/201117732)
- Gravity Collaboration, Sturm, E., Dexter, J., et al. 2018, *Nature*, 563, 657, doi: [10.1038/s41586-018-0731-9](https://doi.org/10.1038/s41586-018-0731-9)
- Grier, C. J., Hall, P. B., Brandt, W. N., et al. 2015, *ApJ*, 806, 111, doi: [10.1088/0004-637X/806/1/111](https://doi.org/10.1088/0004-637X/806/1/111)
- Gronke, M., & Oh, S. P. 2018, *MNRAS*, 480, L111, doi: [10.1093/mnrasl/sly131](https://doi.org/10.1093/mnrasl/sly131)
- . 2020, *MNRAS*, 492, 1970, doi: [10.1093/mnras/stz3332](https://doi.org/10.1093/mnras/stz3332)
- Grønnow, A., Tepper-García, T., & Bland-Hawthorn, J. 2018, *ApJ*, 865, 64, doi: [10.3847/1538-4357/aada0e](https://doi.org/10.3847/1538-4357/aada0e)
- Guyon, O., Sanders, D. B., & Stockton, A. 2006, *ApJS*, 166, 89, doi: [10.1086/505030](https://doi.org/10.1086/505030)
- Haislmaier, K. J., Tripp, T. M., Katz, N., et al. 2021, *MNRAS*, 502, 4993, doi: [10.1093/mnras/staa3544](https://doi.org/10.1093/mnras/staa3544)
- Hamann, F. 1998, *ApJ*, 500, 798, doi: [10.1086/305776](https://doi.org/10.1086/305776)
- Hamann, F., Barlow, T. A., Junkkarinen, V., & Burbidge, E. M. 1997a, *ApJ*, 478, 80, doi: [10.1086/303781](https://doi.org/10.1086/303781)
- Hamann, F., Beaver, E. A., Cohen, R. D., et al. 1997b, *ApJ*, 488, 155, doi: [10.1086/304698](https://doi.org/10.1086/304698)
- Hamann, F., Chartas, G., McGraw, S., et al. 2013, *MNRAS*, 435, 133, doi: [10.1093/mnras/stt1231](https://doi.org/10.1093/mnras/stt1231)
- Hamann, F., Herbst, H., Paris, I., & Capellupo, D. 2019a, *MNRAS*, 483, 1808, doi: [10.1093/mnras/sty2900](https://doi.org/10.1093/mnras/sty2900)
- Hamann, F., Kanekar, N., Prochaska, J. X., et al. 2011, *MNRAS*, 410, 1957, doi: [10.1111/j.1365-2966.2010.17575.x](https://doi.org/10.1111/j.1365-2966.2010.17575.x)
- Hamann, F., Kaplan, K. F., Rodríguez Hidalgo, P., Prochaska, J. X., & Herbert-Fort, S. 2008, *MNRAS*, 391, L39, doi: [10.1111/j.1745-3933.2008.00554.x](https://doi.org/10.1111/j.1745-3933.2008.00554.x)
- Hamann, F., & Sabra, B. 2004, in *Astronomical Society of the Pacific Conference Series*, Vol. 311, *AGN Physics with the Sloan Digital Sky Survey*, ed. G. T. Richards & P. B. Hall, 203. <https://arxiv.org/abs/astro-ph/0310668>
- Hamann, F., Tripp, T. M., Rupke, D., & Veilleux, S. 2019b, *MNRAS*, 487, 5041, doi: [10.1093/mnras/stz1408](https://doi.org/10.1093/mnras/stz1408)
- Hamilton, T. S., Casertano, S., & Turnshek, D. A. 2008, *ApJ*, 678, 22, doi: [10.1086/524182](https://doi.org/10.1086/524182)
- Harris, D. W., Jensen, T. W., Suzuki, N., et al. 2016, *AJ*, 151, 155, doi: [10.3847/0004-6256/151/6/155](https://doi.org/10.3847/0004-6256/151/6/155)
- He, Z., Wang, T., Liu, G., et al. 2019, *Nature Astronomy*, 3, 265, doi: [10.1038/s41550-018-0669-8](https://doi.org/10.1038/s41550-018-0669-8)
- Hewett, P. C., & Wild, V. 2010, *MNRAS*, 405, 2302, doi: [10.1111/j.1365-2966.2010.16648.x](https://doi.org/10.1111/j.1365-2966.2010.16648.x)
- Hickox, R. C., & Alexander, D. M. 2018, *ARA&A*, 56, 625, doi: [10.1146/annurev-astro-081817-051803](https://doi.org/10.1146/annurev-astro-081817-051803)
- Ho, L. C., & Kim, M. 2009, *ApJS*, 184, 398, doi: [10.1088/0067-0049/184/2/398](https://doi.org/10.1088/0067-0049/184/2/398)
- Hopkins, P. F., & Elvis, M. 2010, *MNRAS*, 401, 7, doi: [10.1111/j.1365-2966.2009.15643.x](https://doi.org/10.1111/j.1365-2966.2009.15643.x)
- Hopkins, P. F., Grudić, M. Y., Wetzell, A., et al. 2020, *MNRAS*, 491, 3702, doi: [10.1093/mnras/stz3129](https://doi.org/10.1093/mnras/stz3129)
- Hopkins, P. F., Kereš, D., Oñorbe, J., et al. 2014, *MNRAS*, 445, 581, doi: [10.1093/mnras/stu1738](https://doi.org/10.1093/mnras/stu1738)
- Hu, C., Li, S.-S., Guo, W.-J., et al. 2020, *ApJ*, 905, 75, doi: [10.3847/1538-4357/abc2da](https://doi.org/10.3847/1538-4357/abc2da)
- Inoue, H., Terashima, Y., & Ho, L. C. 2007, *ApJ*, 662, 860, doi: [10.1086/517995](https://doi.org/10.1086/517995)
- Ishibashi, W., Fabian, A. C., & Arakawa, N. 2021, *MNRAS*, 502, 3638, doi: [10.1093/mnras/stab266](https://doi.org/10.1093/mnras/stab266)

- Ishibashi, W., Fabian, A. C., & Maiolino, R. 2018, *MNRAS*, 476, 512, doi: [10.1093/mnras/sty236](https://doi.org/10.1093/mnras/sty236)
- Isobe, T., Feigelson, E. D., & Nelson, P. I. 1986, *ApJ*, 306, 490, doi: [10.1086/164359](https://doi.org/10.1086/164359)
- Jin, C., Ward, M., Done, C., & Gelbord, J. 2012, *MNRAS*, 420, 1825, doi: [10.1111/j.1365-2966.2011.19805.x](https://doi.org/10.1111/j.1365-2966.2011.19805.x)
- Kaspi, S., Brandt, W. N., Maoz, D., et al. 2007, *ApJ*, 659, 997, doi: [10.1086/512094](https://doi.org/10.1086/512094)
- Kaspi, S., Brandt, W. N., Netzer, H., et al. 2000, *ApJL*, 535, L17, doi: [10.1086/312697](https://doi.org/10.1086/312697)
- Kaspi, S., Maoz, D., Netzer, H., et al. 2005, *ApJ*, 629, 61, doi: [10.1086/431275](https://doi.org/10.1086/431275)
- Kaspi, S., Brandt, W. N., Netzer, H., et al. 2001, *ApJ*, 554, 216, doi: [10.1086/321333](https://doi.org/10.1086/321333)
- Kelly, B. C. 2007, *ApJ*, 665, 1489, doi: [10.1086/519947](https://doi.org/10.1086/519947)
- Kim, M., Ho, L. C., Peng, C. Y., Barth, A. J., & Im, M. 2008, *ApJS*, 179, 283, doi: [10.1086/591796](https://doi.org/10.1086/591796)
- Knigge, C., Scaringi, S., Goad, M. R., & Cottis, C. E. 2008, *MNRAS*, 386, 1426, doi: [10.1111/j.1365-2966.2008.13081.x](https://doi.org/10.1111/j.1365-2966.2008.13081.x)
- Kraemer, S. B., Crenshaw, D. M., & Gabel, J. R. 2001, *ApJ*, 557, 30, doi: [10.1086/321619](https://doi.org/10.1086/321619)
- Kriss, G. A. 2004a, arXiv e-prints, astro. <https://arxiv.org/abs/astro-ph/0411380>
- Kriss, G. A. 2004b, in *The Interplay Among Black Holes, Stars and ISM in Galactic Nuclei*, ed. T. Storchi-Bergmann, L. C. Ho, & H. R. Schmitt, Vol. 222, 223–228, doi: [10.1017/S1743921304002157](https://doi.org/10.1017/S1743921304002157)
- Kriss, G. A., Lee, J. C., Danehkar, A., et al. 2018, *ApJ*, 853, 166, doi: [10.3847/1538-4357/aaa42b](https://doi.org/10.3847/1538-4357/aaa42b)
- Krongold, Y., Nicastro, F., Brickhouse, N. S., et al. 2003, *ApJ*, 597, 832, doi: [10.1086/378639](https://doi.org/10.1086/378639)
- Krug, H. B. 2013, PhD thesis, University of Maryland, College Park
- Laha, S., Guainazzi, M., Piconcelli, E., et al. 2018, *ApJ*, 868, 10, doi: [10.3847/1538-4357/aae390](https://doi.org/10.3847/1538-4357/aae390)
- Laha, S., Reynolds, C. S., Reeves, J., et al. 2021, *Nature Astronomy*, 5, 13, doi: [10.1038/s41550-020-01255-2](https://doi.org/10.1038/s41550-020-01255-2)
- Lani, C., Netzer, H., & Lutz, D. 2017, *MNRAS*, 471, 59, doi: [10.1093/mnras/stx1374](https://doi.org/10.1093/mnras/stx1374)
- Laor, A., & Brandt, W. N. 2002, *ApJ*, 569, 641, doi: [10.1086/339476](https://doi.org/10.1086/339476)
- Laor, A., & Davis, S. W. 2014, *MNRAS*, 438, 3024, doi: [10.1093/mnras/stt2408](https://doi.org/10.1093/mnras/stt2408)
- Leighly, K. M., Dietrich, M., & Barber, S. 2011, *ApJ*, 728, 94, doi: [10.1088/0004-637X/728/2/94](https://doi.org/10.1088/0004-637X/728/2/94)
- Lodders, K. 2003, *ApJ*, 591, 1220, doi: [10.1086/375492](https://doi.org/10.1086/375492)
- Lu, W.-J., & Lin, Y.-R. 2018, *ApJ*, 863, 186, doi: [10.3847/1538-4357/aad411](https://doi.org/10.3847/1538-4357/aad411)
- Luo, B., Brandt, W. N., Hall, P. B., et al. 2015, *ApJ*, 805, 122, doi: [10.1088/0004-637X/805/2/122](https://doi.org/10.1088/0004-637X/805/2/122)
- Lutz, D., Sturm, E., Janssen, A., et al. 2020, *A&A*, 633, A134, doi: [10.1051/0004-6361/201936803](https://doi.org/10.1051/0004-6361/201936803)
- Lyu, J., Rieke, G. H., & Shi, Y. 2017, *ApJ*, 835, 257, doi: [10.3847/1538-4357/835/2/257](https://doi.org/10.3847/1538-4357/835/2/257)
- Marcolini, A., Strickland, D. K., D’Ercole, A., Heckman, T. M., & Hoopes, C. G. 2005, *MNRAS*, 362, 626, doi: [10.1111/j.1365-2966.2005.09343.x](https://doi.org/10.1111/j.1365-2966.2005.09343.x)
- Martin, C. L., Dijkstra, M., Henry, A., et al. 2015, *ApJ*, 803, 6, doi: [10.1088/0004-637X/803/1/6](https://doi.org/10.1088/0004-637X/803/1/6)
- Marziani, P., Sulentic, J. W., Dultzin-Hacyan, D., Calvani, M., & Moles, M. 1996, *ApJS*, 104, 37, doi: [10.1086/192291](https://doi.org/10.1086/192291)
- Mas-Ribas, L., & Mauland, R. 2019, *ApJ*, 886, 151, doi: [10.3847/1538-4357/ab4efd](https://doi.org/10.3847/1538-4357/ab4efd)
- Moravec, E. A., Hamann, F., Capellupo, D. M., et al. 2017, *MNRAS*, 468, 4539, doi: [10.1093/mnras/stx775](https://doi.org/10.1093/mnras/stx775)
- Murray, N., Chiang, J., Grossman, S. A., & Voit, G. M. 1995, *ApJ*, 451, 498, doi: [10.1086/176238](https://doi.org/10.1086/176238)
- Mushotzky, R. F., Solomon, P. M., & Strittmatter, P. A. 1972, *ApJ*, 174, 7, doi: [10.1086/151463](https://doi.org/10.1086/151463)
- Nelson, D., Pillepich, A., Springel, V., et al. 2019, *MNRAS*, 490, 3234, doi: [10.1093/mnras/stz2306](https://doi.org/10.1093/mnras/stz2306)
- Nelson, E. J., Tacchella, S., Diemer, B., et al. 2021, arXiv e-prints, arXiv:2101.12212. <https://arxiv.org/abs/2101.12212>
- Netzer, H., & Laor, A. 1993, *ApJL*, 404, L51, doi: [10.1086/186741](https://doi.org/10.1086/186741)
- Netzer, H., Lutz, D., Schweitzer, M., et al. 2007, *ApJ*, 666, 806, doi: [10.1086/520716](https://doi.org/10.1086/520716)
- Nims, J., Quataert, E., & Faucher-Giguère, C.-A. 2015, *MNRAS*, 447, 3612, doi: [10.1093/mnras/stu2648](https://doi.org/10.1093/mnras/stu2648)
- Onken, C. A., Ferrarese, L., Merritt, D., et al. 2004, *ApJ*, 615, 645, doi: [10.1086/424655](https://doi.org/10.1086/424655)
- Oppenheimer, B. D., Davies, J. J., Crain, R. A., et al. 2020, *MNRAS*, 491, 2939, doi: [10.1093/mnras/stz3124](https://doi.org/10.1093/mnras/stz3124)
- Perry, J. J., & O’Dell, S. L. 1978, *A&A*, 62, 229
- Piconcelli, E., Jimenez-Bailón, E., Guainazzi, M., et al. 2005, *A&A*, 432, 15, doi: [10.1051/0004-6361:20041621](https://doi.org/10.1051/0004-6361:20041621)
- Privon, G. C., Ricci, C., Aalto, S., et al. 2020, *ApJ*, 893, 149, doi: [10.3847/1538-4357/ab8015](https://doi.org/10.3847/1538-4357/ab8015)
- Prochaska, J. X., Wolfe, A. M., Tytler, D., et al. 2001, *ApJS*, 137, 21, doi: [10.1086/322542](https://doi.org/10.1086/322542)
- Proga, D. 2007, *ApJ*, 661, 693, doi: [10.1086/515389](https://doi.org/10.1086/515389)
- Proga, D., & Kallman, T. R. 2004, *ApJ*, 616, 688, doi: [10.1086/425117](https://doi.org/10.1086/425117)
- Rankine, A. L., Hewett, P. C., Banerji, M., & Richards, G. T. 2020, *MNRAS*, 492, 4553, doi: [10.1093/mnras/staa1310](https://doi.org/10.1093/mnras/staa1310)

- Revalski, M., Crenshaw, D. M., Kraemer, S. B., et al. 2018, *ApJ*, 856, 46, doi: [10.3847/1538-4357/aab107](https://doi.org/10.3847/1538-4357/aab107)
- Reynolds, C. S. 1997, *MNRAS*, 286, 513, doi: [10.1093/mnras/286.3.513](https://doi.org/10.1093/mnras/286.3.513)
- Ricci, C., Trakhtenbrot, B., Koss, M. J., et al. 2017, *ApJS*, 233, 17, doi: [10.3847/1538-4365/aa96ad](https://doi.org/10.3847/1538-4365/aa96ad)
- Richards, G. T., Kruczek, N. E., Gallagher, S. C., et al. 2011, *AJ*, 141, 167, doi: [10.1088/0004-6256/141/5/167](https://doi.org/10.1088/0004-6256/141/5/167)
- Richings, A. J., & Faucher-Giguère, C.-A. 2018a, *MNRAS*, 474, 3673, doi: [10.1093/mnras/stx3014](https://doi.org/10.1093/mnras/stx3014)
- . 2018b, *MNRAS*, 478, 3100, doi: [10.1093/mnras/sty1285](https://doi.org/10.1093/mnras/sty1285)
- Richings, A. J., Faucher-Giguère, C.-A., & Stern, J. 2021, *MNRAS*, 503, 1568, doi: [10.1093/mnras/stab556](https://doi.org/10.1093/mnras/stab556)
- Rupke, D. 2021a, doi: [10.5281/zenodo.5659382](https://doi.org/10.5281/zenodo.5659382)
- . 2021b, doi: [10.5281/zenodo.5659520](https://doi.org/10.5281/zenodo.5659520)
- . 2021c, doi: [10.5281/zenodo.5659554](https://doi.org/10.5281/zenodo.5659554)
- Rupke, D. S., Veilleux, S., & Sanders, D. B. 2005, *ApJS*, 160, 87, doi: [10.1086/432886](https://doi.org/10.1086/432886)
- Rupke, D. S. N. 2014, *IFSFIT: Spectral Fitting for Integral Field Spectrographs*. <http://ascl.net/1409.005>
- Rupke, D. S. N., Gültekin, K., & Veilleux, S. 2017, *ApJ*, 850, 40, doi: [10.3847/1538-4357/aa94d1](https://doi.org/10.3847/1538-4357/aa94d1)
- Rupke, D. S. N., & Veilleux, S. 2015, *ApJ*, 801, 126, doi: [10.1088/0004-637X/801/2/126](https://doi.org/10.1088/0004-637X/801/2/126)
- Sanders, D. B., Soifer, B. T., Elias, J. H., et al. 1988, *ApJ*, 325, 74, doi: [10.1086/165983](https://doi.org/10.1086/165983)
- Savage, B. D., Kim, T. S., Wakker, B. P., et al. 2014, *ApJS*, 212, 8, doi: [10.1088/0067-0049/212/1/8](https://doi.org/10.1088/0067-0049/212/1/8)
- Scannapieco, E., & Brügggen, M. 2015, *ApJ*, 805, 158, doi: [10.1088/0004-637X/805/2/158](https://doi.org/10.1088/0004-637X/805/2/158)
- Scargle, J. D. 1973, *ApJ*, 179, 705, doi: [10.1086/151910](https://doi.org/10.1086/151910)
- Schlaflly, E. F., & Finkbeiner, D. P. 2011, *ApJ*, 737, 103, doi: [10.1088/0004-637X/737/2/103](https://doi.org/10.1088/0004-637X/737/2/103)
- Schmidt, M., & Green, R. F. 1983, *ApJ*, 269, 352, doi: [10.1086/161048](https://doi.org/10.1086/161048)
- Schneider, D. P., Richards, G. T., Hall, P. B., et al. 2010, *AJ*, 139, 2360, doi: [10.1088/0004-6256/139/6/2360](https://doi.org/10.1088/0004-6256/139/6/2360)
- Schneider, E. E., Ostriker, E. C., Robertson, B. E., & Thompson, T. A. 2020, *ApJ*, 895, 43, doi: [10.3847/1538-4357/ab8ae8](https://doi.org/10.3847/1538-4357/ab8ae8)
- Schneider, E. E., & Robertson, B. E. 2015, *ApJS*, 217, 24, doi: [10.1088/0067-0049/217/2/24](https://doi.org/10.1088/0067-0049/217/2/24)
- . 2017, *ApJ*, 834, 144, doi: [10.3847/1538-4357/834/2/144](https://doi.org/10.3847/1538-4357/834/2/144)
- Schweitzer, M., Lutz, D., Sturm, E., et al. 2006, *ApJ*, 649, 79, doi: [10.1086/506510](https://doi.org/10.1086/506510)
- Schweitzer, M., Groves, B., Netzer, H., et al. 2008, *ApJ*, 679, 101, doi: [10.1086/587097](https://doi.org/10.1086/587097)
- Shangguan, J., Ho, L. C., & Xie, Y. 2018, *ApJ*, 854, 158, doi: [10.3847/1538-4357/aaa9be](https://doi.org/10.3847/1538-4357/aaa9be)
- Shankar, F., Dai, X., & Sivakoff, G. R. 2008, *ApJ*, 687, 859, doi: [10.1086/591488](https://doi.org/10.1086/591488)
- Silich, S., Tenorio-Tagle, G., & Muñoz-Tuñón, C. 2003, *ApJ*, 590, 791, doi: [10.1086/375133](https://doi.org/10.1086/375133)
- Silva, C. V., Costantini, E., Giustini, M., et al. 2018, *MNRAS*, 480, 2334, doi: [10.1093/mnras/sty1938](https://doi.org/10.1093/mnras/sty1938)
- Sim, S. A., Proga, D., Miller, L., Long, K. S., & Turner, T. J. 2010, *MNRAS*, 408, 1396, doi: [10.1111/j.1365-2966.2010.17215.x](https://doi.org/10.1111/j.1365-2966.2010.17215.x)
- Somalwar, J., Johnson, S. D., Stern, J., et al. 2020, *ApJL*, 890, L28, doi: [10.3847/2041-8213/ab733d](https://doi.org/10.3847/2041-8213/ab733d)
- Springob, C. M., Haynes, M. P., Giovanelli, R., & Kent, B. R. 2005, *ApJS*, 160, 149, doi: [10.1086/431550](https://doi.org/10.1086/431550)
- Srianand, R. 2000, *ApJ*, 528, 617, doi: [10.1086/308214](https://doi.org/10.1086/308214)
- Srianand, R., Petitjean, P., Ledoux, C., & Hazard, C. 2002, *MNRAS*, 336, 753, doi: [10.1046/j.1365-8711.2002.05792.x](https://doi.org/10.1046/j.1365-8711.2002.05792.x)
- Stern, J., Faucher-Giguère, C.-A., Zakamska, N. L., & Hennawi, J. F. 2016, *ApJ*, 819, 130, doi: [10.3847/0004-637X/819/2/130](https://doi.org/10.3847/0004-637X/819/2/130)
- Stevens, M. L., Shull, J. M., Danforth, C. W., & Tilton, E. M. 2014, *ApJ*, 794, 75, doi: [10.1088/0004-637X/794/1/75](https://doi.org/10.1088/0004-637X/794/1/75)
- Sturm, E., González-Alfonso, E., Veilleux, S., et al. 2011, *ApJL*, 733, L16, doi: [10.1088/2041-8205/733/1/L16](https://doi.org/10.1088/2041-8205/733/1/L16)
- Surace, J. A., Sanders, D. B., & Evans, A. S. 2001, *AJ*, 122, 2791, doi: [10.1086/324462](https://doi.org/10.1086/324462)
- Teng, S. H., & Veilleux, S. 2010, *ApJ*, 725, 1848, doi: [10.1088/0004-637X/725/2/1848](https://doi.org/10.1088/0004-637X/725/2/1848)
- Teng, S. H., Veilleux, S., & Baker, A. J. 2013, *ApJ*, 765, 95, doi: [10.1088/0004-637X/765/2/95](https://doi.org/10.1088/0004-637X/765/2/95)
- Teng, S. H., Brandt, W. N., Harrison, F. A., et al. 2014, *ApJ*, 785, 19, doi: [10.1088/0004-637X/785/1/19](https://doi.org/10.1088/0004-637X/785/1/19)
- Thompson, T. A., Quataert, E., Zhang, D., & Weinberg, D. H. 2016, *MNRAS*, 455, 1830, doi: [10.1093/mnras/stv2428](https://doi.org/10.1093/mnras/stv2428)
- Tombesi, F., Meléndez, M., Veilleux, S., et al. 2015, *Nature*, 519, 436, doi: [10.1038/nature14261](https://doi.org/10.1038/nature14261)
- Tombesi, F., Veilleux, S., Meléndez, M., et al. 2017, *ApJ*, 850, 151, doi: [10.3847/1538-4357/aa9579](https://doi.org/10.3847/1538-4357/aa9579)
- Tripp, T. M., Lu, L., & Savage, B. D. 1998, *ApJ*, 508, 200, doi: [10.1086/306397](https://doi.org/10.1086/306397)
- Tripp, T. M., Sembach, K. R., Bowen, D. V., et al. 2008, *ApJS*, 177, 39, doi: [10.1086/587486](https://doi.org/10.1086/587486)
- Trump, J. R., Hall, P. B., Reichard, T. A., et al. 2006, *ApJS*, 165, 1, doi: [10.1086/503834](https://doi.org/10.1086/503834)
- U, V., Medling, A., Sanders, D., et al. 2013, *ApJ*, 775, 115, doi: [10.1088/0004-637X/775/2/115](https://doi.org/10.1088/0004-637X/775/2/115)
- Vanden Berk, D. E., Richards, G. T., Bauer, A., et al. 2001, *AJ*, 122, 549, doi: [10.1086/321167](https://doi.org/10.1086/321167)

- Veilleux, S., Bolatto, A., Tombesi, F., et al. 2017, *ApJ*, 843, 18, doi: [10.3847/1538-4357/aa767d](https://doi.org/10.3847/1538-4357/aa767d)
- Veilleux, S., Kim, D. C., & Sanders, D. B. 2002, *ApJS*, 143, 315, doi: [10.1086/343844](https://doi.org/10.1086/343844)
- Veilleux, S., Maiolino, R., Bolatto, A. D., & Aalto, S. 2020, *A&A Rv*, 28, 2, doi: [10.1007/s00159-019-0121-9](https://doi.org/10.1007/s00159-019-0121-9)
- Veilleux, S., Meléndez, M., Tripp, T. M., Hamann, F., & Rupke, D. S. N. 2016, *ApJ*, 825, 42, doi: [10.3847/0004-637X/825/1/42](https://doi.org/10.3847/0004-637X/825/1/42)
- Veilleux, S., Teng, S. H., Rupke, D. S. N., Maiolino, R., & Sturm, E. 2014, *ApJ*, 790, 116, doi: [10.1088/0004-637X/790/2/116](https://doi.org/10.1088/0004-637X/790/2/116)
- Veilleux, S., Kim, D. C., Peng, C. Y., et al. 2006, *ApJ*, 643, 707, doi: [10.1086/503188](https://doi.org/10.1086/503188)
- Veilleux, S., Rupke, D. S. N., Kim, D. C., et al. 2009a, *ApJS*, 182, 628, doi: [10.1088/0067-0049/182/2/628](https://doi.org/10.1088/0067-0049/182/2/628)
- Veilleux, S., Kim, D. C., Rupke, D. S. N., et al. 2009b, *ApJ*, 701, 587, doi: [10.1088/0004-637X/701/1/587](https://doi.org/10.1088/0004-637X/701/1/587)
- Veilleux, S., Tripp, M., Hamann, F., et al. 2013a, *ApJ*, 764, 15, doi: [10.1088/0004-637X/764/1/15](https://doi.org/10.1088/0004-637X/764/1/15)
- Veilleux, S., Meléndez, M., Sturm, E., et al. 2013b, *ApJ*, 776, 27, doi: [10.1088/0004-637X/776/1/27](https://doi.org/10.1088/0004-637X/776/1/27)
- Vestergaard, M., & Peterson, B. M. 2006, *ApJ*, 641, 689, doi: [10.1086/500572](https://doi.org/10.1086/500572)
- Virtanen, P., Gommers, R., Oliphant, T. E., et al. 2020, *Nature Methods*, 17, 261, doi: [10.1038/s41592-019-0686-2](https://doi.org/10.1038/s41592-019-0686-2)
- Waddell, S. G. H., & Gallo, L. C. 2020, *MNRAS*, 498, 5207, doi: [10.1093/mnras/staa2783](https://doi.org/10.1093/mnras/staa2783)
- Wang, T., & Wang, J. 1999, *Publications of the Purple Mountain Observatory*, 18, 248
- Wang, T. G., Brinkmann, W., Wamsteker, W., Yuan, W., & Wang, J. X. 1999, *MNRAS*, 307, 821, doi: [10.1046/j.1365-8711.1999.02650.x](https://doi.org/10.1046/j.1365-8711.1999.02650.x)
- Werk, J. K., Prochaska, J. X., Cantalupo, S., et al. 2016, *ApJ*, 833, 54, doi: [10.3847/1538-4357/833/1/54](https://doi.org/10.3847/1538-4357/833/1/54)
- Weymann, R. J., Carswell, R. F., & Smith, M. G. 1981, *ARA&A*, 19, 41, doi: [10.1146/annurev.aa.19.090181.000353](https://doi.org/10.1146/annurev.aa.19.090181.000353)
- Weymann, R. J., Morris, S. L., Foltz, C. B., & Hewett, P. C. 1991, *ApJ*, 373, 23, doi: [10.1086/170020](https://doi.org/10.1086/170020)
- Weymann, R. J., Turnshek, D. A., & Christiansen, W. A. 1985, in *Astrophysics of Active Galaxies and Quasi-Stellar Objects*, ed. J. S. Miller, 333–365
- Wills, B. J., Brandt, W. N., & Laor, A. 1999, *ApJL*, 520, L91, doi: [10.1086/312165](https://doi.org/10.1086/312165)
- Wu, J., Brandt, W. N., Hall, P. B., et al. 2011, *ApJ*, 736, 28, doi: [10.1088/0004-637X/736/1/28](https://doi.org/10.1088/0004-637X/736/1/28)
- Yi, W., Brandt, W. N., Hall, P. B., et al. 2019, *ApJS*, 242, 28, doi: [10.3847/1538-4365/ab1f90](https://doi.org/10.3847/1538-4365/ab1f90)
- Zhang, S., Wang, H., Wang, T., et al. 2014, *ApJ*, 786, 42, doi: [10.1088/0004-637X/786/1/42](https://doi.org/10.1088/0004-637X/786/1/42)
- Zhuang, M.-Y., Ho, L. C., & Shanguan, J. 2018, *ApJ*, 862, 118, doi: [10.3847/1538-4357/aacc2d](https://doi.org/10.3847/1538-4357/aacc2d)
- Zubovas, K., & King, A. 2012, *ApJL*, 745, L34, doi: [10.1088/2041-8205/745/2/L34](https://doi.org/10.1088/2041-8205/745/2/L34)
- Zubovas, K., & King, A. R. 2014, *MNRAS*, 439, 400, doi: [10.1093/mnras/stt2472](https://doi.org/10.1093/mnras/stt2472)